PRAMANA
journal of physics

Vol. 50 No. 1
January 1998

INDIAN ACADEMY OF SCIENCES
Indian National Science Academy
Indian Physics Association

R Nityananda
Raman Research Institute, Bangalore

Associate Editor

H R Krishnamurthy
Indian Institute of Science, Bangalore

Editorial Board

G S Agarwal, *Physical Research Laboratory, Ahmedabad*
V Balakrishnan, *Indian Institute of Technology, Chennai*
J K Bhattacharjee, *Indian Assoc. for the Cultivation of Science, Calcutta*
D N Bose, *Indian Institute of Technology, Kharagpur*
B M Deb, *Panjab University, Chandigarh*
Rohini M Godbole, *Indian Institute of Science, Bangalore*
S Kailas, *Bhabha Atomic Research Centre, Mumbai*
R K Kaul, *The Institute of Mathematical Sciences, Chennai*
A V Khare, *Institute of Physics, Bhubaneswar*
T Padmanabhan, *Inter-Univ. Centre for Astronomy and Astrophysics, Pune*
R Ramaswamy, *Jawaharlal Nehru University, New Delhi*
A K Raychaudhuri, *National Physical Laboratory, New Delhi*
K C Rustagi, *Centre for Advanced Technology, Indore*
E V Sampathkumaran, *Tata Institute of Fundamental Research, Mumbai*
Abhijit Sen, *Institute for Plasma Research, Gandhinagar*
S K Sikka, *Bhabha Atomic Research Centre, Mumbai*
Y Singh, *Banaras Hindu University, Varanasi*

Editor of Publications of the Academy

N Mukunda
Indian Institute of Science, Bangalore

Annual Subscription Rates

All countries except India (Price includes AIR MAIL charges)	US$ 200
India	Rs. 200

Annual subscriptions for individuals for India and abroad are Rs. 100/- and $50 respectively.

All correspondence regarding subscription should be addressed to the Circulation Department of the Academy

---

Editorial Office

Indian Academy of Sciences, C V Raman Avenue,
P.B. No. 8005, Bangalore 560 080, India

Telephone: 334 2546
Telefax: 91-80-334 6094

Email: pramana@ias.ernet.in

© 1998 by the Indian Academy of Sciences. All rights reserved.

“Information for contributors” is printed in the last issue of

niversality in the effective pair interaction of *d*-shell etals – Compressibility and vacancy formation energy ' 3*d*-liquid metals

K KARMAKAR and R N JOARDER
partment of Physics, Jadavpur University, Calcutta 700 032, India

; received 23 May 1997; revised 6 October 1997

stract. Like liquid alkali metals *d*-shell liquid metals show scaling behaviour in structure and eraction potentials. A realistic interaction potential model, properly parametrized can reasonably cribe the universality in the isothermal compressibility and vacancy formation energy of 3*d*-uid metals in electron ion plasma model.

ywords. Universality; effective pair-potential; 3*d*-liquid metals.

CS No. 61.25

Introduction

is now well established that for liquid alkali metals, the structure factors and pair tribution functions when suitably expressed scaling behaviour follows very well [1]. In nsition metals, in spite of the fact that the incomplete *d*-shell contributes substantially the properties, the liquid structure factors can be put into the same class of simple uid metals such as Al [2]. A large number of diffraction data on the liquid structure tors of these metals are now available in the literature [2]. A plot of structure factors, $Q)$ versus $Q/Q_{\max}$ where 'max' refers to the value of wave vector at which $S(Q)$ is ximum is shown in figure 1 and it is evident that the structure factors scale reasonably ll. It is therefore expected that the basic function i.e., the intermolecular potential ergy function should scale similarly and thereby show certain universality in the erage behaviour of different properties. But unfortunately, all the experimental ucture factor data, accessible from diffraction experiments, are devoid of accurate low data – in fact the data below $Q \simeq 1.0\,\text{Å}^{-1}$ is rarely available. Since the accuracy of the fective pair potential extracted from diffraction data depends strongly on the low Q ta [3], it is not easy to use the integral equations to extract the effective pair potential d see how the scaling property in the potential operates in these liquids. We have erefore addressed the problem somewhat indirectly. Earlier works from this laboratory ve shown that at least for the liquid 3*d*-transition metals, the simplified Wills–Harrison odel potential [4] in slightly modified form [5, 6] works quite well as far as the structure d thermodynamic properties are concerned. We have therefore thought it useful to test e model potential in some detail to see whether the effective pair potentials for various

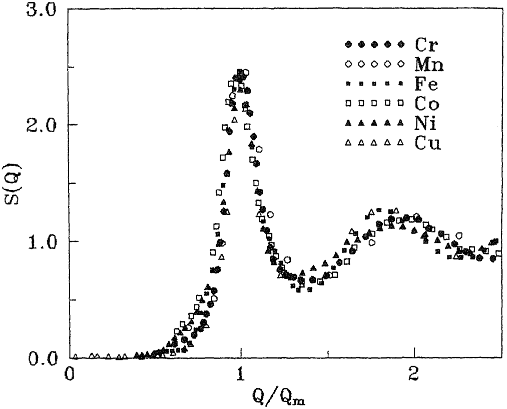

Figure 1. Scaling of experimental structure factors [2] of some 3*d*-liquid transition metal (all at or near their melting points).

members of 3*d*-series too scale properly. We have then obtained the structure factors using these potentials following the method described in ref. [6] and then Fourier transformed to obtain pair distribution functions. Both structure factors and pair distribution functions agree well with experimental data. It is also tested how these computed structure factors and pair distribution functions scale. In § 3, the scaling behaviours via the isothermal compressibility, a quantity directly linked to the long wave limit of structure factor are also investigated.

In § 4 the vacancy formation energies of several members of the 3*d*-metal series are studied via Minchin *et al* [7] formalism. These authors have given the Faber's formula [8] for the vacancy formation energies in a direct space formalism, and have applied to mono-, di- and polyvalent metals. More recently Bhatia and March [9] have used the Minchin *et al* formalism to estimate this quantity for solid argon at the melting temperature. Das *et al* [10] successfully applied the method for liquid alkali and several other metals at or near their m.p.'s. We have reinvestigated this formalism for several liquid metals of 3*d*-transition series using both one component plasma (OCP) and charged hard sphere (CHS) plasma models for reference. It is evident that vacancy formation energies of several members of 3*d*-series too scale though in somewhat limited sense.

2. W–H model for effective potential of 3*d*-liquid metals and liquid structure

m.p.

(a)

Liquid metals with solid state structure	N_c	Z_d	r_d (au)	r_c (au)
Ti (hcp)	12	2.5	2.04	1.88
Mn (bcc)	8	5.5	1.63	2.00
Fe (bcc)	8	6.5	1.51	1.61
Co (hcp)	12	7.5	1.44	1.48
Ni (fcc)	12	8.5	1.34	1.36
Cu (fcc)	12	9.5	1.266	1.09

(b)

Liquid metals	Packing density η	Charge parameter Γ
Ti	0.437	110
Mn	0.449	110
Fe	0.438	110
Co	0.444	110
Ni	0.442	110
Cu	0.450	120

repulsive contribution $u_{dd}(r)$, from the shift of the d-band centres

$$u(r) = u_s(r) + u_d(r) + u_{dd}(r). \tag{1}$$

The s-electron contribution to the pair potential is given by the Ashcroft empty core form of the bare pseudo-potential and in terms of number of s-electrons, and Ashcroft core radius, r_c the detailed expression is available in ref. [6]. In the construction of dielectric screening function same Geldart–Vosko (GV) [11] local field factor as in ref. [6] was used. The d-electron contributions are expressed in terms of the number of d-electrons, Z_d, and the d-state radii r_d; N_c is the nearest neighbour coordination number and expressions are also given in refs [4] and [6].

For all the 3d-transition metals $Z_s = 1.5$ is used in the calculation. Z_d and r_d are obtained as in ref. [4]. Values of r_c derived from the free atom s-state ionization potential lie between the two sets of values given by Wills and Harrison as pointed out earlier [6] and same values are used in the present calculations. The input parameters are listed in table 1.

The computed effective pair potentials of several liquid 3d-metals are shown in figure 2(a). The depth and position of the potential minimum are affected by the choice of r_cs, and near the minimum the potentials are dominated by the d-electron contribution. The potentials in general are stronger than typical liquid alkali metal potentials but the softness of the core potential appears almost alike. The Friedel oscillations [6] are almost absent. For comparison we have also shown the effective pair potential of liquid sodium at the melting point (m.p.) [12]. In figure 2(b) the scaled property of the effective pair potential (in respect of position and depth) for a few members of 3d-metal series is shown. The potentials are reasonably scaled.

The structure factor $S(Q)$'s obtained from effective pair potential through low order perturbation theory like random phase approximation (RPA) agree extremely well with experimental data [6]. When Fourier transformed we get pair distribution function, $g(r)$ which too agrees well with experimental data. Both $S(Q)$ and $g(r)$ are seen to scale surprisingly well. The scaling behaviour of $S(Q)$ and $g(r)$ in respect of the first peak height are depicted in figures 3(a) and (b) respectively. These functions scale reasonably even at higher temperatures (figure 3(a)).

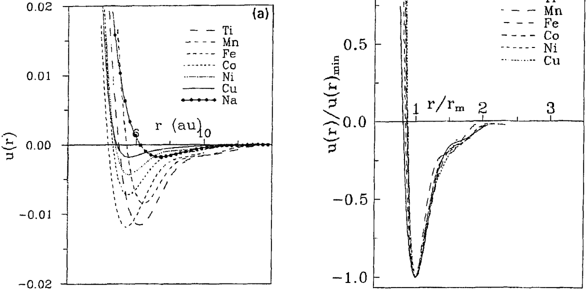

Figure 2. (**a**) Effective pair-potentials (in au) of six $3d$-liquid metals alongwith that of Na ($r_c = 1.69$ au and with GV local field); (**b**) Scaled effective pair-potential of six $3d$-liquid metals.

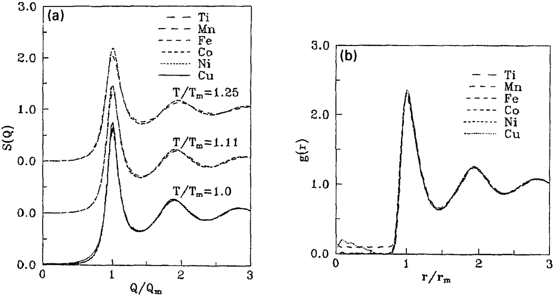

Figure 3. (**a**) Calculated $S(Q)$ vs. Q/Q_m of six $3d$-liquid metals at $T/T_{mp} = 1.0$, 1.11, 1.25. At higher temperatures $S(Q)$ is given for three metals e.g., Fe, Co, Ni. (**b**) Calculated $g(r)$ vs. r/r_m of six $3d$-liquid metals (at or near their melting points).

3. Isothermal compressibility

Isothermal compressibility, χ_T is related with the structure factor as [3]

$$S(0) = \rho k_B T \chi_T, \tag{2}$$

where $S(0)$ is the long wave limit of the structure factor $S(Q)$. Using the compressibility equation of state the scaling behaviour of the compressibility χ_T, of the $3d$-transition

Transition metals	Ti	Mn	Fe	Co	Ni	Cu	Average value
CHS plasma	0.45	0.46	0.46	0.45	0.45	0.46	0.45
Experimental	0.45	0.46	0.45	0.45	0.45	0.46	0.45
Alkali metals [1]	Li	Na	K	Cs	Rb		
CHS plasma	0.443	0.461	0.468	0.463	0.469		0.46
Experimental	0.433	0.460	0.467	0.462	0.468		0.46

liquid metals can be described in the form

$$S(0) = 1 + 4\pi\rho \int_0^\infty [g(r,T) - 1]r^2 \mathrm{d}r = 1 + \tilde{h}(0) \tag{3a}$$

or

$$\frac{\tilde{h}(0)}{\eta} = 24\sqrt{2} \int_0^\infty [g(r^*,T) - 1]r^{*2} \mathrm{d}r^*, \tag{3b}$$

which is a constant at or near m.p. because it depends only on the pair distribution function $g(r^*, T)$ which is scaled well. In eq. 3(b) $r^* = r/r_m$, r_m being the position of first $g(r)$ maximum and η is the hard core packing density. Further eq. 3(a) can be put into the form

$$S(0) = 1 + 24\sqrt{2}\eta_{\mathrm{mp}}(\rho/\rho_{\mathrm{mp}}) \int_0^\infty [g(r^*,T) - 1]r^{*2} \mathrm{d}r^*. \tag{3c}$$

This equation indicates that variation of $S(0)$ as a function of ρ/ρ_{mp} at higher temperatures should be similar for different members of the series.

Now the long wave limit structure factor $S(0)$ using the RPA expression [13] for transition metals requires the inclusion of d-electron contribution [6]. Thus,

$$S^{-1}(0) = S_0^{-1}(0) + S_s^{-1}(0) + S_d^{-1}(0), \tag{4}$$

where $S_0^{-1}(0)$ is the contribution for the reference system and in the present case it is charged hard sphere (CHS) plasma which depends on parameters η and Γ [14]. η and Γ are taken from ref. [6]. $S_s^{-1}(0)$, $S_d^{-1}(0)$ are the contributions for s- and d-electrons respectively in the long wave limit [6].

The calculated scaled values of $S(0)$ are depicted in table 2. The experimental values based on Waseda's work [2] are also shown. We also give the values for the liquid alkali metals in charged hard sphere plasma model [1]. It is to be noted that all the transition metals are scaled very well in long wave limit. The average value for $3d$-transition series are slightly smaller in magnitude in comparison with the liquid alkali metals. The experimental results also show similar difference between liquid transition and alkali metals. In figure 4 we have shown variation of $S(0)/S(0)_{\mathrm{mp}}$ as a function of ρ/ρ_{mp}, where ρ refers to number density at elevated temperature and m.p., the melting point. Γ's at

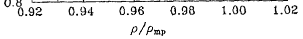

Figure 4. Plot of $S(0)/S(0)_{\mathrm{mp}}$ vs. ρ/ρ_{mp}; Ti (○ ○), Mn (□ □), Fe (△ △), Co (+ +), Ni (× ×), Cu (● ●).

higher temperatures are obtained by assuming constant Z_s and η's from an expression given by Waseda [2]. For the temperature range considered ($T/T_{\mathrm{mp}} = 1.25$ maximum), the variation of $S(0)$ is linear and almost similar for different members of $3d$-series except liquid copper. On various aspects copper appears to behave somewhat differently in comparison with other members [4]. The magnitude of the potential minimum is lowest for copper and it is lower than average thermal energy, $k_{\mathrm{B}}T$ at m.p.

4. Vacancy formation energy

A method for the vacancy formation energy of liquid metals involving pseudopotential and total pressure was evolved from this laboratory [10]. The expression could be conveniently used to compute vacancy formation energy of several simple liquid metals. The method here is extended to liquid $3d$-metals. Using the direct space formulation of Minchin *et al* [7] (which neglects atomic relaxation around a vacant lattice site) and total pressure of the liquid metals, the expression of vacancy formation energy, E_{v} is conveniently written as

$$E_{\mathrm{v}} = -k_{\mathrm{B}}T - \rho(\mathrm{d}u(\rho)/\mathrm{d}\rho) - (\rho/2)\int u(r,\rho)g(r)\mathrm{d}r$$
$$- (\rho^2/2)\int(\partial(u(r,\rho)g(r))/\partial\rho)\mathrm{d}r + (\rho^2/2)\int(\partial g(r)/\partial\rho)u(r,\rho)\mathrm{d}r, \quad (5)$$

where the terms have their usual meaning as in ref. [10]. Following Bhatia and March [9] we use the Ornstein–Zernike (OZ) relation for the direct correlation function (DCF) and after some manipulation we get the basic equation

$$\frac{E_{\mathrm{v}}}{k_{\mathrm{B}}T} = -1 - (\rho/k_{\mathrm{B}}T)(\mathrm{d}u(\rho)/\mathrm{d}\rho) - (\rho/2)[(\partial S^{-1}(0)/\partial\rho) + (\partial c(r=0)/\partial\rho)]$$
$$+ (\rho^2/2k_{\mathrm{B}}T)\int(\partial g(r)/\partial\rho)u(r,\rho)\mathrm{d}r, \quad (6)$$

where $c(r=0)$ is the direct correlation function evaluated at $r=0$. $c(r=0)$ can easily be evaluated knowing $c_0(r)$, the reference part and $c_{\mathrm{RPA}}(r=0)$ from the knowledge of

Fe	1823	11.20	8.79	6.07	—	10.12
Co	1823	11.65	12.83	10.30	12.20	8.16
Ni	1773	11.73	9.30	6.52	11.25	9.41
Cu	1423	10.98	14.42	9.53	8.00	11.26
Average values:			10.09	7.02	9.24	9.64

indirect s- and d-electron mediated part in RPA. We use $c_0(r)$ for two closely related electron-ion plasma models for liquid metals, namely, the one component plasma (OCP) model of Baus and Hansen [15] as modified by Evans and Sluckin [13] and the charged hard sphere (CHS) plasma model [14].

The expressions for $c_0(r=0)$ in the two electron-ion plasma models are given in [10]. The $c_{\mathrm{RPA}}(r=0)$ term is given by

$$c_{\mathrm{RPA}}(r=0) = -\beta/(2\pi^2)\int v(Q)Q^2\mathrm{d}\mathbf{Q}, \tag{7}$$

where $v(Q)$ has now been arising from the contributions of s- and d-electron interactions (§ 2). The expressions for $S_0(0)$ for the two models given in ref. [10] plus the d-electron terms of § 3 constitute $S(0)$. The volume dependent but structure independent energy has the same functional form as in ref. [10] but the expression for electron gas free energy, F_{eg} is now given as

$$F_{\mathrm{eg}} = \frac{Z_s}{2}\left[0.982/r_s^2 - 0.712/r_s + 0.031\ln r_s - 0.115 - 2\left(\frac{\pi k_{\mathrm{B}}}{Q_f}\right)^2\right] - \frac{\pi^2}{3}k_{\mathrm{B}}^2 n(E_f), \tag{8}$$

where the terms have their usual meaning as in ref. [6].

Now in (6) the last term is structure dependent and can be called structural term while the rest of the terms are in fact thermodynamic terms [16]. So we can put

$$E_{\mathrm{v}}/k_{\mathrm{B}}T = E_{\mathrm{v}}^{\mathrm{therm}}/k_{\mathrm{B}}T + E_{\mathrm{v}}^{\mathrm{struct}}/k_{\mathrm{B}}T. \tag{9}$$

It is in general found that the structural term has minor contribution ($E_{\mathrm{v}}^{\mathrm{struct}}/k_{\mathrm{B}}T < 1$) to the vacancy formation energy and the major part is contributed by the thermodynamical terms [16]. Assuming Egelstaff's uniform fluid model [17] as in ref. [10] this can be shown to be approximately the case. We have therefore computed here the thermodynamic part only and make the comparison with experimental results. The computed results alongwith the experimental values are shown in table 3. The input parameters are all taken as in §§ 2 and 3. The results for CHS plasma model are in general a little bigger than the values for OCP model. The model results agree fairly well with experimental results. The average calculated E_v/k_BT values for the two plasma models come out to be about 10.1 and 7.0 respectively. The results are better than those of Alonso and March [18] for liquid transition metals at their m.p's. The average experimental value (for 5 metals for which vacancy formation energies are available) is about 9.64. Our earlier calculation showed for alkalis (bcc) except for Li an average, E_v/k_BT as 15.6 and 12.2 for CHS and OCP models respectively. The average experimental value is 12.2. For close packed lattice (both non-transition and transition metals) observed $E_v/k_BT \sim$ 8–9. Rashid and March [16] have sought to connect this term i.e., E_v/k_BT at m.p. to the corresponding crystal lattice structure. Thus, the present calculation shows some agreement with the proposition of Rashid and March. The graph E_v vs T is approximately linear (not shown) indicating a moderate scaling behaviour for vacancy formation energy for 3*d*-liquid metals.

5. Conclusion

The W–H model for liquid transition metals is easily applicable effective pair potential model for the study of various structural and thermodynamic properties of liquid 3*d*-transition metals. The effective pair potentials of this series are scaled well. The structure factors $S(Q)$ calculated in RPA and pair distribution functions $g(r)$ also scale surprisingly well. The long wave limit of structure factor $S(0)$ and its equivalent expression $\eta\tilde{h}(0)^{-1}$ is found to be constant which indicates again a good scaling behaviour and difference with liquid alkali metals is evident.

The experimental liquid structure factor data for several members of 3*d*-series depicted in figure 1 however show limited scaling. It is clear that there exist some limitations in spite of the fact that all the data shown here are due to Waseda's single-set measurements and accuracies in $S(Q)$ and $g(r)$ were claimed about 4%. The coordination numbers evaluated from these data varied between 10.6 and 11.6 for different members of the series indicating good similarity of nearest neighbour structures in the liquid state. The solid state structures, however are different either fcc/hcp or bcc for different members of 3*d*-series. Similar is the case with evaluated hard core packing densities which varied between 0.44 and 0.45 except for Ti and V indicating once again the similarity with limited variations. As pointed out by Waseda and Tamaki [2] the measurements in this kind of work, particularly in the data collection, were affected by the experimental difficulties arising from the high temperatures due to active chemical reactivity of the liquid samples compared to measurements at lower temperature (below 1373 K). In this connection we would also like to mention that the experimental liquid structure factor data of alkali metals too show the scaling property with limitations among various members of the series [1]. So the scaling depicted in figure 1 for liquid 3*d*-series is not unreasonable.

We have also applied W-H model potential to obtain vacancy formation energies of several liquid 3*d*-metals in Minchin *et al* formalism. We have evaluated the thermodynamic part only and the average value agrees fairly well with the known average values for the 3*d*-series. Here also scaling is evident and difference from liquid alkali metals is clear, probably implying the structural distinctions of the two

Acknowledgements

The authors are grateful to CSIR, New Delhi and IUC-DAEF, Indore for financ
support.

References

[1] M J Huijben and W van der Lugt, *Acta Crystallogr.* **A35**, 431 (1979)
N Matsuda, H Mori, K Hoshino and M Watabe, *J. Phys. Condens. Matter* **3**, 827 (1991)
A Bari, P Pal and R N Joarder, *Pramana – J. Phys.* **42**, 395 (1994)
[2] Y Waseda and S Ueno, *Sci. Rep. Res. Inst. Tohuku Univ.* **A34**, 15 (1987)
Y Waseda, *The structure of non-crystalline materials* (Mc-Graw Hill, New York, 1980)
Y Waseda and S Tamaki, *Philos. Mag.* **32**, 273 (1975)
[3] N H March, *Liquid metals* (Pergamon Press, London, 1968)
[4] J M Wills and W A Harrison, *Phys. Rev.* **B28**, 4363 (1983)
[5] C Hausleitner and J Hafner, *J. Phys.* **F18**, 1025 (1988)
[6] A Bari, T Das and R N Joarder, *J. Non-Cryst. Solids* **136**, 173 (1991)
A Bari and R N Joarder, *Indian J. Pure Appl. Phys.* **30**, 256 (1992)
[7] P Minchin, A Meyer and W H Young, *J. Phys.* **F4**, 2117 (1974)
[8] T E Faber, *An introduction to the theory of liquid metals* (Cambridge University Press, Lonc
and New York, 1972)
[9] A B Bhatia and N H March, *J. Chem. Phys.* **80**, 2076 (1984)
[10] T Das, T Nammalvar, L B Bhuiyan and R N Joarder, *Phys. Status Solidi* **B157**, 93 (1990
[11] D J W Geldart and S H Vosko, *Can. J. Phys.* **44**, 2137 (1966)
[12] N W Ashcroft, *Phys. Lett.* **23**, 48 (1966)
[13] R Evans and T J Slukin, *J. Phys.* **C14**, 3137 (1981)
[14] T Das, A Bari and R N Joarder, *Indian J. Pure Appl. Phys.* **27**, 37 (1989)
[15] M Baus and J P Hansen, *Phys. Rep.* **59**, 1 (1980)
[16] R I M A Rashid and N H March, *Phys. Chem. Liquids* **19**, 41 (1989)
[17] P A Egelstaff, D I Page and C R T Heard, *J. Phys.* **C4**, 1453 (1971)
[18] J A Alonso and N H March, *Phys. Chem. Liquids* **20**, 235 (1989)

—journal of
physics

© Printed in India

Vol. 50, No. 1,
January 1998
pp. 11–23

Evidence of polaronic charge carriers in oxide superconductors

C M SRIVASTAVA
Department of Physics, Indian Institute of Technology, Powai, Mumbai 400076, India

MS received 20 September 1997

Abstract. The analysis of photoemission and femtosecond optical absorption spectroscopy in oxide superconductors supports the view that the charge carriers are polaronic in nature. These carriers are found to exist in the (Ba/Sr)–O planes and are coupled to B_{1g} vibrations of the apical oxygen.

Keywords. Optical properties of high T_c compounds; polaronic charge carriers.

PACS Nos **74.20; 74.25**

1. Introduction

The nature of the charge carriers in high T_c superconductors has been a subject of extensive investigations [1–4]. We have proposed that the normal state properties of copper-oxide superconductors can be understood on the polaronic model of the charge carrier [5]. Recently Zhao *et al* [2] through the study of isotope effect of the number density and London penetration depth have found evidence of polaronic charge carriers in $La_{2-x}Sr_xCuO_4$. Shen and Schrieffer [3] have observed two types of excitations in their angle resolved photoemission spectroscopy (ARPES) of Bi(2212), one has a nearly Lorentzian shape and is attributed to a quasi-particle and the other has a broad feature with an edge type opening near the Fermi surface which they attribute to a collective mode of excitation. These line shapes of the excitations are dependent on the temperature, level of doping, and momentum of the excitations. Campuzano *et al* [6] have carried out ARPES studies on $YBa_2Cu_3O_{6.9}$ and have mapped the Fermi surfaces which are in agreement with the calculations made using the local-density approximation. Similar measurements have been made for Bi (2212) by Marshall *et al* [7] and they find hole pockets centred at (π, π). The underdoped sample with less hole has Fermi level crossings over a small portion compared to the overdoped sample and its Fermi surface does not extend to the Brillioun zone (BZ) edge. The lowest binding energy edge is shifted from the Fermi surface by about 20–30 meV as in ref. [3]. There exist several femtosecond pump-probe optical absorption studies on high T_c superconducting and nonsuperconductthe nonsuperconducting YBCO sample.

We have shown that phenomenological description of the normal state of Cu–O high temperature superconductors in terms of q independent polarizability proposed by Varma *et al* [1] follows from the short range cooperative electron–phonon coupling which produces correlated polarons in mixed valence compounds [5]. We use this approach and show that the ARPES and optical absorption results are satisfactorily explained on the basis that both large and small polarons coexist in high-T_c materials and their weight is dependent on the doping concentration, temperature and momentum of the excitation.

2. The model

We begin with the Holstein molecular crystal model [10] and consider diagonal electron–phonon coupling. Taking independent Einstein oscillators having frequency ω_0,

$$\begin{aligned} H = {} & \sum_{i\cdot\sigma} \epsilon_i c^+_{i,\sigma} c_{i,\sigma} + \sum_{i\cdot j\sigma} t_{ij}(c^+_{i+j\sigma} c_{i,\sigma} + c^+_{i,\sigma} c_{i+j\sigma}) + U\sum_i n_{i\uparrow} n_{i\downarrow} \\ & - \lambda \sum_{i\cdot\sigma} c^+_{i,\sigma} c_{i,\sigma} u_i + M/2 \sum_i (u_i^2 + \omega_0^2 u_i^2), \end{aligned} \tag{1}$$

where t_{ij} denotes the bare electron hopping integral from site i to all j sites that are available for hopping, λ is the electron-lattice coupling constant, $n_i = c_i^+ c_i$, M is the mass of the ions and u_i their displacement from equilibrium, $c^+_{i\sigma}(c_{i\sigma})$ denotes the creation (annhilation) operator for the electron with spin σ at site i.

Using the canonical polaron transformation

$$H \to H' = \mathrm{e}^{iS} H \mathrm{e}^{-iS}, \tag{2}$$

$$S = \sum_i \frac{\lambda(a_i - a_i^+)(n_{i\uparrow} + n_{i\downarrow})}{\hbar\omega_0 (2M\omega_0/\hbar)^{1/2}}, \tag{3}$$

where a_i^+ (a_i) denotes the creation annihilation operator for the local Einstein oscillators and

$$u_i = \frac{a_i^+ + a_i}{\sqrt{2M\omega_0/\hbar}}. \tag{4}$$

We obtain

$$\begin{aligned} H = {} & \sum_{i\sigma} (\epsilon_i - \epsilon_p) l^+_{i\sigma} l_{i\sigma} + \sum_i \hbar\omega_0 (a_i^+ a_i + \tfrac{1}{2}) + \sum_{i,\sigma} (U - 2\epsilon_p) n_{i\uparrow} n_{i\downarrow} \\ & + \sum_{i,j} t_{ij} (l_i^+ l_{i+j} x_{i,i+j} + l^+_{i+j} l_i x_{i+j,i}) \end{aligned} \tag{5}$$

where

$$l_i^+ = \mathrm{e}^{iS} c_i^+, \tag{6}$$

$$t_{ij} x_{i,i+j} = t \exp\left\{ \frac{\epsilon_p}{\hbar\omega_0} [(a_i - a_i^+) - (a_j - a_j^+)] \right\}, \tag{7}$$

$$\epsilon_p = \lambda^2/2M\omega_0^2 \tag{8}$$

is the polaron binding energy and $2\epsilon_p$ is the polaron–polaron attraction energy. It can be readily shown that there are two different types of solutions, one band type and the other localized.

The energy of the band type polaron is

$$E_k = -2J + Jk^2 \tag{9}$$

and that of the localized state is

$$E_l = -2J - (\lambda^2/2M\omega_0^2) = -2J - \epsilon_p. \tag{10}$$

We consider that the localized electrons and holes are symmetric about the chemical potential, μ, so the energy diagram as shown in figure 1 holds. In eqs (9) and (10)

$$J = t\exp[-s(n_q)], \tag{11}$$

where (n_q) denotes the set of oscillator occupation numbers,

$$s(n_q) = (1/\pi)\int_0^{\pi}(1+2n_q)r_q\,\mathrm{d}q, \tag{12}$$

$$r_q = (\lambda^2/2M\omega_0^2\hbar\omega_0)(1-\cos \underline{q}\cdot(\underline{X}_i - \underline{X}_{i+j})), \tag{13}$$

$$n_q = [\exp(\hbar\omega_0\beta)-1]^{-1}, \quad \beta = 1/k_{\mathrm{B}}T. \tag{14}$$

From figure 1 the localized hole states are $2\epsilon_p$ below the bottom of the polaron band while localized electron states are at the bottom of the band. The hole and electron states arise in homogenous mixed valence compound with the metallic ions in A^{n+} and A^{n+1} and anions in B^{m-} and $B^{(m+1)-}$ states. In a compound like Bi(2212) with some O^{-1} ions present in the lattice, 2D primitive cell of SrO, assuming that mixed valence cation and anion states exist in this plane, will be constituted by two blocks as shown in figure 2. Coupling with LO phonon modes with ion displacements normal to the plane along the

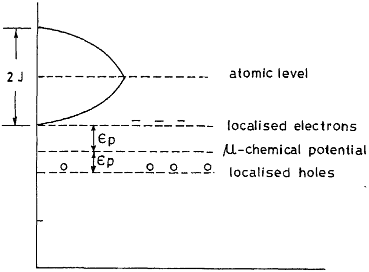

Figure 1. Energy level diagram for localized small polaron.

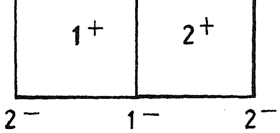

Figure 2. Location of charges on Sr–O4 plane.

Bi^{3+}–O4–Cu^{2+} bond, will couple 1^-, 2^- and 2^+, 1^+ states through electron and hole transport as discussed in ref. [11] and will lower the energy of the system due to asymmetry of the charges in the bond. In this process $\underline{q}$ is nearly normal to the plane containing the $\underline{X}_i$ and $\underline{X}_{i+j}$ vectors and leads to near vanishing of r_q in eq. (13) so there are no Frank–Condon transitions. Consequently there is no narrowing of the polaron bandwidth with temperature and no increase in the effective mass of the electron [11]. This case was discussed by us in terms of two degenerate states $\psi_{\rm I} = \sqrt{N}\exp(i\phi_{\rm I})$ and $\psi_{\rm II} = \sqrt{N}\exp(i\phi_{\rm II})$ related by the phase difference $\phi_{\rm I} - \phi_{\rm II} = \pi/2$ and coupled via the phonon energy $\hbar\omega_0$. For this case there is no activation energy in the expression for dc conductivity.

3. Band and hopping conductivity

We now obtain the expressions for optical absorption coefficeint $\Gamma(\omega)$ on the polaronic model to explain the results of the ARPES and femtosecond optical absorption studies. We assume that the small polaron band states behave approximately the same way as free states of large polaron in the continuum approximation. The treatment of Kartheuser [12] which considers the electrons initially at rest is applicable to the present case and the absorption constant is given by

$$\Gamma(\omega)=\frac{1}{\epsilon_0 c n(w)}\cdot\frac{2}{3}\alpha\left(\frac{m^*}{m}\right)^{3/2}\frac{\left[\frac{\omega}{\omega_0}-1\right]^{1/2}}{\left[\frac{\omega}{\omega_0}\right]^{3}}\exp\left[-\frac{m^*}{m}\cdot\frac{\alpha}{12}\left(\frac{\omega}{\omega_0}-1\right)\right]. \tag{15}$$

Here ϵ_0 is the dielectric constant of vacuum, $n(\omega)$ is the index of refraction, c is the velocity of light, ω_0 is the LO phonon frequency to which the electron is coupled and α is the dimensionless coupling constant

$$\alpha=\frac{1}{2}\frac{e^2}{(\hbar/2m\omega_0)^{1/2}}\frac{1}{\hbar\omega_0}\left(\frac{1}{\epsilon_\infty}-\frac{1}{\epsilon_0}\right). \tag{16}$$

A general approach using density matrix gives

$$\Gamma(\omega)=\frac{1}{\epsilon_0 c n(\omega)}{\rm Re}(\sigma_{ij}), \tag{17}$$

site $i+j$ is given by

$$\overset{\leftrightarrow}{\sigma}^i(\omega,T)=\overset{\leftrightarrow}{\sigma}^i(O,T)\frac{\sinh(\hbar\omega\beta/2)}{(\hbar\omega\beta/2)}\frac{\exp(-\xi_i^2\tau_i^2\eta_i)}{\left[1+(2\xi_i\omega_0\tau_i^2)^2\right]^{1/4}}, \tag{18}$$

where

$$\xi_i=\hbar\omega+\epsilon_{i+j}-\epsilon_i, \tag{19}$$

$$\eta_i=\frac{2}{p_i}\ln\{p_i+(1+p_i^2)^2\}^{1/2}-\frac{2}{p_i^2}\{[1+p_i^2]^{1/2}-1\}, \tag{20}$$

$$p_i=2(\omega_0\xi_i\tau_i^2), \tag{20a}$$

and

$$\frac{1}{\tau_i^2}=\frac{4\alpha(q)\sin^2 l_2(q\cdot(\underline{X}_i-\underline{X}_{i+j}))\cdot\omega_0^2}{\sinh(\hbar\omega_0\beta/2)}. \tag{21}$$

The contribution to dc conductivity is given by

$$\begin{aligned}\overset{\leftrightarrow}{\sigma}^i(O,T)=&\frac{\pi^{1/2}}{4}\frac{e^2c_ec_hJ^2}{\hbar^2}(\underline{X}_i-\underline{X}_{i+j})(\underline{X}_i-\underline{X}_{i+j})\\ &\times\operatorname{sech}((\epsilon_{i+j}-\mu)\beta/2)\operatorname{sech}((\epsilon_i-\mu)\beta/2)\\ &\times\beta\tau_i\exp(-2\alpha(q)\sin^2\tfrac{1}{2}(q(x_i-x_{i+j}))\tanh\hbar\omega_0\beta/2).\end{aligned} \tag{22}$$

Here c_h, c_e are the probability of occupation of sites i and $i+j$ by hole and electron respectively and $\epsilon_{i+j}-\mu=+\epsilon_p$ and $\epsilon_{i+j}-\mu=-\epsilon_p$ as shown in figure 1. In the present case with q of the LO phonon normal to the vector $(X_i-X_{i+j}), \tau_i^{-1}=\omega_0$ and $J\sim\hbar\omega_0$, we obtain for a square lattice with coordination number $z=4$, the expression for the dc conductivity for the correlated polarons,

$$\sigma_c(O,T)=\frac{\pi^{1/2}}{2}nc_ec_ha^2e^2\omega_0\beta\operatorname{sech}^2(\epsilon_p\beta/2), \tag{23}$$

where n is the number of ions in the mixed valence state. The optical conductivity can be expressed as [1]

$$\sigma_c(\omega,T)=\sigma_{c1}(\omega,T)+\sigma_{c2}(\omega,T). \tag{24}$$

The low frequency optical conductivity is obtained from eq. (18) when the electron absorbs the photon and emits it without Frank–Condon (FC) transition,

$$\epsilon_i=\hbar\omega+\epsilon_p\quad\text{and}\quad\epsilon_{i+j}=\epsilon_p. \tag{25}$$

So $\xi=0$. Then from eq. (19)

$$\sigma_{c1}(\omega,T)=\sigma_c(O,T)\frac{\sinh(\hbar\omega\beta/2)}{(\hbar\omega\beta/2)}\cdot\frac{\cosh(\epsilon_p\beta/2)}{\cosh((\epsilon_p+\hbar\omega)\beta/2)}. \tag{26}$$

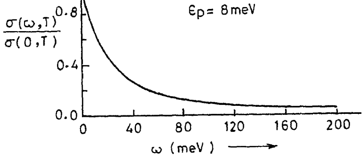

Figure 3. Drude type contribution to optical conductivity from eq. (26) for $\varepsilon_p = 8\,\text{meV}$ and $T = 100\,\text{K}$.

This is Drude type contribution and as shown in figure 3 monotonically decreases with increase in ω.

The second component is obtained for those processes in which the FC transition occurs,

$$\epsilon_i = \hbar\omega - \epsilon_p, \quad \epsilon_{i+j} = \epsilon_p, \quad \xi_i = 2\epsilon_p, \tag{27}$$

$$\begin{aligned}\sigma_{c2} &= \frac{\pi^{1/2}}{2}\frac{e^2 c_e c_h}{\hbar^2} J'^2 a^2 e^2 \beta\tau' \operatorname{sech}(\epsilon_p\beta/2)\operatorname{sech}((\hbar\omega - \epsilon_p)\beta/2) \\ &\quad\times \frac{\sinh(\hbar\omega\beta/2)}{(\hbar\omega\beta/2)} \frac{\exp(-4\epsilon_p^2\tau'^2\eta/\hbar^2)}{[1 + (4\epsilon_p\omega_0\tau'^2/\hbar)^2]^{1/4}} \quad \text{for } \omega > 2\epsilon_p \\ &= 0 \quad \text{for } \omega \leq 2\epsilon_p.\end{aligned} \tag{28}$$

For $\omega > 2\epsilon_p$, we take

$$J' = \hbar(\omega_0^2 + \omega^2)^{1/2} \quad \text{and } \tau'^{-1} = \omega_0\left(1 + \frac{\omega^2}{4\omega_0^2}\right). \tag{29}$$

This gives

$$\begin{aligned}\frac{\sigma_{c2}(\omega, T)}{\sigma_{c2}(O, T)} &= \frac{\sinh(\hbar\omega\beta/2)}{(\hbar\omega\beta/2)}\operatorname{sech}((\hbar\omega - \epsilon_p)\beta/2)\cosh(\epsilon_p\beta/2) \\ &\quad\times \left(1 + \frac{\omega^2}{\omega_0^2}\right)\left[\left(1 + \frac{\omega^2}{4\omega_0^2}\right)^{-1}\left(1 + \frac{4\epsilon_p}{\hbar\omega_0\left(1 + \frac{\omega^2}{4\omega_0^2}\right)}\right)^{2}\right]^{-1/4} \\ &\quad\times \exp\left[-\frac{4\epsilon_p^2\eta}{\hbar^2\omega_0^2\left(1 + \frac{\omega^2}{4\omega_0^2}\right)}\right].\end{aligned} \tag{30}$$

The relative contributions to optical conductivity from $\sigma_{c1}(\omega, T)$ and $\sigma_{c2}(\omega, T)$ have to be determined from experiment. The nature of $\sigma_{c2}(\omega, T)$ curve in eq. (30) agrees well with that found emperically by Varma *et al* [1] for $YBa_2Cu_3O_{7-\delta}$.

We now examine the data on optical absorption, photoemission spectroscopy and femtosecond absorption in high T_c superconductors and show that these can be satisfactorily explained on the model developed above.

4.1 *Optical conductivity*

The optical conductivity of all oxide superconductors seems to be composed of Drude-like free carrier peak centered at zero frequency and a broad mid-infrared absorption band centered nearly at $2000\,\mathrm{cm}^{-1}$. Reedyk *et al* [14] have obtained the optical conductivity of Bi(2212) from the reflectance data. The normal state conductivity is dominated by a peak at zero frequency representing the Drude contribution. Also there are two broad peaks, one near $412\,\mathrm{cm}^{-1}$ and another at $996\,\mathrm{cm}^{-1}$. As discussed by Cardona *et al* [15], the polarized Raman spectra of Bi(2212) show a broad stretching mode of B_{1g} symmetry at $480\,\mathrm{cm}^{-1}$ corresponding mainly to the vibrations of the apical oxygen O4 in the Cu–O–Bi bonds. The dc resistivity measurements of Crommie and Zettl [16] on Bi(2212) have been used to obtain values of ϵ_p and n from eq. (23). The sample with linear temperature dependence of the resisitivity gives $n \simeq 0.25$ charge carriers per Sr atom and $\epsilon_p = 8$ meV. For the Drude contribution we obtain [5]

$$\omega_{pD}^2 = 4\pi n_{\mathrm{eff}}\, e^2/m^* = 4\pi\sigma(O,T), \tag{31}$$

$$n_{\mathrm{eff}} = \frac{\sqrt{\pi}}{2} n c_e c_h \,\mathrm{sech}^2(\epsilon_p\beta/2) \tag{31a}$$

and

$$\Gamma_D^{-1} = a^2\omega_0\beta m^*. \tag{31b}$$

The resistivity of Bi(2212) at 100 K is 120 μΩ-cm. This gives $\omega_{pD} = 6190\,\mathrm{cm}^{-1}$ and $\Gamma_D = 67\,\mathrm{cm}^{-1}$ assuming m^* nearly equal to the electron mass. These values are close to those obtained in ref. [14] from optical reflectance data.

The expression for $\sigma_{c2}(\omega, T)$ in eq. (30) applies for the correlated localized polarons when $\omega > 2\epsilon_p$. These act as oscillators having center frequency ω_0 which for Bi(2212) is $480\,\mathrm{cm}^{-1}$. There are localized as well as free polarons as shown in figure 1. The optical absorption for free polaron is given by eq. (15) while that for localized polaron is given by eqs (17) and (18). Therefore there are three types of contributions to optical conductivity; (i) Drude eq. (26), (ii) zero phonon scattering from localized polaron eq. (30) and (iii) one phonon (and higher phonon) scattering processes from free polaron states (eq. 15).

The threshold for low frequency process (ii) in Bi(2212) is at 16 meV which is observed by Reedyk *et al* [14]. The broad peak at $412\,\mathrm{cm}^{-1}$ arises both from (ii) and (iii) and the one at $996\,\mathrm{cm}^{-1}$ arises from (iii) for a two-phonon scattering process which has a threshold at $960\,\mathrm{cm}^{-1}$ and a maximum at $996\,\mathrm{cm}^{-1}$.

4.2 *Photoemission spectroscopy*

The angle resolved photoemission spectra (ARPES) of high-T_c superconductors has not been understood despite several attempts [3, 7, 8]. There are however some systematics that are emerging from these studies. In underdoped samples of $Bi_2Sr_2CaCu_2O_{8+\delta}$ a broad feature is always present at 100–200 MeV in the spectra taken near $(\pi, 0)$. Recently Shen and Schrieffer [3] have found that this feature is absent for overdoped samples along ΓS and XS directions of the Fermi surface (FS) while it is absent only along ΓS direction in the underdoped samples. They believe that this is due to strong dressing of the photohole for $k \simeq (\pi, 0)$ in the underdoped samples.

The difficulty in the interpretation of the angle-resolved photoemission spectra of high T_c superconductors has been discussed by Mott [17]. Generally ARPES enables a Fermi surface to be mapped and the results are similar to band calculations. However in a doped semiconductor where holes near the Fermi surface drop down and form bosons there are no states available near the FS, so no excitation occurs and the spectrum does not map the FS. Following Mott we then look for the dynamical feature of the charge carriers in the ARPES spectrum of the high T_c superconductors.

The localized hole states are below the bottom of the polaron band by $2\epsilon_p$ as shown in figure 1. This is 16 meV in Bi (2212). The bottom of the polaron band is below the atomic level by $\hbar\omega_0 = 60$ meV in this system. In the photoemission spectroscopy the one-phonon optical absorption band following eq. (15) should peak at $\omega = \omega_0 = 60$ meV. But as in the ground state the polarons are in the localized state below the polaron band, the one phonon line appears at 16 meV below the Fermi surface. The line shape for the quasi-like excitation is given by eq. (15). In figures 4(a, b, c) we have plotted the intensity of absorption from eq. (15) with $\omega_0 = 60$ meV and $\alpha = 2.5$, 1, 0.75 and compared them with the ARPES data of ref. [3] for overdoped Γ-S, X-S and underdoped Γ-S directed free polaron energy distribution curves, respectively. It follows that the electron–phonon coupling is stronger in the overdoped compared to the underdoped sample. The polaron along X-S in the

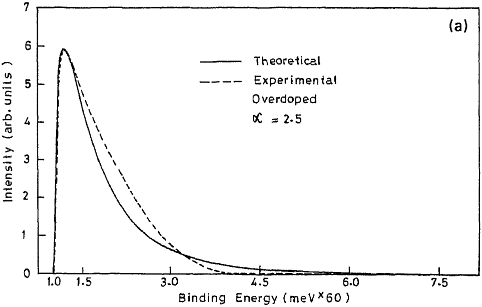

Figure 4(a). Energy distribution curve along Γ-S symmetry direction in the Brillouin zone of Bi(2212). The experimental data is taken from ref. [3] for the overdoped samples. The theoretical curve is from eq. (15) with $m^*/m = (1 - \alpha/6)^{-1}$ and $\alpha = 2.5$. The binding energy is in terms of optical phonon energy $\hbar\omega_0$ where ω_0 is

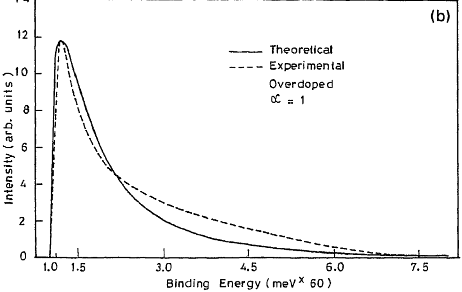

Figure 4(b). Energy distribution curve along X-S symmetry direction in the Brillouin zone of Bi(2212). The experimental data is taken from ref. [3] for the overdoped samples. The theoretical curve is from eq. (15) with $m^*/m = (1 - \alpha/6)^{-1}$ and $\alpha = 1$. The binding energy is in terms of optical phonon energy $\hbar\omega_0$, where ω_0 is the frequency of Bi^{3+}–O4–Cu^{2+} bond stretching vibrational mode of B_{1g} symmetry and is taken as $480\,cm^{-1}$ from ref. [15].

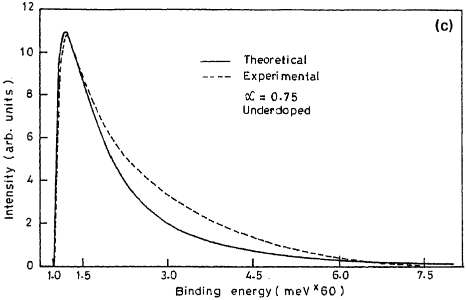

Figure 4(c). Energy distribution curve along Γ-S symmetry direction in the Brillouin zone of Bi(2212). The experimental data is taken from ref. [3] for the underdoped samples. The theoretical curve is from eq. (15) with $m^*/m = (1 - \alpha/6)^{-1}$ and $\alpha = 0.75$. The binding energy is in terms of optical phonon energy $\hbar\omega_0$, where ω_0 is the frequency of Bi^{3+}–O4–Cu^{2+} bond stretching vibrational mode of B_{1g} symmetry and is taken as $480\,cm^{-1}$ from ref. [15].

underdoped is localized and its line shape is given by the contribution from eq. (30) with additional contributions from multi-phonon processes adding at binding energies,

$$\Gamma(\theta)\alpha \sum_{n_{i=1}} \sigma_2^{n_i} \left(\frac{\omega}{n_i\omega_0}, T \right) \zeta(\omega - n_i\omega_0), \tag{32}$$

where $\zeta(\phi)$ is a step function

$$\begin{aligned} \zeta(\phi) &= 0 \quad \text{for } \phi \leq 0 \\ &= 1 \quad \text{for } \phi > 1. \end{aligned} \tag{32a}$$

This accounts for the broadness of this line. Later we show that evidence of multi phonon processes exist in femtosecond absorption studies.

In several studies of photoemission spectrum hole pockets at (π, π) have been reported which are consistent with the transport and optical data. For underdoped samples, Marshall *et al* [7] found in Bi(2212), clear Fermi level crossings along the Γ-S line but over small portions of the BZ and its Fermi surface does not extend to the BZ edge.

In the present model with O4 in the Sr-O plane in Bi(2212) the hole pockets are centered at the Sr atoms. From figure 2 it can be seen that the charge transport from one Sr atom to a neighbouring Sr atom can take place along the XS direction and to O atom along the Γ-S direction if O and Sr are both in mixed valence states and charge transport is produced due to the modulation of the Modelung energy by optical phonons [11]. In the underdoped samples with less number of holes the polaron state, that move along the XS direction from one Sr atom to another, cease to exist in the normal state and the polaron along this direction tend to localize. On entering the superconducting phase the polarons along this direction become delocalized and connect the hole pockets centered at (π, π) in the unit cells.

In figure 2 linear chains of $(2^- \, 2^+ \, 2^-)$ and $(1^- \, 1^+ \, 1^- ..)$ ions are seen in (1 1 0) direction. These alternate chains exchange their charge states when coupled with phonon at a frequency comparable to the phonon frequency. As argued by Shen and Schrieffer [3] if a photohole is created in these chains it excites a collective mode along (π, π) to attain the equilibrium state.

4.3 *Femtosecond optical absorption*

Femtosecond pump-probe measurements performed on Y-123, Bi(2223) and non-superconducting, $YBa_2Cu_3O_{6+y}$ $(y < 0.4)$ for sample temperature ranging from 7 K to 300 K have been reported by Chwalek *et al* [8]. The observations are made in transmission on thin films with a laser that produced pulses of ~100 fs duration at 100 MHz repetition rate and a wavelength of 630 nm (1.98 eV). The change in refractive index was measured by passing a second beam polarized perpendicular to the pump beam. The change in transmissivity was recorded versus the pump-probe delay time.

The experiment relates to the observation of the cross-modulation produced by the thermomodulation process. We take that the modulation is produced by the polarons whose frequency, ω_0, of the order of 50 meV is small compared to the laser frequency Ω (~1 eV). For large Ω, the refractive index n is given by

$$n(\Omega + \omega) = 1 - \frac{\omega_p^2}{(\Omega + \omega)^2}, \tag{33}$$

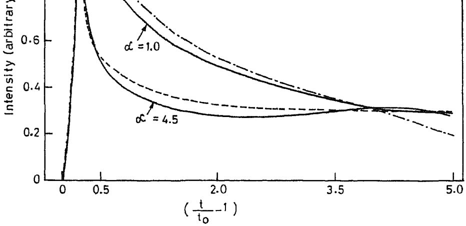

Figure 5. Transmissivity change normalized to unity is plotted relative to the pump-probe delay time for the Bi(2223) film at 8 K and 202 K. The experimental data is taken from ref. [8]. The theoretical curves are obtained from eq. (15) with $m^*/m = (1 - \alpha/6)^{-1}$ and assuming that $(\omega/\omega_0 - 1) \propto$ the normalized delay time $(t/t_0 - 1)$ (eq. (34)). α for the theoretical curve for the superconducting phase ($T = 8$ K) is 1, and nonsuperconducting phase ($T = 202$ K) is 4.5.

where ω_p is the plasma frequency. It can be readily shown that

$$\frac{n(\Omega+\omega)}{n(\Omega+\omega_0)} - 1 \propto \left(\frac{\omega_p}{\Omega}\right)^2 \left(\frac{\omega_0}{\Omega}\right) \left(\frac{\omega}{\omega_0} - 1\right) = \frac{t - t_0}{t_0}, \tag{34}$$

where $(t - t_0)$ is the pulse delay time and t_0 is the reference time taken as the time of maximum transmissivity.

In figure 5 we show the transmissivity change normalized to unity plotted relative to the pump-probe delay time for the Bi(2223) film at 100 K from ref. [8]. The theoretical plot is obtained on the assumptions that at low energies only free polarons are excited but when ω exceeds 1.5 ω_0 localized polarons are also excited. We then can write with $\theta = \omega/\omega_0$,

$$\Gamma(\theta) = \Gamma(t/t_0) = cn\epsilon_0[a_1\Gamma_1(\theta) + a_2\Gamma_2(\theta)], \tag{35}$$

where $\Gamma_1(\theta)$ is given by eq. (15) and $\Gamma_2(\theta)$ is given by eq. (17) with $\sigma(\omega, T)$ given by eq. (30). We take a_2 as zero for $\theta \leq 1.5$ and gradually increasing for $\theta \geq 1.5$,

$$\begin{aligned} a_2 &= \left(\frac{\theta - 1.5}{6}\right)^{1/2} && \text{for } \theta > 1.5 \\ &= 0 && \text{for } \theta \leq 1.5. \end{aligned} \tag{36}$$

a_1 simply normalizes the contribution from free polarons to its maximum value near $\theta = 1$ and is 0.68. There appears to be a good agreement for $\alpha = 4.5$ for the free polarons.

A similar analysis of the spectra of the same sample at 8 K when it is superconducting shows that $a_1 = a_2 = 1$ and α is 1.0 in this state. Consequently there is a delay in the rising edge near Ops and the line is much broader as shown in figure 5. Since, in eq. (16), $(\hbar/2m\omega_0)^{1/2}$ is a measure of the size of the polaron, the decrease in α from 4.5 to 1 indicates that in the superconducting phase the free polaron size increases by a factor of more than four compared to the normal state to enhance the overlap and increase the pairing interaction.

The evidence of multiphonon like processes, as discussed in eq. (32) comes from the transmissivity change observed in ref. [8] for the nonsuperconducting YBCO sample at temperature ranging between 7 K and 296 K. In each case the main peak is followed by a large number of small oscillations in the tail of the relaxation whose amplitude decreases with increasing time as well as with increasing sample temperature. As discussed by Feynman *et al* [18] such oscillations are expected whenever external field supplies an energy quantum equal to the energy $\hbar\omega_0$ of an optical phonon plus the energy of excitation to higher levels of the polaron.

5. Conclusion

We have examined the optical absorption, photoemission and femtosecond absorption spectrum of high temperature oxide superconductors and showed that these can be explained on the basis that the charge carriers are polaronic in nature and are primarily located in the Sr/Ba–O planes.

Acknowledgement

The author is thankful to Prof. S S Jha for some stimulating discussions during the preparation of the paper.

References

[1] C M Varma *et al, Phys. Rev. Lett.* **63**, 1996 (1989)
[2] Geo-meng Zhao *et al, Nature (London)* **385**, 386 (1997)
[3] Z-X Shen and J R Schrieffer, *Phys. Rev. Lett.* **78**, 1771 (1997)
[4] J R Schrieffer *et al, Phys. Rev. Lett.* **60**, 945 (1988)
[5] C M Srivastava, *Physica* **C176**, 481 (1991)
[6] J C Campuzano *et al, Phys. Rev. Lett.* **64**, 2308 (1990)
[7] D S Marshall *et al, Phys. Rev. Lett.* **76**, 4841 (1996)
[8] J M Chwalek *et al, Appl. Phys. Lett.* **57**, 1696 (1990)
[9] G L Eeseley *et al, Phys. Rev. Lett.* **27**, 3445 (1990)
[10] J Ranninger, *Solid. State Commun.* **85**, 929 (1993)
[11] G Srinivasan and C M Srivastava, *Phys. Status Solidi* **B103**, 665 (1981)
[12] E Kartheuser, in *Polarons in Ionic Crystal and Polar Semiconductor* edited by J T Devreese (North-Holland, Amsterdam, 1972) pp. 515–550
[13] H G Reik, in *Polarons in Ionic Crystal and Polar Semiconductor* edited by J T Devreese

[15] M Cardona, in *International Conference on Superconductivity*, January 10–14 1990, Bangalore, India edited by S K Joshi, C N R Rao and S V Subramanyam (World Scientific, 1990) pp. 208–223.

[16] M F Crommie and A Zettl, *Phys. Rev.* **B41**, 10978 (1990)

[17] N F Mott, in *Polaron and bipolarons in high-T_c superconductors and related materials* edited by E K H Salje, A-S Alexandor and W Y Liang (Cambridge University Press, 1995) p. 1

[18] R P Feynman *et al, Phys. Rev.* **127**, 1004 (1962)

lectrical properties of a-antimony selenide

ANJEEV GAUTAM, D K SHUKLA, SHELLY JAIN and N GOYAL
entre of Advanced Study in Physics, Panjab University, Chandigarh 160 014, India

S received 7 March 1997; revised 20 October 1997

bstract. This paper reports conduction mechanism in a-Sb_2Se_3 over a wide range of mperature (238 to 338 K) and frequency (5 Hz to 100 kHz). The d.c. conductivity measured as function of temperature shows semiconducting behaviour with activation energy $\Delta E = 0.42$ eV. hermally induced changes in the electrical and dielectric properties of a-Sb_2Se_3 have been xamined. The a.c. conductivity in the material has been explained using modified CBH model. The nd conduction and single polaron hopping is dominant above room temperature. However, in the wer temperature range the bipolaron hopping dominates.

eywords. Chalcogenide glasses; amorphous semiconductors; a.c. conductivity; electrical operties.

ACS Nos 72.20; 71.55

Introduction

uring the last few years amorphous semiconductors have been used in the manufacture f solar cells, batteries and phototransistors as well as in some steps of technological rocessing of very large scale integration (VLSI) microelectronics circuits [1]. Thermally duced structural and electrical effects are known to be important in inducing the emory phenomenon in semiconducting chalcogenide glasses [2–6]. Alzewel *et al* [7, 8] ave studied the electrical conductivity of powdered antimony chalcogenides. Antimony loys have recieved great attention in the past due to semiconductivity of Sb oncentration. It was reported by Mott and Devis [9] that the effect of Sb in Se is ven greater than in Te in promoting crystallization. Recently, study has been made on in and thick films of the system $Bi_{10}Sb_xSe_{90-x}$ ($x = 35$, 40 and 45) [10]. Crystalline b_2Se_3 has been prepared and studied by several workers [11, 12]. Antimony triselenide and gap ~1.2 eV), [13] a p-type semiconductor having an orthorhombic D_8^5 structure ith unit cell dimensions $a = 11.77 \pm 1$, $b = 3.962 \pm 7$ and $c = 11.62 \pm 1$ Å [14] is used the preparation of recording optical laser disc and as an insulating material in MIS olar cells. The preparation and study of amorphous-Sb_2Se_3 can throw light on the ossible applications of this material in that form. Measurements of electrical properties f a-Sb_2Se_3 are reported in this paper over a wide temperature and frequency nge. Results indicate that electrical properties can be explained on the basis of idely accepted modified-correlated barrier hopping (m-CBH) model for chalcogenide asses.

2. Experimental details

Ingots of glassy material Sb_2Se_3 were prepared by melt quench method. The 99.99% pure elements were sealed in an evacuated (1×10^{-6} torr) quartz ampoule (12 mm diameter and 160 mm long). The ampoule was heated in a muffle furnace at the reaction temperature (630 ± 3°C for 24 h). The composition (Sb : Se : 1 : 1) of the glasses was determined by EDAX and amorphous nature was verified by X-ray diffraction pattern obtained using X-ray diffractometer (Philips PW 1130/60). The pellets of 0.677 cm diameter were prepared in the hydraulic press at a pressure of $\approx 10^7$ Pa.

The measurements were carried out in a specially designed vacuum cell in the temperature range 233 to 313 K and frequencies from 6 Hz to 100 kHz. A sophisticated computer controlled ac-impedance system (Model 5206, EG & G, PARC USA) was used for the measurements [17]. Polished samples with a thickness 0.04–0.10 cm and area $0.36\,\text{cm}^2$ were put in contact with aquadag (a conducting emulsion) in a sandwich configuration. The sample was kept in vacuum in a copper sample holder ensuring no temperature gradient between the electrodes and the sample. The effect of temperature is studied using a closed cycle refrigerator (Model F-70, Julabo) to obtain different temperatures, which can maintain constant temperature within ± 1 K for all the measurements. Ohmic contacts were confirmed through linear I-V characterstics in the voltage range. All electrical measurements of real and imaginary components of impedance parameters (Z' and Z'') and real and imaginary component of admittance parameters (Y' and Y'') were made over a wide range of temperature (233 to 313 K) and frequency (6 Hz to 100 kHz).

3. Results and discussion

3.1 *Dipolar behaviour of Sb_2Se_3*

Figure 1 shows the plot of $\ln \sigma_{\text{dc}}$ versus $1000/T$ which was obtained using the expression

$$\sigma_{\text{dc}} = C' \exp(-\Delta E/kT). \tag{1}$$

The plots in figure 1 are found to be linear over the temperature range studied. In the above expression $C' = \sigma_0 \exp(\gamma/k)$ and γ is the temperature coefficient of the band gap. From the figure, the activation energy ΔE and C' for the sample are found to be 0.43 eV and $3.35 \times 10^{-4} \Omega^{-1}\,\text{cm}^{-1}$ respectively. It has also been observed that ΔE is constant for different pellets (thickness = 0.04 cm to 0.08 cm) with a statistical error of 0.3%.

The variation of $\log |Z|$ versus $\log f$ (figure 2) indicates that the impedance is sensitive to frequency at lower temperatures and gradually becomes independent of frequency with increase in temperature. This type of behaviour indicates dominance of band conduction at higher temperatures.

The sensitivity of Sb_2Se_3 to temperature is shown in figure 3. The figure gives the Nyquist plots (Z' versus Z'') for Sb_2Se_3 at different temperatures over the frequency

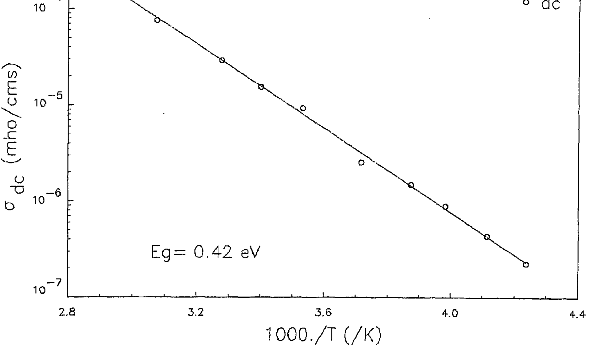

Figure 1. Variation of $\sigma_{dc}(\Omega^{-1}\,cm^{-1})$ with respect to $1000/T$(/K).

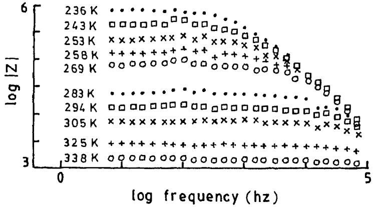

Figure 2. Frequency dependence of log $|Z|(\Omega)$ over the entire temperature range studied.

reduces with rise in temperature and regain their original size when temperature is increased.

The Nyquist plots for Sb_2Se_3 form a perfect arc of a semicircle with its centre lying considerably below the abscissa (i.e., distribution parameter $\alpha \gg 0$). Figure 3 also gives the value of α calculated at different temperatures. In dielectric materials, the finite value of the distribution parameter α and a depressed arc are typical for a dipolar system involving multirelaxation processes [15–17]. But the dependence of α on temperature indicates that the mean position of the dipole is varying with variation in temperature. The dipolar nature of Sb_2Se_3 is further confirmed by investigating the variation of capacitance with temperature at different frequencies. It is clear from figure 4 that in the lower temperature range the value of C is nearly constant and it increases with increase in

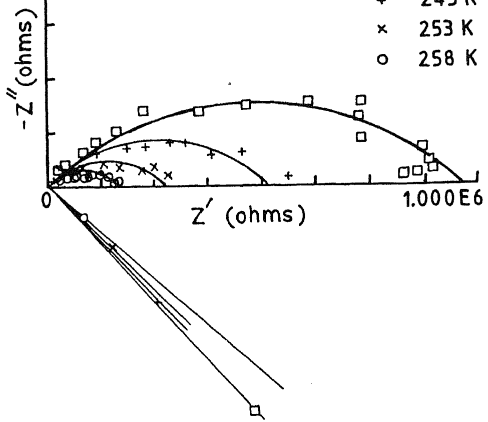

Figure 3. Nyquist plots (Z' versus Z'') at different temperatures. Variation of angle $\alpha = (1 - s)\pi/2$ with respect to temperature.

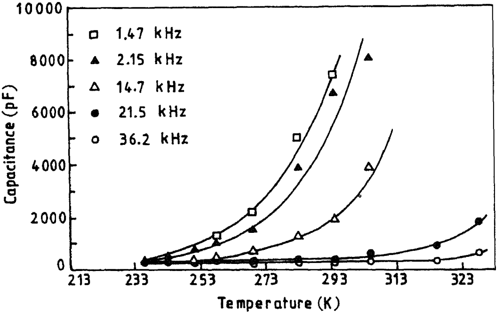

Figure 4. Temperature variation of capacitance at different frequencies.

temperature. However the rate of change of capacitance (i.e., $\mathrm{d}C/\mathrm{d}T$) is higher for lower frequencies and decreases with increasing temperature. These results can be explained by the fact that thermally assisted hopping results in increasing the capacitance of the

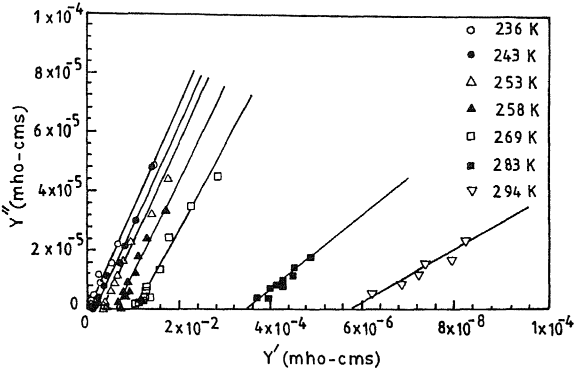

Figure 5. Admittance plots $Y'(\Omega^{-1})$ versus $Y''(\Omega^{-1})$. The variation of angle $\alpha = s\pi/2$ with temperature.

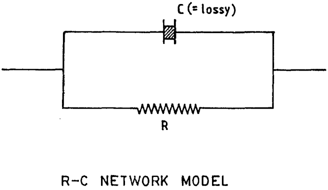

Figure 6. R-C network model for lossy capacitance.

material. In other words, in the lower temperature range, the dipoles remain frozen and attain rotational freedom when the temperature is increased. Thus the relaxation effects are confirmed by the rate of increase in capacitance with frequency.

The inversion of Nyquist plots in the admittance plane are shown in figure 5. It is clear from the figure that the angle of inclination is less than $\pi/2$. This type of behaviour has been explained on the basis of R-C network model (figure 6), such that total impedance is given by [18]

$$\begin{aligned} Y(\omega) &= B(i\omega)^n + i\omega C_\alpha + G_0 \\ &= G_0 + B\{\cos(s\pi/2) + i\sin(s\pi/2)\}\omega^n + i\omega C_\alpha. \end{aligned} \tag{2}$$

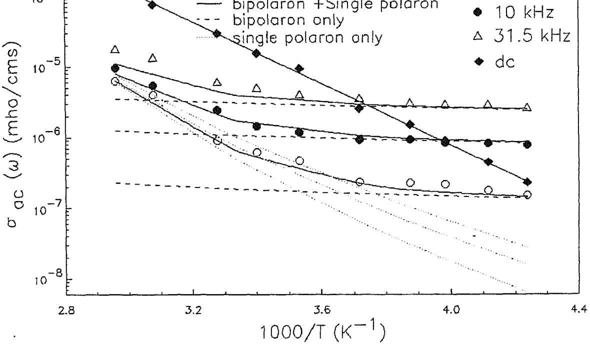

Figure 7. CBH fitting – the variation of $\sigma_{\text{ac}}(\Omega^{-1}\,\text{cm}^{-1})$ with respect to $1000/T$ for experimental points and theoretical curves (m-CBH) at different frequencies.

3.2 *CBH model for a-Sb_2Se_3*

The complex impedance plots show the dipolar multi-relaxation nature of a-Sb_2Se_3. This behaviour is explained by the R-C network model (figure 6). However, this does not further elucidate the nature of conduction mechanism in this sample. Therefore a.c. conductivity $\sigma_{\text{ac}}(\omega)$ at different temperatures is calculated. It is found that dispersion in the temperature dependence of $\sigma_{\text{ac}}(\omega)$ curves increases at lower frequencies while it merges at higher frequencies (figure 7).

From the expression

$$\sigma_{\text{ac}}(\omega) = \sigma_{\text{total}}(\omega) - \sigma_{\text{dc}}, \tag{3}$$

the a.c. conductivity is obtained, where σ_{dc} is given by (1) and its behaviour is shown in figure 1. The $\sigma_{\text{total}}(\omega)$ is measured directly from lock-in-analyser (§ 2). The $\sigma_{\text{ac}}(\omega)$ dominates over σ_{dc} at lower temperatures, while σ_{dc} dominates at higher temperatures (figure 7).

The modified correlated barrier hopping (m-CBH) model explains the experimental results reported in this paper. It states that bipolaron hopping between the charged defects states D^+ and D^- is responsible for the a.c. conductivity in these semiconductors. Dipolar multi-relaxation behaviour of this sample is already indicated from the Nyquist plots described earlier. So the charged defect states are expected to be present in a-Sb_2Se_3. According to CBH model a.c. conductivity is given by [19, 20]

$$\sigma_{\text{ac}} = \frac{n\pi^2 N N_P \epsilon' \omega R_\omega^6}{24}, \tag{4}$$

where n is the number of polarons involved in the hopping process, NN_P is proportional to the square of the concentration of the states and ϵ' is the dielectric constant. R_ω is the hopping distance for the conduction $\omega\tau = 1$ and is given as

$$R_\omega = \frac{4ne^2}{\epsilon'[W_\mathrm{m} - kT\ln(1/\omega\tau_0)]}, \tag{5}$$

where W_m is the maximum barrier height and τ_0 is the characteristic relaxation time for the material.

Figure 7 shows the variation of a.c. conductivity with temperature at different frequencies. It is evident from the figure that σ_ac is very sensitive to temperature in the higher temperature regime. The low temperature a.c. conduction can be explained by considering bipolaron hopping between D^+ and D^- centers whereas the higher temperature behaviour is due to thermally activated single polaron hopping. At higher temperatures a number of thermally generated D^0 centers are produced with a temperature dependent concentration [21]

$$N_0 = N_T \exp(-U_\mathrm{eff}/2kT), \tag{6}$$

where N_T is the concentration of D^+ or D^- centers at $T = 0\,\mathrm{K}$. The defect concentration factor NN_P in (4) is replaced by

$$\begin{aligned} NN_P &= N_T^2/2 && \text{(for bipolaron hopping)},\\ NN_P &= N_T^2/2\exp(-U_\mathrm{eff}/2kT) && \text{(for single polaron hopping)}. \end{aligned} \tag{7}$$

Thus for single bipolaron hopping this factor is thermally activated and hence $\sigma_\mathrm{ac}(\omega)$ is also activated.

According to CBH model [22]

$$B = W_\mathrm{m} - W_1 + W_2, \tag{8}$$

where B is the optical band gap, W_m is the maximum band width and behaviour with frequency ω is as

$$\sigma_\mathrm{ac}(\omega) = A\omega^s. \tag{9}$$

Here [19],

$$s = \frac{\mathrm{d}(\ln\sigma_\mathrm{ac})}{\mathrm{d}\ln\omega} = 1 - 6kT/W, \tag{10}$$

while $W = W_\mathrm{m}$ for bipolaron hopping and $W = W_1$ or W_2 for single polaron hopping. Therefore, W_m is estimated from the s values at lower temperatures. Values of W_1, W_2 and U_eff were estimated from the values of s at higher temperatures. These parameters are then fed to CBH model to fit the a.c. conductivity data calculated from the experiments. The behaviour of (10) ($s = 1 - 6kT/W^*$) can be seen in figure 8. This indicates that W^* follows W_m for lower temperatures and W_2 for higher temperatures. Figure 8 also shows a sudden change in conduction mechanism at a certain temperature (276–278 K). Similar behaviour is noticed in the admittance plots (figure 5). The different parameters used for

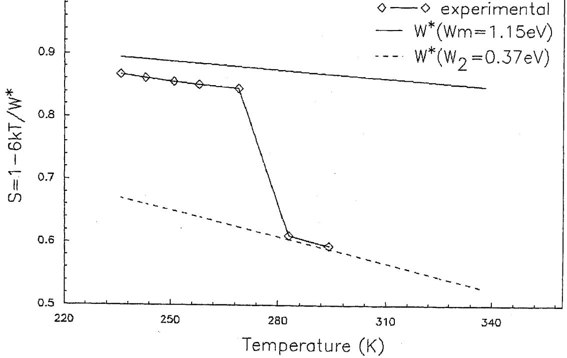

Figure 8. Temperature dependence of $s(= 1 - 6kT/W^{*})$ for theoretical curves (m-CBH) and experimental points.

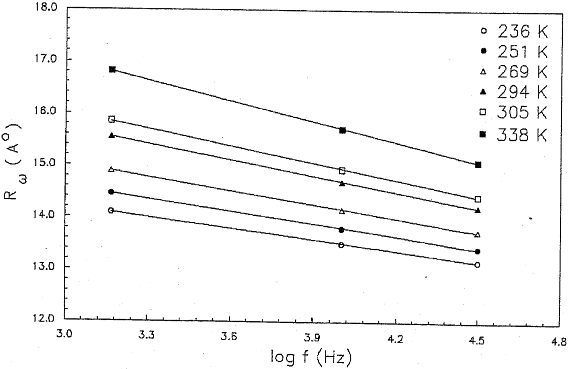

Figure 9. Variation of R_{ω}(Å) with respect to temperature (K) at different frequencies.

Further, the effect of temperature and frequency on the hopping length R_{ω}, which is a measure of the effective length of a dipole can be studied using CBH model. The variation of R_{ω} with frequency at different temperature is shown in figure 9. The figure indicates that R_ω is more sensitive to frequency in the high temperature regime and the sensitivity decreases with decreasing temperature. Thus at low temperature, R_ω is constant with frequency, which implies a constant value of capacitance which is found to be true from figure 4.

4. Conclusion

Nyquist plots or complex impedance studies confirm the dipolar nature of Sb_2Se_3 and multi-relaxation behaviour as seen in most chalcogenide glasses. These plots also indicate that the capacitive nature dominates over the resistive nature of the sample at lower temperature (< 273 K), while the resistive nature is dominant at higher temperatures. The conduction mechanism has a sudden change from bipolaron to single polaron hopping (276–278 K). The temperature and frequency dependence of a.c. conductivity is well explained by the m-CBH model. The contribution to a.c. conductivity from single polaron hopping is dominant at higher temperatures.

Acknowledgements

The authors are grateful to the University Grant Commission for providing funds under COSIST and CAS programmes for purchase of measurement system which was essential for investigations reported in this paper.

References

[1] A C Adams, in *Plasma deposited thin films* edited by J Mort and F Jansen (CRC, Boca Raton, 1986)
[2] A D Pearson, *J. Non-Cryst. Solids* **2**, 1 (1970)
[3] D L Eaton, *J. Am. Ceram. Soc.* **477**, 554 (1964)
[4] H J Stocker, *Appl. Phys. Lett.* **15**, 55 (1969)
[5] B G Bagley and H E Bar, *J. Non-Cryst. Solids* **2**, 155 (1970)
[6] H Fritzsche and S R Ovshinsky, *J. Non-Cryst. Solids* **2**, 148 (1970)
[7] K Alzewl, M M Sekkina and Z M Hanafi, *Z. Phys. Chem.* **94**, 235 (1975)
[8] K Alzewl, M M Sekkina and Z M Hanafi, *Egypt J. Phys.* **12**, 51 (1981)
[9] Mott N F and Davis E A, in *Electronic processes in Noncrystalline materials* (Clarendon, Oxford, 1971) p. 371
[10] M Fadel, K M Sharaf and N A Hegab, *Indian J. Pure Appl. Phys.* **34**, 810–814 (1996)
[11] B R Chakraborty, B Ray, R Bhattacharya and A K Dutta, *J. Phys. Chem. Solids* **41**, 913 (1980)
[12] F Kosek, J Tulka and L Stourac, *Czech. J. Phys.* **B28**, 325 (1978)
[13] C Wood, Z Hurych and J C Shaffer, *J. Non-Cryst. Solids* 209 (1972)
[14] W E Pearson, in *Handbook of lattice spacing and crystal structure of metals* (Pergamon Press, New York, 1964) p. 843
[15] A Vohra and K K Srivastva, *Philos. Mag.* **61**, 201 (1990)
[16] R Shukla, P Khurana and K K Srivastva, *J. Mater. Sci. Mat. Electr.* **3**, 132 (1992)
[17] Navdeep Goyal, *Pramana – J. Phys.* **40**, 97 (1993)
[18] A K Jonscher, in *Dielectric relaxation in solids* (Chelsea Dielectric Press, London, 1983) p. 90
[19] S R Elliott, *Philos. Mag.* **36**, 1291 (1977)
[20] S R Elliott, *Philos. Mag.* **B36**, 135 (1977)

Monte-Carlo optimization of correlated helium wave function

SABYASACHI KAR and PUSPAJIT MANDAL
Department of Mathematics, Visva-Bharati University, Santiniketan 731 235, India
E-mail: pmandal@vbharat.ernet.in

MS received 15 January 1997; revised 8 December 1997

Abstract. A new type of correlated wave function for the normal helium is proposed in the form: $\Psi(\mathbf{r}_1,\mathbf{r}_2)=\sum c_m\Phi_m$ with $\Phi_m=\exp[-\alpha(r_1+r_2)]/(br_{12}+a)^m$ where a,b,α are non-linear variational parameters. Optimizing these parameters by the Monte-Carlo technique, an energy eigenvalue of -2.903645(a.u.) is obtained with *only three* terms in the basis expansion alongwith satisfactory cusp condition, compared to the essentially exact non-relativistic value of -2.903724 as given by Freund *et al* (*Phys. Rev.* **A29**, 980 (1984)).

Keywords. Eigenenergy; normal state; Virial theorem; Monte-Carlo optimization.

PACS Nos 02.60; 02.70; 03.65; 31.20

1. Introduction

Since the early days of quantum mechanics the study of electron–electron correlation in atomic and molecular physics has been in the lime light for its vital importance and significance in determining the behaviour of the bound electrons. A large number of important contributions [1–7] has been made on two-electron atomic systems during the last six decades. Of these, Pekeris [5] made an outstanding contribution in which he predicted essentially exact eigenvalues and other parameters for the ground and first few excited states of two-electron atomic systems using the Raleigh–Ritz upper-bound and Rubinow lower-bound methods. When the number of electrons become higher in an atom or a molecule, electron–electron correlation is taken into account by the many-body perturbation theory (MBPT), the configuration interaction (CI) method, the multi-configuration self-consistent field (MCSCF) theory, etc [8–10]. In all these methods, the calculations and the related computations become enormously difficult and complex.

Recently some significant results have been reported in the literature on the two-electron atomic ground and higher excited states [11–13]. Umrigar *et al* [11] used Monte-Carlo multi-configuration self-consistent field theory with several hundred parameters in the basis set to consider electron–electron correlation in the normal H$^-$, He, Be and few of their excited states. On systematically improving the wave function they were able to obtain accurate results in accord with Pekeris [5] and Freund *et al* [16]. Bhattacharyya *et al* [12], on the other hand, used a very simple three-parameter correlated wave function of the form:

$$\Psi(\mathbf{r}_1, \mathbf{r}_2) = \exp[-\alpha(r_1 + r_2)][1 - \lambda \exp(-\mu r_{12})] \tag{1}$$

and obtained an analytic expression for the energy eigenvalue of the normal helium: $\epsilon = \langle\Psi|H|\Psi\rangle/\langle\Psi|\Psi\rangle$. They reported a value of -2.8894 (a.u.) (-78.6253 eV) which is much improved over the corresponding Hartree–Fock (HF) result, -2.86168(a.u.) (-77.87104 eV), for the following parameters : $\alpha = 1.8395$, $\lambda = 0.586$, $\mu = 0.379$. They obtained a value, 0.5365, for the correlation cusp condition, $((1/\Psi)(\partial\Psi/\partial r_{12}))_{r_{12}\to 0}$, as compared to the exact value, 0.5. Regarding an over estimation of the cusp condition by about 6%, it is possible that proper optimization of the parameters might reflect on its actual value corresponding to this wave function. Very recently, Drake [13] performed an elaborate calculation with the inclusion of non-relativistic and relativistic effects and used a huge basis set to report very accurate results correct up to 9 to 11 significant figures.

In this paper , we propose a very simple form of the correlated wave function for the ground state of the helium atom in the form

$$\Psi(\mathbf{r}_1, \mathbf{r}_2) = \sum c_m \Phi_m \tag{2}$$

with

$$\Phi_m = \exp[-\alpha(r_1 + r_2)]/(br_{12} + a)^m, \tag{3}$$

where c_m's are the linear expansion coefficients ($m = 1, 2, \ldots, N$) and α, a, b are non-linear variational parameters. We use the Raleigh–Ritz variational method and exploit its upper-bound principle to obtain our results. The non-linear variational parameters are optimized by using the Monte-Carlo technique.

The plan of the paper is as follows. We give a brief account of the theory in § 2 and discuss the numerical method in § 3. The results are discussed in § 4. Atomic units (a.u.) are used in our calculations in which $a_0 = m_0 = e = \hbar = 1$, 1 a.u. of energy ($= e^2/a_0$) = 27.21165 eV.

2. Theory

The standard eigenvalue equation according to the Raleigh–Ritz variational principle for the determination of the correlated orbitals $\Phi_m(\mathbf{r}_1, \mathbf{r}_2)$ takes the form

$$\underline{H}\,\underline{c} = \epsilon \underline{S}\,\underline{c}, \tag{4}$$

where the Hamiltonian matrix $\underline{H}$ and the overlap matrix $\underline{S}$ have the elements H_{nm}, S_{nm} respectively over the functional space of the electron co-ordinates $\mathbf{r}_1, \mathbf{r}_2$ ($m, n = 1, 2, \ldots, N$), the vector $\underline{c}^t = (c_1, c_2, \ldots, c_n)$ and ϵ, the required energy eigenvalue.

In order to evaluate the matrix elements H_{nm} and S_{nm}, use is made of the Fourier integral transformation for functions of the type $\exp(-\lambda r)/r$ in the form

$$\frac{\mathrm{e}^{-\lambda r}}{r} = \frac{1}{2\pi^2}\int \frac{\mathrm{e}^{i\mathbf{p}\cdot\mathbf{r}}}{p^2 + \lambda^2}\mathbf{dp}, \quad (\lambda \geq 0) \tag{5}$$

and the Laplace integral transform for function $(br_{12} + a)^{-m}$ in the form:

where $\Gamma(m)$ denotes the gamma function, $\Gamma(m+1) = m\Gamma(m), \Gamma(1) = 1$. Final expressions involve only a single-dimensional integral over $[0, \infty)$ which is evaluated numerically using 20 Gauss–Legendre quadrature points. Typically, the overlap matrix elements S_{nm} are obtained as

$$\begin{aligned} S_{nm} &= \langle \Phi_n | \Phi_m \rangle \\ &= \frac{1}{\Gamma(m+n)} \int_0^\infty \mathrm{e}^{-at} t^{m+n-1} f(t) \mathrm{d}t \end{aligned} \tag{7}$$

with

$$f(t) = 64\pi^2 \frac{(\beta+\mu_t)^3 + \gamma(\beta+\mu_t)[2(\beta+\mu_t)+(\gamma+\mu_t)+(\beta+\gamma)] + \gamma(\gamma+\mu_t)(\beta+\gamma)}{(\beta+\mu_t)^3(\gamma+\mu_t)^3(\beta+\gamma)^3}.$$

3. Numerical evaluation and Monte-Carlo optimization

We have solved the eigenvalue equation (4) by first premultiplying it with an inverse of the matrix $\underline{S}$ and then finding the characteristic polynomial corresponding to the matrix $\underline{S}^{-1}\underline{H} = \underline{A}$, say. The solutions of this polynomial constitute the required eigenvalue spectrum, the least of which gives the desired eigenenergy. For this we require a range of values for the non-linear variational parameters a, b, α, which is accomplished with the Monte-Carlo optimization technique.

3.1 *Krylov's algorithm*

In order to obtain the characteristic polynomial in ϵ, we have used the Krylov algorithm for expanding the secular determinant, $\det(\epsilon \underline{I} - \underline{A})$ [14]. Let

$$\det(\epsilon \underline{I} - \underline{A}) = \epsilon^n + p_1 \epsilon^{n-1} + \cdots + p_{n-1}\epsilon + p_n \tag{8}$$

be the characteristic polynomial. By using now the Cayley–Hamilton theorem which states that, the matrix $\underline{A}$ reduces its characteristic polynomial to zero, we obtain

$$\underline{A}^n + p_1 \underline{A}^{n-1} + \cdots + p_{n-1}\underline{A} + p_n \underline{I} = \underline{0}. \tag{9}$$

Let us consider an arbitrary non-null vector:

$$\underline{y}^{(0)} = \begin{pmatrix} y_1^{(0)} \\ y_2^{(0)} \\ \vdots \\ y_n^{(0)} \end{pmatrix}. \tag{10}$$

Postmultiplying both sides of equation (9) by $\underline{y}^{(0)}$, we get

$$\underline{A}^n \underline{y}^{(0)} + p_1 \underline{A}^{n-1} \underline{y}^{(0)} + \cdots + p_{n-1} \underline{A} \underline{y}^{(0)} + p_n \underline{y}^{(0)} = 0 \tag{11}$$

$$\underline{y}^{(n)} + p_1 \underline{y}^{(n-1)} + \cdots + p_{n-1} \underline{y}^{(1)} + p_n \underline{y}^{(0)} = \underline{0} \qquad (13)$$

which takes the form

$$\begin{pmatrix} y_1^{n-1} & y_1^{n-2} & \cdots & y_1^0 \\ y_2^{n-1} & y_2^{n-2} & \cdots & y_2^0 \\ \cdots & \cdots & \cdots & \cdots \\ y_n^{n-1} & y_n^{n-2} & \cdots & y_n^0 \end{pmatrix} \begin{pmatrix} p_1 \\ p_2 \\ \vdots \\ p_n \end{pmatrix} \begin{pmatrix} y_1^{(n)} \\ y_2^{(n)} \\ \vdots \\ y_n^{(n)} \end{pmatrix}, \qquad (14)$$

where

$$\underline{y}^{(k)} = \begin{pmatrix} y_1^{(k)} \\ y_2^{(k)} \\ \vdots \\ y_n^{(k)} \end{pmatrix}, \quad k = 0, 1, 2, \ldots, n. \qquad (15)$$

Since on the basis of the formula (12) $\underline{y}^{(k)} = \underline{A}\underline{y}^{k-1}, (k = 1, 2, \ldots, n)$, the coordinates $y_1^{(k)}, y_2^{(k)}, \ldots, y_n^{(k)}$ of the vector $\underline{y}^{(k)}$ are successively computed from the relation

$$\begin{aligned} y_i^{(1)} &= \sum_{j=1}^{n} a_{ij} y_j^{(0)} \\ y_i^{(2)} &= \sum_{j=1}^{n} a_{ij} y_j^{(1)} \\ &\cdots \quad \cdots \quad \cdots \quad \cdots \\ y_i^{(n)} &= \sum_{j=1}^{n} a_{ij} y_j^{(n-1)}, \quad i = 1, 2, \ldots, n. \end{aligned} \qquad (16)$$

These are the input elements for the coefficient matrix in the system of linear equations (14) for the determination of the coefficients $p_1, p_2, \ldots, p_n$ of the polynomial (8). It is to be noted that the coordinates of the initial vector $\underline{y}^{(0)}$ of eq. (10) are arbitrary. If the system of equations has a unique solution, then the roots $p_1, p_2, \ldots, p_n$ are the coefficients of the characteristic polynomial (8). If the system (14) does not have a unique solution, the problem gets complicated and a new initial vector is to be tried. In our calculations, we have used the unit vector $(1, 0, \ldots, 0)^t$ as the starting solution. We have solved the linear system of equations (14) by using the scheme of Khaletsky [14]. The roots of the characteristic polynomial is next determined by using the Newton–Raphson method for a set of values of the non-linear variational parameters a, b, α.

3.2 *Monte-Carlo optimization*

Optimization of the non-linear variational parameters by the Monte-Carlo technique is another noteworthy point of our calculation which helps determine the energy eigenvalue with greater ease. Though use of this technique may have been made in bound-state

state problems. We generate random numbers within a prescribed range of values for each of these variational parameters. Our philosophy of optimization of the non-linear variational parameters has been a departure from the conventional approach. We do not increase the number of basis terms in the wave function for a pre-determined set of values of these non-linear variational parameters. Instead, we first decide on the number of terms that are to be retained in a particular calculation. This is done with a view to fully utilize the potential of the wave function with the help of the Monte-Carlo technique. The non-linear variational parameters a, b, α are changed in a random manner within their prescribed ranges of variation one after the other, until the best energy is obtained by utilizing the upper-bound principle of the Raleigh–Ritz method.

In order to check this procedure, we have also studied the following wave functions:

$$\Psi(\mathbf{r}_1, \mathbf{r}_2) = c_1 \exp[-(Ar_1 + Br_2)] + c_2(1 \leftrightarrow 2), \tag{17}$$

$$\Psi(\mathbf{r}_1, \mathbf{r}_2) = N \exp[-\alpha(r_1 + r_2)][c_1 + c_2 \exp(-\mu r_{12})]. \tag{18}$$

The wave function (17) is known after Eckart [15] and incorporates radial correlation through the exchange symmetry. Results of the optimized parameters and the eigenenergy are listed below alongwith other values available in the literature.

4. Results and discussion

The present results are listed in tables 1, 2 and 3, alongwith the accurate values of Pekeris [5], and Roothaan and Weiss [6]. It is a noteworthy feature of our wave function that reliable results are obtained with only three terms in the basis expansion (2). The reason for such a finding is believed to be the inclusion of electron–electron correlation through higher orders by considering terms of the form $1/(br_{12} + a)^m$ in the basis wave function.

Furthermore, the basis functions $\Phi_m(\mathbf{r}_1, \mathbf{r}_2)$ of eq. (3) remain finite at the origin as r_1, r_2, r_{12} all tend to zero. As is further desired, these correlated orbitals also vanish far away from the origin, when both $r_1, r_2 \to \infty$, r_{12} remaining finite or becoming very large. As the bound-systems consisting of the atomic or molecular particles is confined in a finite volume in space, there arises no possibility of allowing $r_{12} \to \infty$ without making $r_1, r_2 \to \infty$ at the same time, which would any way make $\Phi_m(\mathbf{r}_1, \mathbf{r}_2) \to 0$ in the limit. Thus our choice of the correlated basis functions (3) seems to be rested on meaningful physical consideration.

As mentioned earlier, we have also studied the same problem with different forms of the wave function as given by eqs (17) and (18). The Eckart wave function (17) yields a better value -2.875661(a.u.) for helium atom than the HF result -2.86168 (a.u.), while the present wave function (18) gives an eigenenergy -2.891124(a.u.). As mentioned earlier, the Eckart wave function (17) represents a fair amount of correlation due to exchange symmetry. It is apparent from the values of the screening constants A and B that while one electron is assumed to be close to the nucleus, the other electron remains far away from it. Such a wave function which incorporates an additional flexibility for the electrons to avoid each other is often called *a split-shell wave function*.

Table 1. Eigenenergies (a.u.), the non-linear variational parameters and the expansion coefficients for correlated wave functions alongwith cusp conditions.

Form of the wave function ($Z = 2$)	ϵ (a.u.)	Parameters	$((1/\Psi)(\partial\Psi/\partial r_{12}))_{r_{12}\to 0}$ = 0.5 (Exact)
1. Wave function (17):			
(a) Our work	−2.875661	$A = 1.188$, $B = 2.184$ $c_1 = 1.0026$, $c_2 = 2.0053$	–
(b) Pauling and Wilson (1935)	−2.8754	$A = 2.15$, $B = 1.19$	–
2. Wave function (18):			
(a) Our work	−2.891124	$\alpha = 1.848$, $\mu = 0.01902$, $c_1 = 1.0$, $c_2 = -0.9513$, $N = 89.388$	0.372
(b) Roothan and Weiss (1960)	−2.89115	$\alpha = 1.8395$	0.379
(c) Bhattacharyya *et al* (1996)	−2.8894	$\alpha = 1.8395$, $\mu = 0.379$ $c_1 = 1.0$, $c_2 = -0.586$	0.5356
3. Wavefunction (2):			
(a) $m = 2$	−2.891566	$\alpha = 1.855$, $a = 1.255$, $b = 0.0001$, $c_1 = 9644.931$, $c_2 = -12101.823$	0.376
(b) $m = 3$	−2.903645	$\alpha = 1.845$, $a = 1.935$, $b = 0.01$, $c_1 = 150.838$, $c_2 = -132.873$, $c_3 = -298.482$	0.475
4. 'Exact' results:	(see text)		
(a) Pekeris (1962)	−2.903724375	1078 terms	–
(b) Roothan and Weiss (1960)	−2.90039 (closed shell)	64 terms	0.465
(c) Freund *et al* (1984)	−2.903724	–	–

That the optimization procedure is numerically stable is demonstrated in tables 2 and 3, where we enlist the values of the eigenenergy for a number of non-linear variational parameters near the respective best value corresponding to the wave functions (17), (18) and (2) alongwith the averages for the nuclear and Coulomb interactions $\langle 1/r_1 \rangle$, $\langle 1/r_{12} \rangle$ correct upto sixth decimal place. The computer code is freely available for execution in personal computers using Fortran 77. The steadiness of the optimized values clearly emphasizes the correctness of our Monte-Carlo optimization procedure used in the evaluation.

Further indication of the flexibility of our wave function is obtained by the values of the correlation cusp condition $((1/\Psi)(\partial\Psi/\partial r_{12}))_{r_{12}\to 0}$. Compared to the exact value of 0.5, we have obtained a value, 0.475, which is comparable to the result, 0.465, as reported by Roothaan and Weiss [6]. That the exact result is underestimated by the present wave function is quite natural. As the eigenenergy is symmetrically improved towards the exact value in the non-relativistic limit, the cusp condition is expected to gradually tend to its exact value of 0.5. This is evident from the figures of table 1 for the cusp condition and

$$\Psi = N\exp[-\alpha(r_1 + r_2)](c_1 + c_2\exp[-\mu r_{12}]). \tag{18}$$

Wave function (17):

A	B	$-\epsilon$ (a.u.)	$-\epsilon$ (eV)	$\langle 1/r_1\rangle$	$\langle 1/r_{12}\rangle$	$-\langle$P.E.$\rangle/\langle$K.E.$\rangle$[†]
1.184	2.184	2.875654	78.251293	1.68400	0.990102	2.001885
1.186	2.184	2.875660	78.251456	1.68500	0.991048	2.000824
1.187	2.184	2.875661	78.251483	1.68550	0.991521	2.000293
1.188	2.184	2.875661	78.251483	1.68600	0.991994	1.999762
1.189	2.184	2.875660	78.251456	1.68650	0.992466	1.999231
1.190	2.184	2.875659	78.251429	1.68700	0.992938	1.998700
1.192	2.184	2.875656	78.251429	1.68800	0.993880	1.997638
1.188	2.181	2.875659	78.251429	1.68450	0.991401	2.001644
1.188	2.182	2.875660	78.251456	1.68500	0.991599	2.001016
1.188	2.183	2.875661	78.251483	1.68550	0.991796	2.000389
1.188	2.185	2.875660	78.251456	1.68650	0.992191	1.999135
1.188	2.186	2.875659	78.251429	1.68700	0.992388	1.998509
1.188	2.188	2.875654	78.251293	1.68800	0.992782	1.997257
1.188	2.190	2.875646	78.251075	1.68900	0.993176	1.996006

Wave function (18): $c_1 = 1.0$

α	μ	$-c_2$	$-\epsilon$ (a.u.)	$-\epsilon$ (eV)	$\langle 1/r_1\rangle$	$\langle 1/r_{12}\rangle$	$-\langle$P.E.$\rangle/\langle$K.E.$\rangle$[†]
1.846	0.01902	0.9513	2.891121	78.672175	1.687294	0.973528	2.002286
1.847	0.01902	0.9513	2.891123	78.672230	1.688265	0.974118	2.001144
1.848	0.01902	0.9513	2.891124	78.672257	1.689236	0.974708	2.000004
1.849	0.01902	0.9513	2.891122	78.672202	1.690207	0.975298	1.998865
1.848	0.01800	0.9513	2.891021	78.669454	1.694998	0.981041	1.994185
1.848	0.01900	0.9513	2.891123	78.672230	1.689347	0.974830	1.999892
1.848	0.01901	0.9513	2.891124	78.672257	1.689292	0.974769	1.999948
1.848	0.01903	0.9513	2.891124	78.672257	1.689181	0.974647	2.000059
1.848	0.01904	0.9513	2.891124	78.672257	1.689125	0.974585	2.000115
1.848	0.01905	0.9513	2.891124	78.672257	1.689070	0.974526	2.000171
1.848	0.01906	0.9513	2.891124	78.672257	1.689015	0.974465	2.000226
1.848	0.01910	0.9513	2.891124	78.672257	1.688794	0.974222	2.000448
1.848	0.01920	0.9513	2.891123	78.672230	1.688242	0.973617	2.001002
1.848	0.01930	0.9513	2.891120	78.672148	1.687693	0.973014	2.001553
1.848	0.01902	0.9500	2.891094	78.671440	1.692237	0.977991	1.996976
1.848	0.01902	0.9510	2.891122	78.672202	1.689938	0.975475	1.999297
1.848	0.01902	0.9512	2.891123	78.672230	1.689470	0.974964	1.999768
1.848	0.01902	0.9514	2.891124	78.672257	1.689001	0.974451	2.000240
1.848	0.01902	0.9515	2.891124	78.672257	1.688765	0.974193	2.000478
1.848	0.01902	0.9520	2.891120	78.672148	1.687577	0.972894	2.001672

[†] The Virial theorem states that $-\langle\text{P.E.}\rangle/\langle\text{K.E.}\rangle = 2.0$.

parameters do not seem to be optimized properly, since the eigenenergy as reported by them is much worse than that quoted in Roothaan and Weiss [6] and that obtained by us independently with our procedure in the present calculation.

In summary, the results seem to indicate that a satisfactory calculation can be made with correlated wave functions of the form (3) for studies on a two-electron system. This

α	a	b	$-\epsilon$ (a.u.)	$-\epsilon$ (eV)	$\langle 1/r_1 \rangle$	$\langle 1/r_{12} \rangle$	$-\langle \text{P.E.} \rangle / \langle \text{K.E.} \rangle$†
1.842	1.935	0.010	2.899020	78.887120	1.675589	0.960306	2.019694
1.843	1.935	0.010	2.901747	78.961326	1.688495	0.957650	2.002475
1.844	1.935	0.010	2.902974	78.994715	1.689214	0.954866	2.001365
1.845	1.935	0.010	2.903645	79.012974	1.689876	0.953914	2.000586
1.846	1.935	0.010	2.903592	79.011532	1.689810	0.954052	2.000688
1.847	1.935	0.010	2.903476	79.008375	1.689728	0.954258	2.000792
1.848	1.935	0.010	2.903287	79.003232	1.690132	0.956924	2.001024
1.845	1.932	0.010	2.903436	79.007287	1.689562	0.953726	2.000810
1.845	1.933	0.010	2.903542	79.010171	1.689477	0.952978	2.000743
1.845	1.934	0.010	2.903604	79.011858	1.689899	0.954372	2.000684
1.845	1.936	0.010	2.903574	79.011042	1.690664	0.957542	2.000701
1.845	1.937	0.010	2.903531	79.009872	1.689465	0.954095	2.001137
1.845	1.935	0.008	2.901004	78.941108	1.674465	0.956243	2.020905
1.845	1.935	0.009	2.903264	79.002606	1.689572	0.954263	2.000863
1.845	1.935	0.011	2.902991	78.995178	1.687658	0.973255	2.009952
1.845	1.935	0.012	2.899028	78.887338	1.679356	0.962345	2.015048
1.845	1.935	0.013	2.898904	78.883963	1.677997	0.967128	2.018604
1.845	1.935	0.014	2.897617	78.848942	1.677892	0.977128	2.021430
1.845	1.935	0.020	2.893545	78.738136	1.687954	0.973968	2.003204
1.845	1.935	0.100	2.891501	78.682516	1.688176	0.974300	2.001593

† The Virial theorem states that $-\langle \text{P.E.} \rangle / \langle \text{K.E.} \rangle = 2.0$.

prescription may be an inexpensive alternative to the well-tested correlated wave functions containing Hylleraas coordinates which have produced amazingly accurate results over the years ([2–6, 11]).

5. Conclusion

We have reported our findings with a new type of correlated wave function for the ground state helium atom. The results indicate that this wave function is sufficiently flexible to take into account the effect of electron–electron correlation in atomic systems. This application for a small system for which definitive results are available from the works of Pekeris [5], Drake and co-workers [13] and Freund *et al* [16] shows the simplicity of our approach. Now, neither the use of the form of correlation with inverse powers of r_{12} in the wave function such as eq. (3) is certainly new (see, for instance, Kinoshita [4] or Umrigar *et al* [11]) nor the optimization of the non-linear parameters by Monte-Carlo technique is novel. What we show in this work is that reasonably accurate values of the eigenenergy of the two-electron systems can hopefully be obtained with our prescription with ease and elegance. Such a simple form of the wave function may therefore find applications in other areas, such as, atomic or molecular collisions where bulk of the theoretical efforts are involved with inaccurate bound-state wave functions without taking account of any correlation of the atomic/molecular electrons.

Further, this simple approach can be extended to write molecular wave functions through linear combination of atomic orbitals (LCAO) which would explicitly incorporate electron–electron correlation. Thus this method might be used alongwith other methods in structure calculations, such as, the density functional theory ([17–21]), the CI method, the MCSCF theory, the MBPT, etc.

All these calculations were performed on an IBM-compatible PC/AT of 100 MHz clockspeed with double precision arithmetic. Further applications of this correlated basis function would hopefully make a new beginning in the study of many-body systems in atomic, molecular, nuclear and solid-state physics.

References

[1] G Temple, *Proc R. Soc. (London)* **A119**, 276 (1928)
[2] E A Hylleraas, *Z. Phys.* **54**, 347 (1929); **65**, 209 (1930)
[3] S Chandrasekhar, *Astrophys. J.* **128**, 114 (1958)
[4] T Kinoshita, *Phys. Rev.* **115**, 366 (1959)
[5] C L Pekeris, *Phys. Rev.* **126**, 1470 (1962)
[6] C C J Roothaan and A W Weiss, *Rev. Mod. Phys.* **32**, 194 (1960)
[7] L Pauling and E B Wilson, Jr *Introduction to Quantum Mechanics* (McGraw-Hill Book Company, London, 1935)
[8] O Sinanoglu, *J. Chem. Phys.* **36**, 706 (1962)
[9] K A Brueckner, in *The Many Body Problem* (John Wiley & Sons Inc., New York, 1959)
[10] P-O Löwdin and B Pullman, *Molecular Orbitals in Chemistry, Physics and Biology* (Academic Press, New York, 1964)
[11] C J Umrigar, K G Wilson and J W Wilkins, *Phys. Rev. Lett.* **60**, 1719 (1988)
[12] S Bhattacharyya, A Bhattacharyya, B Thalukdar and N C Deb, *J. Phys.* **B29**, L147 (1996)
[13] T Zhang, Z-C Yan and G W F Drake, *Phys. Rev. Lett.* **77**, 1715 (1996)
G W F Drake and Z-C Yan, *Phys. Rev.* **A46**, 2378 (1992)
[14] B P Demidovich and I A Maron, *Computational Mathematics*, English translation G Yankovsky (Mir : Moscow, 1973), pp. 246, 421
[15] C Eckrat, *Phys. Rev.* **36**, 878 (1930)
[16] D E Freund, B D Huxtable and J D Morgan, *Phys. Rev.* **A29**, 980 (1984)
[17] P Hohenberg and W Kohn, *Phys. Rev.* **136**, B864 (1964)
[18] W Kohn and L J Sham, *Phys. Rev.* **140**, A1133 (1965)
[19] R O Jones and O Gunnarsson, *Rev. Mod. Phys.* **61**, 689 (1989)
[20] F L Pilar, *Elementary Quantum Chemistry*, 2nd edition (McGraw-Hill, New York, 1990)
[21] I N Levine, *Quantum Chemistry*, 4th edition (Prentice-Hall Inc., Eaglewood Cliffs, N.J., USA, 1991)

Total electron scattering cross-sections for nitrous oxide at low electron energies

P RAWAT, K P SUBRAMANIAN and VIJAY KUMAR
Physical Research Laboratory, Navrangpura, Ahmedabad 380 009, India
Email: vkumar@prl.ernet.in

MS received 15 December 1997; revised 13 January 1998

Abstract. Absolute total electron scattering cross sections for nitrous oxide have been measured at low electron energies using a photoelectron source. The measurements have been carried out at 19 electron energies varying from 0.73–9.14 eV with an accuracy of ±3%. The cross sections obtained in the present experiment have been compared with other measurements.

Keywords. Electron scattering; total cross sections; nitrous oxide.

PACS No. 34.80

The scattering of low energy electrons by atoms and molecules has been studied for many years. It has been found to be important for the better understanding of weakly ionized plasma. The electron collision studies of nitrous oxide molecules are of particular importance as N_2O lasers are now being used as a secondary frequency standard in areas of spectroscopy [1]. Also, nitrous oxide plays an important role in stratospheric chemistry and eventually affects the Earth's climate [2].

Total electron scattering cross sections for nitrous oxide were measured many years ago by Brüche [3] at electron energies larger than 1.0 eV and by Ramsauer and Kollath [4] at energies varying from 0.1–1.2 eV. Since then, only three more measurements have been reported using high energy resolution electron spectrometers. Zecca *et al* [5] used a retarding potential difference electron monochromator to obtain normalized total cross sections at electron energies ranging from 0.75–7 eV whereas a linear transmission method was employed by Szmytkowski *et al* [6] to obtain absolute cross section values in the energy range 0.8–40 eV. Absolute total cross sections for 1–500 eV electron scattering of nitrous oxide were also reported by Kwan *et al* [7] by a beam transmission method. However, some relative transmission measurements have been carried out by Boness *et al* [8] and Sanche and Schulz [9] in the energy range 0–6 eV, but unfortunately, it is not possible to obtain cross sections from these results. Also, no theoretical computations have so far been reported in the literature for obtaining the absolute total electron scattering cross sections for nitrous oxide. In a nutshell, there are only four measurements available for a possible comparison of cross section values at electron energies from 0.7–10 eV. Although the general shape of the cross section curves reported by Szmytkowski *et al* [6], Kwan *et al* [7], Zecca *et al* [5] and Brüche [3] is more or less similar with respect to electron energy, the cross section values in some cases are different. There is a large discrepancy in cross section values at and around the well-known ${}^2\sum^+$ shape resonance centered at 2.3 eV energy [10]. Around the peak of the shape resonance, the cross section value reported by Szmytkowski *et al* [6] is about 26% higher than that obtained by Brüche [3] and is larger by a factor of 2.3 than the normalized cross section given by Zecca [5]. However, there is satisfactory agreement in cross section values reported by Kwan *et al* [7] and Szmytkowski *et al* [6] at the peak of the shape resonance. Also, there is a large discrepancy in the results obtained by the four groups on both sides of the shape resonance at energies ranging from 1.5–3.5 eV. In view of this, we decided to measure the absolute total scattering cross sections for nitrous oxide at low electron energies.

This paper is part of the ongoing research programme taken up to measure total electron scattering cross sections for atoms and molecules at low electron energies using a photoelectron source. Previously, absolute total cross sections for helium, neon [11], argon, krypton, xenon [12], molecular hydrogen [13] and molecular oxygen [14] have been measured at electron energies from 0–10 eV. In this paper, we present measurements of scattering cross sections for electrons scattered by nitrous oxide with projectile energy varying from 0.73–9.14 eV.

A detailed description of the experimental set-up used for the study, the method for analysis of the data and error analysis has been reported previously [11, 12]. In brief, the experiment consists of measuring the intensities of the peaks in the photoelectron spectra of the source gas such as argon, krypton, xenon or nitrous oxide itself. The photoelectrons thus produced by the source gas are scattered by the target gas, the cross section of which is to be determined. Each peak in the photoelectron spectrum of the source gas provides one point in the electron energy scale. Complete scanning of the electron energy is performed by varying the energy of the ionizing radiation as well as changing the source gas. Using different combinations of photons of three different wavelengths (HeI, 58.4 nm, NeI, 73.6 nm and 74.4 nm) and four different source gases and neglecting the energy points where the statistics for the photoelectron intensity were poor, it was possible to measure scattering cross sections at 19 electron energies.

The electron scattering cross sections for nitrous oxide were measured using the method described previously. When source and target species are different, the electron scattering cross section σ can be evaluated by using the following equation:

$$\ln\left(\frac{I_{e2}\, I_{\lambda 01}}{I_{e1}\, I_{\lambda 02}}\right) = \frac{P_1 - P_2}{760}\,[n_0\sigma x + k(al_1 + l_2)]. \qquad (1)$$

Here I_{e1} and I_{e2} are the amplitudes of the photoelectron peaks at two different gas pressures P_1 and P_2, $I_{\lambda 01}$ and $I_{\lambda 02}$ are the incident photon intensities monitored during the experiment by the beam monitor at the two pressures, l_1 is the distance from the centre of the beam splitter to the circular aperture covering the ionization region, l_2 is the distance from the same aperture to the actual ionization region defined geometrically by different slits in the acceleration region and cylindrical mirror analyser, x is the scattering path length, a is the ratio of the pressures of the target gas outside and inside the ionization

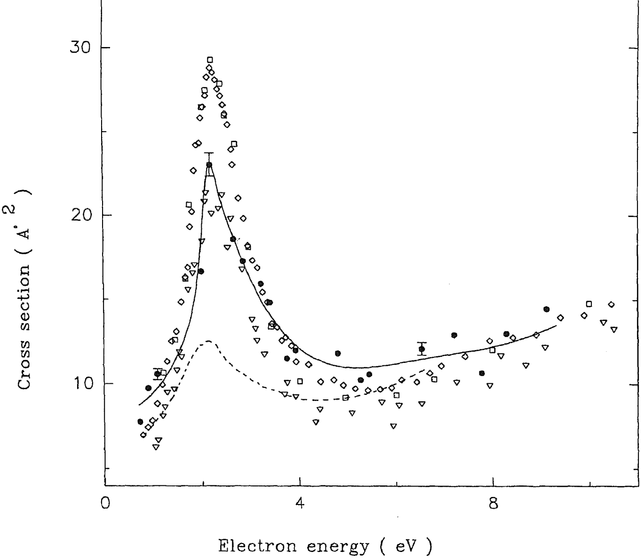

Figure 1. Total electron scattering cross section for nitrous oxide as a function of incident electron energy from 0.73–9.14 eV obtained by different researchers. The symbols denote as follows: ▽, Brüche [3]; — — —, Zecca [5]; ◇, Szmytkowski *et al* [6]; □, Kwan *et al* [7]; ●, present work; ————, cross section curve after proper curve fitting (present work).

have been taken from Samson and Yin [15]. The ratios of $I_{\lambda 01}$ and $I_{\lambda 02}$ were determined from the beam splitter as described previously by Kumar *et al* [11].

When source and target gas species are the same, the electron scattering cross sections could be calculated by the equation given below:

$$\ln\left(\frac{I_{e2}}{I_{e1}}\frac{I_{\lambda 01}}{I_{\lambda 02}}\frac{P_1}{P_2}\right) = \frac{P_1 - P_2}{760}[n_0\sigma x + k(al_1 + l_2)]. \tag{2}$$

The electron scattering cross sections for nitrous oxide were measured using equations (1) and (2) respectively in the two cases described above. In both these equations, all parameters I_{e1}, I_{e2}, $I_{\lambda 01}$, $I_{\lambda 02}$, P_1 and P_2 could be determined experimentally and cross sections could be deduced.

All errors in the measurement of electron-scattering cross sections have been discussed in detail previously by the present authors. In the present experiment, the most probable error was estimated to be ±3%. The problem of inadequate discrimination against forward scattered electrons has been attempted to estimate the magnitude of this effect on the measured cross sections in the experimental set-up used by us. A Monte Carlo method was developed and the electron trajectories originating from the ionization region and terminating at the detector were numerically studied using five random generators i.e. the finite length of the ionization region where photoelectrons are produced, random angle of projection within the allowed cone of ejection determined by the geometry, spread in energy of the photoelectrons determined by thermal broadening, place where a chosen fraction of the emitted photoelectrons are undergoing forward scattering and deflection in angle within a specified cone due to forward scattering. Assuming a differential scattering cross section of $100\,\text{Å}^2$ per steradian, the error in total cross section due to lack of discrimination of forward scattered electrons was found to be dependent on the overall cone angle of emergence. For our experimental set-up where the overall cone angle of emergence has been estimated to be 6°, the maximum error has been found to be about 0.5%.

The total electron-scattering cross sections for nitrous oxide as measured in the present experiment are shown in figure 1 for electron energies ranging from 0.73–9.14 eV along with error bars at three energies only. Also shown in the figure are the measured cross sections of Brüche [3], Zecca *et al* [5], Szmytkowski *et al* [6] and Kwan *et al* [7]. The cross section values reported by Ramsauer and Kollath [4] is not shown in the figure as there are only 10 cross section values available at energies from 0.1–1.2 eV and 3 values between 0.7 to 1.2 eV. The energy width for electron beams used by Kwan *et al* [7] was about 100 meV and the experimental error for absolute total cross section measurement was about 5% at 1.2 eV and 3% at higher electron energies.

Szmytkowski *et al* [6] reported an overall experimental error (calculated as the linear sum of all single contributions) of 10% at the lowest electron energy, rising to 12% at the sharp maxima and decreasing to 8% at and above 10 eV. The energy spread of the electron beam used by their group was about 70 meV. Relative total scattering cross sections were measured by Zecca *et al* [5] in an attempt to locate broad resonance, if any, and to determine the absolute size of the sharp resonances observed by Sanche and Schulz [9]. However, their relative cross sections were normalized at 4 eV to the value obtained by Brüche [3] at the same energy. Also shown in figure 1 is the cross section curve after proper curve fitting to the results obtained in the present experiment. This has been carried out using an appropriate mathematical function in the library of large number of such functions available in the Tablecurve–2D (Jandel Scientific) software for which the regression coefficient is closest to unity. It may be pointed out here that the theoretically computed electron scattering cross sections for nitrous oxide have not been shown in figure 1 as these have not been reported so far in literature by any research group.

For the sake of discussion, the cross section curve (figure 1) in the entire electron energy range from 0.73–9.14 eV has been divided into two regions. These include regions below 5.5 eV and between 5.5 and 9.14 eV. In the first energy region a sharp increase in involved was the ${}^2\sum^+$ of the N_2O^- ion. From figure 1, it is clear that the cross section values at the maximum of the resonance peak and also at the wings on both sides of the peak show large discrepancies. To have a clear comparison, the cross section curves reported by Brüche [3], Zecca *et al* [5], Szmytkowski *et al* [6] and Kwan *et al* [7] along with the curve obtained in the present experiment have been made to undergo proper curve fitting procedure. This has been done with the help of Tablecurve–2D (Jandel Scientific) software. The energy and the cross section value at the peak of the shape resonance thus obtained are 2.3 eV and 28.8 Å^2 [6], 2.3 eV and 29.1 Å^2 [7], 2.1 eV and 12.5 Å^2 [5], 2.3 eV and 21.9 Å^2 [3], and 2.2 eV and 23.2 Å^2 (present work) respectively. The electron energy value at the peak of the shape resonance has been reported by different research groups to be the same but the cross section values have been found to be different. The cross section values reported at the peak by Szmytkowski *et al* [6] and Kwan *et al* [7] are same within the stipulated experimental errors but these values are larger by about 25% as compared to the cross section obtained in the present measurement. The cross section value measured in the present work is about 6% higher than that obtained by Brüche [3] whereas the value given by Zecca *et al* [5] is about 46% lower than that reported in the present work. It has been mentioned earlier in the text that the relative data of Zecca *et al* [5] has been normalized at 4.0 eV to the cross section value reported by Brüche [3]. It is difficult to visualize why the normalization was carried out at 4.0 eV because this energy neither corresponds to the maximum nor the minimum of the resonance peak. Also, the ratio of the cross section values at the maximum and the minimum (9.1 Å^2 at 4.4 eV electron energy) of the resonance peak after normalization is extremely small i.e. about 1.4. In comparison, such a ratio varies from 2.1 to 3.2, the smallest and the largest being obtained from data reported in the present experiment and by Kwan *et al* [7]. Incidentally, the shape resonance passes through the minima at 5.4 eV, 5.1 eV, 5.0 eV and 5.2 eV having cross section values 9.6, 9.0, 8.3 and 11.0 Å^2 as given by Szmytkowski *et al* [6], Kwan *et al* [7], Brüche [3] and the authors in the present work respectively. Except for Zecca's results, all other four measurements are fairly reliable. However, there are two sets of cross section values available from the four measurements for the peak of the shape resonance. One set of values, from Szmytkowski *et al* [6] and Kwan *et al* [7] is about 28% higher than that given by Brüche [3] and authors in the present work. At this stage, it may be worthwhile to discuss about error in all the four measurements associated with incomplete discrimination against projectiles at small angles in the forward direction. In the present experiment, the maximum error because of lack of such discrimination has been found to be about 0.5% whereas such an error in the measurements by Kwan *et al* [7] is also small, of the order of 0.5 to 1%. Brüche [3] has not discussed about this potential source of error associated with their instrument, whereas Szmytkowski *et al* [6] have found an error of about 1% at 60 eV and even smaller at lower energies. In view of the above discussion, it is clear that two sets of cross section values exist for the peak of the shape resonance and this controversy needs to be resolved in future.

In the energy region from 5.5–9.14 eV, the cross section curve after passing through a minimum on the decreasing wing of the main shape resonance peak shows an increasing trend in cross sections at higher energies. In the measurements reported by Zecca *et al* state for the corresponding electron energy.

Ionizing line (Å)	Source gas	Photo-ion state	Electron energy (eV)	Cross section (Å^2)
744	Ar	$^2P_{1/2}$	0.73	7.76
744	Ar	$^2P_{3/2}$	0.91	9.74
736	Ar	$^2P_{3/2}$	1.09	10.56
744	Kr	$^2P_1$	2.00	16.66
736	Kr	$^2P_1$	2.18	23.02
744	Kr	$^2P_{3/2}$	2.66	18.58
736	Kr	$^2P_{3/2}$	2.85	17.28
744	Xe	$^2P_{1/2}$	3.23	15.94
736	Xe	$^2P_{1/2}$	3.41	14.82
744	N_2O	$\tilde{X}\,^2\Pi(\nu = 0)$	3.76	11.52
736	N_2O	$\tilde{X}\,^2\Pi(\nu = 0)$	3.94	12.00
584	N_2O	$\tilde{A}\,^2\Sigma^+(\nu = 0)$	4.81	11.84
584	Ar	$^2P_{1/2}$	5.28	10.25
584	Ar	$^2P_{3/2}$	5.46	10.61
584	Kr	$^2P_{1/2}$	6.55	12.11
584	Kr	$^2P_{3/2}$	7.22	12.92
584	Xe	$^2P_{1/2}$	7.78	10.68
584	N_2O	$\tilde{X}\,^2\Pi(\nu = 0)$	8.31	13.01
584	Xe	$^2P_{3/2}$	9.14	14.48

case, the difference being more than the stipulated experimental errors. The cross section values reported in the present experiment in this electron energy region are the highest whereas those reported by Brüche [3] are the lowest.

The values of scattering cross sections for nitrous oxide as measured in the present experiment are given in table 1 along with the photon wavelength, source gas and the photon state for the corresponding electron energy.

As nitrous oxide and carbon dioxide molecules are isoelectronic and linear in their ground state, it may be interesting to find out the difference in the electron scattering cross section curves for the two molecules. The cross section measurements for the CO_2 have also been carried out by the present authors and these would be published elsewhere in detail. Our measurements in the case of these two molecules show two broad features. Qualitatively, the shape of the cross section curves of N_2O and CO_2 has striking similarities, but quantitatively, it has been found that the cross section values for CO_2 are smaller than those obtained for N_2O at all electron energies below 10 eV. Secondly, the resonance peaks have been found at different electron energies ie. 2.3 and 3.8 eV for N_2O and CO_2 respectively. It may be worthwhile to make an attempt to explain at least the first broad feature. N_2O is a polar molecule with a permanent dipole moment whereas CO_2 is a non-polar molecule. It has been found that at smaller angles, the differential cross sections at intermediate energies are larger in the case of polar molecules than those for the non-polar molecules [16, 17]. It is presumed that the same is true at low electron energies also. In that case, the total cross sections would also be larger in case of molecules having permanent dipole moment.

References

[1] K E Fox and J Reid, *J. Opt. Soc. Am.* **B2**, 807 (1985)

[2] W C Wang and N D Sze, *Nature (London)* **286**, 589 (1981)

[3] E Brüche, *Ann. Phys. Lpz.* **83**, 1065 (1927)

[4] C Ramsauer and R Kollath, *Ann. Phys. Lpz.* **7**, 176 (1930)

[5] A Zecca, I Lazzizzera, M Krauss and C E Kuyatt, *J. Chem. Phys.* **61**, 4560 (1974)

[6] C Szmytkowski, G Karwasz and K Maciag, *Chem. Phys. Lett.* **107**, 481 (1984)

[7] Ch K Kwan, Y F Hsieh, W E Kauppila, S J Smith, T S Stein and M N Uddin, *Phys. Rev.* **52**, 1417 (1984)

[8] M J W Boness, J B Hasted and I W Larkin, *Proc. R. Soc. (London)* **A305**, 493 (1968)

[9] L Sanche and G J Schulz, *J. Chem. Phys.* **58**, 479 (1973)

[10] L Dube and A Herzenberg, *Phys. Rev.* **A11**, 1314 (1975)

[11] V Kumar, E Krishnakumar and K P Subramanian, *J. Phys.* **B20**, 2899 (1987)

[12] K P Subramanian and V Kumar, *J. Phys.* **B20**, 5505 (1987)

[13] K P Subramanian and V Kumar, *J. Phys.* **B22**, 2387 (1989)

[14] K P Subramanian and V Kumar, *J. Phys.* **B23**, 745 (1990)

[15] J A R Samson and L Yin, *J. Opt. Soc. Am.* **B6**, 2326 (1989)

[16] J P Bromberg, *J. Chem. Phys.* **52**, 1243 (1970)

[17] S S Tayal, A Jain, A N Tripathi and M K Srivastava, *J. Chem. Phys.* **78**, 3021 (1983)

Hyperspherical calculation for electron hydrogen atom ionization collisions in a symmetric form

J N DAS
Department of Applied Mathematics, University College of Science, 92, Acharya Prafulla Chandra Road, Calcutta 700 009, India
Email: jndas@cubmb.ernet.in

MS received 15 July 1997; revised 10 November 1997

Abstract. The hyperspherical partial wave method (Das [7]) has been presented here in a symmetric form so that effects of coupling among different partial waves may be included in a systematic way. It is also outlined here how to solve the relevant coupled set of radial wave equations numerically. Some preliminary results are presented for S, P and D waves in the low energy domain of 30–50 eV for the incident electron. In this calculation only two important partial waves are included in each channel. The results are compared with experimental ones and appear very encouraging.

Keywords. Hyperspherical; ionization; cross section; partial wave; channel; close-coupling.

PACS No. 34.80

1. Introduction

Three very successful methods of calculating total cross sections for ionization of hydrogen atoms by electrons at low energies are the convergent close-coupling (CCC) method (Bray and Stelbovics [1, 2]), the *R*-matrix with pseudostates (RMPS) method (Bartschat *et al* [3]) and the hyperspherical close-coupling (HSCC) method (Kato and Watanabe [4]). All these methods give good total cross values (see [4, 5]) down to very low energies. However their capabilities in reproducing the differential cross sections have not been tested (except in one or two cases such as in Bray *et al* [6]). Moreover each of these methods has its own difficulties and limitations. Another, very similar approach, is the hyperspherical partial wave (HSPW) method, suggested by the present author [7]. This is perhaps a better approach. Since this approach is straightforward and most natural, it is just an extension of the partial wave method so useful in two-body scattering calculations. It is also free from any pathological difficulty such as the non-existence of certain integrals for some of the angular momenta for the partial waves (see the second paragraph after eq. (2) of ref. [6]). It also does not require additional knowledge such as in HSCC calculation where one needs the values of the wave function in the asymptotic domain for matching purpose from some other sources. Moreover such values are known only approximately and no analytic solution exists for the asymptotic domain. Some obtained following this approach, for Erhardt asymmetric geometry [8] and for coplanar constant θ_{12} geometry [9], θ_{12} being the angle between the outgoing electrons. In these calculations effects of coupling among different partial waves, in hyperspherical coordinates, are neglected. To include the effects of coupling among different partial waves it will be better to proceed in a symmetric form as is indicated below. In our earlier papers [7–9] we did not consider the problem of how to solve the resultant coupled set of radial wave equations numerically. Here we paid attention to this very problem and outlined a method. Following the present approach some calculations have also been done. Here we report also these preliminary results. In § 3 we describe the present symmetric approach which intends to include fully the coupling effects. In § 3 we describe the calculations of the present article. Results for S, P and D waves are reported in § 4. Some concluding remarks are made in § 5.

2. Hyperspherical calculation in a symmetric form

We consider ionization of a hydrogen atom in its ground state by an electron of incidence energy E_{i} and momentum $\mathbf{p}_{\mathrm{i}}$, the momentum of the ejected and scattered electrons being $\mathbf{p}_1$ and $\mathbf{p}_2$ and coordinates $\mathbf{r}_1$, $\mathbf{r}_2$.

Then ionization amplitude for symmetry S is given by

$$f^S = -(2\pi)^2 \langle \Psi_{\mathrm{fs}}^{(-)} | V_{\mathrm{i}} | \Phi_{\mathrm{i}} \rangle, \tag{1}$$

where $S = 0$ or 1 corresponding to a symmetric or an antisymmetric wave function. Here

$$V_{\mathrm{i}}(\mathbf{r}_1, \mathbf{r}_2) = (1/r_{12}) - (1/r_2),$$
$$\Phi_{\mathrm{i}}(\mathbf{r}_1, \mathbf{r}_2) = (1/2\sqrt{2\pi^2})\mathrm{e}^{-r_1} \cdot \mathrm{e}^{i\mathbf{p}_{\mathrm{i}} \cdot \mathbf{r}_2}$$

and $\Psi_{\mathrm{fs}}^{(-)}$ is the exact scattering state wave function in the final channel with symmetry S and satisfying incoming converging boundary condition. Here we indicate how one can calculate $\Psi_{\mathrm{fs}}^{(-)}$, and hence the scattering amplitude using hyperspherical coordinates $(R, \alpha, \hat{r}_1, \hat{r}_2)$, where

$$R = \sqrt{r_1^2 + r_2^2}, \qquad \alpha = \tan^{-1}(r_2/r_1).$$

We set

$$P = \sqrt{p_1^2 + p_2^2}, \qquad \alpha_0 = \tan^{-1}(p_2/p_1)$$

and use the notations $\omega = (\alpha, \hat{r}_1, \hat{r}_2)$, $\omega_0 = (\alpha_0, \hat{p}_1, \hat{p}_2)$.

Now we note that plane wave has the expansion [7]

$$\exp(i\mathbf{p}_1 \cdot \mathbf{r}_1 + i\mathbf{p}_2 \cdot \mathbf{r}_2)/(2\pi)^3 = (2/\pi)^{1/2} \sum i^{\lambda} (j_{\nu_\lambda}(\rho)/\rho^{3/2}) \varphi_\lambda^*(\omega_0) \varphi_\lambda(\omega), \tag{2}$$

angular momentum for the individual electrons.

Henceforth λ stands for the eigenvalue $l_1 + l_2 + 2n$ or the set (l_1, l_2, n, L, M) depending on the context and $\nu_\lambda = \lambda + 3/2$, $\rho = PR$. For our present formulation it is necessary to consider the symmetrized plane wave function, which may be expanded in hyperspherical coordinates using the symmetrized angular wave function [10]

$$\begin{aligned}\varphi_\lambda^S(\omega) &= (1/(2)^{1/2})\{P_{l_1 l_2}^n(\alpha) Y_{l_1 l_2}^{LM}(\hat{r}_1, \hat{r}_2) + (-1)^{l_1+l_2-L+S+n} \\ &\qquad \times P_{l_2 l_1}^n(\alpha) Y_{l_2 l_1}^{LM}(\hat{r}_1, \hat{r}_2)\} \quad \text{for } l_1 \neq l_2 \\ &= \tfrac{1}{2}[1 + (-1)^{-L+S+n}] P_{ll}^n(\alpha) Y_{ll}^{LM}(\hat{r}_1, \hat{r}_2), \quad \text{for } l_1 = l_2 = 1. \end{aligned} \tag{3}$$

These wave functions are orthonormal and have definite values of (L, M, S, π), π standing for parity and taking values 0 or 1. Then one can easily prove that

$$\begin{aligned}&\{\exp(i\mathbf{p}_1 \cdot \mathbf{r}_1 + i\mathbf{p}_2 \cdot \mathbf{r}_2) + (-1)^S \exp(i\mathbf{p}_1 \cdot \mathbf{r}_2 + i\mathbf{p}_2 \cdot \mathbf{r}_1)\}/(2\pi)^3 \\ &\quad = 2(2/\pi)^{1/2} \sum_{\substack{l_1 \leq l_2 n \\ LM}} i^\lambda (j_{\nu_\lambda}(\rho)/\rho^{3/2}) \varphi_\lambda^{S*}(\omega_0) \varphi_\lambda^S(\omega). \end{aligned} \tag{4}$$

We consider symmetrized final scattering state $\Psi_{\text{fs}}^{(-)}$ with incoming boundary condition. This state may be expanded as

$$\Psi_{\text{fs}}^{(-)}(R, \omega) = (2/\pi)^{1/2} \sum_{\substack{l_1 \leq l_2 n \\ LM}} (F_\lambda^S(\rho)/\rho^{5/2}) \varphi_\lambda^S(\omega). \tag{5}$$

The radial wave functions $F_\lambda^S(\rho)$'s satisfy the equations

$$[(\mathrm{d}^2/\mathrm{d}\rho^2) + 1 - (\nu_\lambda(\nu_\lambda + 1))/\rho^2] F_\lambda^S + \sum_{\lambda'} (2\gamma_{\lambda\lambda'}^S/\rho) F_{\lambda'}^S = 0, \tag{6}$$

where

$$\begin{aligned}\gamma_{\lambda\lambda'}^S &= (1/P)\langle \varphi_\lambda^S | C | \varphi_{\lambda'}^S \rangle, \\ C &= (1/\cos\alpha) + (1/\sin\alpha) - (1/|\hat{r}_1 \cos\alpha - \hat{r}_2 \sin\alpha|).\end{aligned}$$

At this point an explanation is in order why the formulation of the problem in symmetric form is expedient. Because of conversation laws, for any fixed $\mu = (L, S, \pi)$ only radial waves with this particular μ enter in a coupled set of equations, reducing considerably the computational problem.

In the above equations those λ, λ' occur for which there are fixed values of L, M, S and π. For the present case $M = 0$ only needs consideration, since in the calculation of the scattering amplitude, given by equation (1), only states with $M = 0$ gives a non-zero contribution. Henceforth we fix $M = 0$ everywhere. Now we denote (L, S, π) by the single letter and introduce a single index N in place of (l_1, l_2, n). Then we have $F_\lambda^S(\rho) = f_N^\mu(\rho)$ and equation (6) becomes

$$[(\mathrm{d}^2/\mathrm{d}\rho^2) + 1 - ((\nu_N^\mu(\nu_N^\mu + 1)/\rho^2)] f_N^\mu(\rho) + \sum_{N'} (2\gamma_{NN'}^\mu/\rho) f_{N'}^\mu(\rho) = 0, \tag{7}$$

where $\nu_\lambda \equiv \nu_N^\mu$, $\gamma^S_{\lambda\lambda'} \equiv \gamma^\mu_{NN'}$ for each fixed μ and N. In any realistic calculation N, N' are restricted to certain maximum value $N_{mx} \cdot N_{mx}$ depends on μ, but this will not be explicitly indicated here.

Now we consider particular solutions of the above set of equations. It may be noted that there are two particular sets of solutions $\mathbf{f}_{sn}^{\mu(k)}(\rho)$ and $\mathbf{f}_{cs}^{\mu(k)}(\rho)$ which behave asymptotically as

$$f_{snN}^{\mu(k)}(\rho) \sim a_{kN}^\mu \sin(\rho + \beta_k^\mu \ln 2\rho), \quad \rho \to \infty$$

and

$$f_{csN}^{\mu(k)}(\rho) \sim b_{kN}^\mu \cos(\rho + \beta_k^\mu \ln 2\rho), \quad \rho \to \infty.$$

Here β_k^μ is the kth eigenvalue of the charge matrix $A^\mu = (\gamma^\mu_{NN'})$ and

$$\mathbf{X}_k^\mu = \begin{pmatrix} a_{k1}^\mu \\ \vdots \\ a_{kN_{mx}}^\mu \end{pmatrix}, \qquad \mathbf{Y}_k^\mu = \begin{pmatrix} b_{k1}^\mu \\ \vdots \\ b_{kN_{mx}}^\mu \end{pmatrix}$$

are the kth eigenvectors of it. We determine particular solutions $\mathbf{f}_{sn}^{\mu(k)}$ and $\mathbf{f}_{cs}^{\mu(k)}$ in the asymptotic region by substituting

$$f_N(\rho)^{\mu(k)} = \sum_{l=0}^{\infty} a_{kN}^{\mu(l)} (\sin\theta_k^\mu/\rho^l) + \sum_{l=0}^{\infty} b_{kN}^{\mu(l)} (\cos\theta_k^\mu/\rho^l), \tag{8}$$

where $\theta_k^\mu = \rho + \beta_k^\mu \ln 2\rho$ in the differential equation (7) and on equating coefficients of $\sin\theta_k/\rho^{l+1}$ and $\cos\theta_k/\rho^{l+1}$ to zero. Thus we have the following recurrence relations for the unknowns

$$\begin{aligned} 2[(A_k^\mu)^2 + l^2] X_k^{\mu(l)} &= [A_k^\mu \Lambda_k^\mu - l(l-1)A_k^\mu - l(2l-1)\beta_k^\mu I]\mathbf{X}_k^{\mu(l-1)} \\ &\quad - [(2l-1)\beta_k^\mu A_k^\mu + l\Lambda_k^\mu - l^2(l-1)I]\mathbf{Y}_k^{\mu(l-1)}, \end{aligned} \tag{9a}$$

$$\begin{aligned} 2[(A_k^\mu)^2 + l^2] \mathbf{Y}_k^{\mu(l)} &= [A_k^\mu \Lambda_k^\mu - l(l-1)A_k^\mu - l(2l-1)\beta_k^\mu I]\mathbf{Y}_k^{\mu(l-1)} \\ &\quad + [(2l-1)\beta_k^\mu A_k^\mu + l\Lambda_k^\mu - l^2(l-1)I]\mathbf{X}_k^{\mu(l-1)}, \end{aligned} \tag{9b}$$

where

$$\begin{aligned} &(\mathbf{X}_k^{\mu(l)})_N = a_{kN}^{\mu(l)}, \quad (\mathbf{Y}_k^{\mu(l)})_N = b_{kN}^{\mu(l)}, \\ &A_k^\mu = A^\mu - \beta_k^\mu I, \quad (\Lambda_k^\mu)_{NN'} = [(\beta_k^\mu)^2 + \nu_N^\mu(\nu_N^\mu + 1)]\delta_{NN'}. \end{aligned}$$

The above equations with the initial conditions

$$\mathbf{X}_k^{\mu(0)} = \mathbf{X}_k^\mu, \quad \mathbf{Y}_k^{\mu(0)} = \mathbf{0}$$

give $\mathbf{f}_{sn}^{\mu(k)}(\rho)$ and the conditions

$$\mathbf{X}_k^{\mu(0)} = \mathbf{0}, \quad \mathbf{Y}_k^{\mu(0)} = \mathbf{X}_k^\mu$$

Now the physical solution will be a superposition

$$f^{\mu}_{N}(\rho) = \sum_{k} c^{\mu}_{k} f^{\mu(k)}_{snN}(\rho) + \sum_{k} d^{\mu}_{k} f^{\mu(k)}_{csN}(\rho). \tag{10}$$

The partial wave containing $\varphi^{S}_{\lambda_N}(\omega)$ will be then

$$(2/\pi)^{1/2} \sum_{k} (c^{\mu}_{k} + i d^{\mu}_{k}) a^{\mu}_{kN} (\exp(i(\rho + \beta^{\mu}_{k} \ln 2\rho))/2i\rho^{5/2}) \varphi^{S}_{\lambda_N}(\omega),$$

λ_N corresponds to the set λ for the index N and for fixed μ. This must agree (apart from a Coulomb distortion) with the part

$$2(2/\pi)^{1/2} i^{\lambda_N} \exp(i(\rho - \nu^{S}_{N}\pi/2))/2i\rho^{5/2}) \varphi^{S*}_{\lambda_N}(\omega_0) \varphi^{S}_{\lambda_N}(\omega)$$

of the symmetrized plane wave in order that $\Psi^{(-)}_{\text{fs}}$ be asymptotically a superposition of (distorted) symmetrized plane wave plus incoming converging waves. So we have,

$$\sum_{k} (c^{\mu}_{k} + i d^{\mu}_{k}) a^{\mu}_{kN} = 2 \exp(i(\lambda_n - \nu_N)\pi/2) \varphi^{S*}_{\lambda_N}(\omega_0). \tag{11}$$

Putting $p^{\mu}_{k} = c^{\mu}_{k} + i d^{\mu}_{k'}$, $q^{\mu}_{k} = c^{\mu}_{k} - i d^{\mu}_{k}$ we have

$$X^{\mu}\mathbf{P}^{\mu} = -2\exp(i\pi/4) \begin{pmatrix} \varphi^{\mu*}_{1}(\omega_0) \\ \vdots \\ \varphi^{\mu*}_{Nmx}(\omega_0) \end{pmatrix},$$

where

$$\mathbf{P}^{\mu} = \begin{pmatrix} p^{\mu}_{1} \\ \vdots \\ p^{\mu}_{N_{mx}} \end{pmatrix} \quad \text{and } X^{\mu} = (\mathbf{X}^{\mu}_{1}, \mathbf{X}^{\mu}_{2}, \ldots, \mathbf{X}^{\mu}_{N_{mx}}).$$

Then

$$\mathbf{P}^{\mu} = -2\exp(i\pi/4)(X^{\mu})^{-1} \begin{pmatrix} \varphi^{\mu*}_{1}(\omega_0) \\ \vdots \\ \varphi^{\mu*}_{N_{mx}}(\omega_0) \end{pmatrix}. \tag{12}$$

Here the inverse $(X^{\mu})^{-1}$ exists since X^{μ} is actually the similarity transformation which diagonalizes the symmetric charge matrix A^{μ}.

Next we construct N_{mx} independent solutions of equation (7) which vanish at origin. We denote the corresponding solution vectors by $\mathbf{f}^{\mu(k)}_{0}$, $k = 1, 2, \ldots, N_{mx}$. Then the physical solution vector may also be written as

$$\mathbf{f}^{\mu}(\rho) = \sum_{k} \frac{1}{2} G_k \mathbf{f}^{\mu(k)}_{0}(\rho). \tag{13}$$

We match values of radial waves (and their derivatives) given by right hand sides of

$$f_N^{\mu}(\rho) = \frac{1}{2}\sum_k (g_{RK} + i g_{IK}) f_{0N}^{\mu(k)}(\rho), \tag{14}$$

where g_{RK} and g_{IK} turns out in the forms

$$g_{RK} = \sum_{N'} g_{KN'}^{(1)} \varphi_{N'R}^{\mu}(\omega_0) + \sum_{N'} g_{KN'}^{(2)} \varphi_{N'I}^{\mu}(\omega_0)$$

and

$$g_{IK} = \sum_{N'} g_{KN'}^{(3)} \varphi_{N'R}^{\mu}(\omega_0) + \sum_{N'} g_{KN'}^{(4)} \varphi_{N'I}^{\mu}(\omega_0), \tag{15}$$

and $\varphi_{N'R}^{\mu}(\omega_0)$ and $\varphi_{N'I}^{\mu}(\omega_0)$ are the real and imaginary parts of $\varphi_{N'}^{\mu}(\omega_0)$. In this way radial waves $f_N^{\mu}(\rho)$'s are determined for the scattering states

$$\Psi_{\mathrm{fs}}^{(-)}(\rho) = (2/\pi)^{1/2} \sum_{\lambda_N} (f_N^{\mu}(\rho)/\rho^{5/2}) \varphi_{\lambda_N}^{S}(\omega). \tag{16}$$

This on substituting in equation (1) gives the scattering amplitude and hence the cross sections.

3. Calculations

From the results of CCC and RMPS calculations of Bartschat and Bray [5] it is now known that at low energies S, P and D waves give most significant contributions to the total cross section, P wave itself accounting for more than 50%. So we include in our calculations only the channel ${}^{1,3}S^e$, ${}^{1,3}P^0$ and ${}^{1,3}D^e$. Here a channel corresponds to fixed values of $(L, S, P) = \mu$. We report two sets of results. In one of these only one, most important, partial wave in each channel is retained. For example ${}^{3}P^0$ includes the partial wave with $l_1 = 0, l_2 = 1, n = 0$ only. In the second calculation we include two important partial waves in each channel. These are shown in table 1.

In our present scheme, determination of solution of the coupled set of equations [7] is the most difficult task. As is described in §2 the equations are solved by matching method. In the asymptotic domain solutions $\mathbf{f}_{sn}^{(k)}(\rho)$ and $\mathbf{f}_{cs}^{(k)}(\rho)$ are determined from asymptotic expansion (equations (8) and (9)). Then another set of solutions are continued from the neighbourhood of origin, say starting at ε (with $\varepsilon = 0.1$). At this point N_{mx} solutions are constructed with initial values zero and derivatives δ_{NK} for the Nth element of the kth solution vector. These are then continued numerically to ρ_{int}, a point in the asymptotic domain. In this numerical integration of the equations (8) we adopted a Tailors expansion with 10 terms in steps $\Delta\rho = 0.01$ initially up to 0.2, then in steps $\Delta\rho = 0.05$ up to 0.2, then with $\Delta\rho = 0.2$ up to ρ_{∞}, a point beyond which no contribution arises in the T-matrix elements. ρ_{int} was varied from 20 a.u. to about 150 a.u. in steps of 5 or 10 a.u.. In general there was good agreement in the results for different matching points ρ_{int}. But occasionally there were oscillations also. In some instances there were some spurious singular like behaviours. With further change in the value of ρ_{int}, the results again become what it should be. The results presented in the next section were obtained from observation of

$^1S^e$	$^3S^e$	$^1P^0$	$^3P^0$	$^1D^e$	$^3D^e$
(0,0,0)	(0,0,1)	(0,1,0)	(0,1,0)	(1,1,0)	(1,1,1)
(0,0,2)	(0,0,3)	(0,1,1)	(0,1,1)	(1,1,2)	(1,1,3)

Table 2. Partial wave cross sections (in a_0^2) for ionization of hydrogen atoms by electrons in different channels in the energy range 30–50 eV for calculations wit $N_{mx} = 2$. Quantities in brackets represent those with $N_{mx} = 1$. Total cross sections ar also presented (which include cross section for F state of RMPS calculations). See tex for details.

E_i (eV)	$\sigma(^1S^e)$	$\sigma(^3S^e)$	$\sigma(^1P^0)$	$\sigma(^3P^0)$	$\sigma(^1D^e)$	$\sigma(^3D^e)$	σ_Tot	σ_Tot (CCC)	σ_Tot (RMPS
30	0.08 (0.06)	0.02 (0.00)	0.06 (0.02)	0.32 (0.36)	0.12 (0.19)	0.00 (0.02)	0.63	0.60	0.58
35	0.10 (0.05)	0.03 (0.00)	0.06 (0.01)	0.28 (0.26)	0.13 (0.17)	0.01 (0.02)	0.65	0.65	0.63
40	0.08 (0.04)	0.05 (0.00)	0.07 (0.01)	0.27 (0.19)	0.12 (0.14)	0.01 (0.01)	0.64	0.68	0.66
45	0.06 (–)	0.05 (–)	0.08 (–)	0.25 (–)	0.11 (–)	0.01 (–)	0.59	0.70	0.68
50	0.06 (–)	0.03 (–)	0.07 (–)	0.24 (–)	0.09 (–)	0.01 (–)	0.53	0.71	0.69

results calculated with different ρ_int in the range noted above. Often average values wer taken as the final results. In these calculations scaling of the wave functions is necessar since for a variation of ρ from say $\rho = 1.0$ to $\rho = 10$ units the wave function changes b many orders. As already stated we made calculations for $N_{mx} = 1$ and $N_{mx} = 2$ only. Fo further increase of N_{mx} often the results become unphysical. This implies that the stabilization of the calculations becomes essential. This problem is left for a futur investigation. Now in obtaining T-matrix elements all the integrations except the integra tion over ρ were done analytically. The ρ-integration was done numerically. In calculatin the partial cross sections from the T-matrix elements the remaining integrations ar amenable to analytical evaluations. In this paper we present only the various partial cros sections and values of certain parameters related to these.

4. Results

Partial wave cross sections for ionization of hydrogen atoms by electrons in the energ range 30–50 eV of our present calculation are presented in table 2. In this table two sets results are presented. One set corresponds to $N_{mx} = 2$ and for comparison a second set presented for $N_{mx} = 1$. For 30, 35 and 40 eV energies the two sets of results are close each other indicating that at these energies most important contributions arises fro single states (0,0,0) in $^1S^e$, (0,0,1) in $^3S^e$, (0,1,0) in $^1P^0$ and $^3P^0$, (1,1,0) in $^1D^e$ and (1,1, in $^3D^e$. As the energy increases, other states in these channels become important. The tw

L	$E_i = 30\,\text{eV}$			$E_i = 50\,\text{eV}$		
	Present ($N_{mx} = 2$)	RMPS	CCC	Present ($N_{mx} = 2$)	RMPS	CCC
0	0.14	0.10	0.13	0.16	0.09	0.09
1	0.63	0.63	0.51	0.57	0.60	0.56
2	0.20	0.23	0.28	0.17	0.24	0.26
3	–	0.05	0.10	–	0.06	0.09

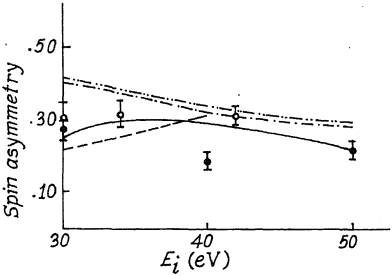

Figure 1. Spin asymmetry for electron impact ionization of hydrogen atoms as a function of the projectile energy. Theory: continuous, present calculation; dash-dotted, CCC [5]; dash-double dotted, RMPS [5]. Experiment: •, Crowe *et al* [12]; ○, Fletcher *et al* [11].

states shown in table 1 in each channel give reasonable contributions to partial cross sections as well as to total cross sections in the energy range 30–40 eV. Total cross sections of the present calculation, the CCC and the RMPS calculations agree quite well (see table 2). Beyond 40 eV, however, the results go to depart considerably. We have not calculated F-channel contributions. F-channel gives about 5% to 10% contributions to the total cross sections at these energies. In calculating the total cross sections we have included the F-channel values of RMPS calculation to our results. Next we look to table 3 where we presented ratios of partial cross sections to the total cross sections. Our results agree well with the CCC results and with the RMPS results for 30 eV energy. For 50 eV energy our S-wave results appear somewhat higher compared to those of other calculations, while the D-wave cross sections are somewhat lower. The P-wave cross sections of these calculations which account for more than 50%, agree reasonably well with one another.

Finally in figure 1 we have presented values of an important parameter of these cross section results. This is the spin asymmetry parameter defined by

$$\text{spin asymmetry} = (\sigma^S - \sigma^T)/(\sigma^S + 3\sigma^T).$$

et al [12]. It is interesting to note that our results for $N_{mx} = 2$ agree beautifully with the experimental results and appear somewhat better compared to the CCC and RMPS results in the above energy range. Excepting one point of Crowe *et al* all these experimental points are very close to our theoretical curve.

5. Conclusion

The results of our present preliminary calculation of electron hydrogen atom ionization collisions, presented here in a symmetric form, and which includes fully the coupling effects, appear very encouraging. Thus simple inclusion of two most important states in each channel gives good representation of the partial wave cross sections in the energy range 30–40 eV. However, for better results and for other energies, one has to include larger number of states in each channel. Matching method also does not appear very efficient. Improved calculations including a large number of partial waves in each channel now appears relatively difficult. Then stabilization of the calculation for the solution of the coupled set of equations will be necessary. Once this is achieved many interesting results and insights in the low energy domain are expected.

References

[1] I Bray and A Stelbovics, *Phys. Rev. Lett.* **69**, 53 (1992)
[2] I Bray and A Stelbovics, *Phys. Rev.* **A46**, 6995 (1992)
[3] K Bartschat, E T Hudson, M P Scott, P G Burke and V M Burke, *J. Phys.* **B29**, 115 (1996
[4] D Kato and S Watanabe, *Phys. Rev. Lett.* **74**, 2443 (1995)
[5] K Bartschat and I Bray, *J. Phys.* **B29**, L577 (1996)
[6] I Bray, D A Konovalov, I E McCarthy and A T Stelbovics, *Phys. Rev.* **A50**, R2818 (1994)
[7] J N Das, *Aust. J. Phys.* **47**, 743 (1994)
[8] J N Das and K Chakrabarti, *Parmana – J. Phys.* **47**, 249 (1996)
[9] J N Das and K Chakrabarti, *Phys. Rev.* **A56**, 365 (1997)
[10] C D Lin, *Phys. Rev.* **A10**, 1986 (1974)
[11] G D Fletcher, M J Alguard, T J Gray, P F Wainwright, M S Lubell, W Raith and V W Hughes *Phys. Rev.* **A31**, 2854 (1985)
[12] D M Crowe, X Q Guo, M S Lubell, J Slevin and M Eminyan, *J. Phys.* **B23**, L325 (1990)

Numerical modeling of laser matter interaction in the presence of an ambient gas

A NEOGI and R K THAREJA*
Department of Physics and Centre for Laser Technology, Indian Institute of Technology, Kanpur, 208 016, India
* To whom all correspondence should be addressed

MS received 3 March 1997; revised 12 August 1997

Abstract. A one dimensional numerical model to simulate the laser matter interaction in the presence of an ambient gas is presented. The model is developed by making appropriate modifications in MEDUSA, a one dimensional Lagrangian computer code, which simulates laser plasma interaction in vacuum. Various parameters of the plasma such as velocity, electron temperature, ion temperature, density, pressure, shock wave intensity of the plasma as it expands into a background gas are simulated. The results are compared with the experimental observations.

Keywords. Ablation; modeling; laser; ambient gas; MEDUSA.

PACS Nos **52.65; 52.40; 52.50**

1. Introduction

The study of laser-matter interaction has been a subject of paramount importance in recent years. There have been reports on laser-matter interaction in the presence of an ambient gas [1–6], electric field [7, 8] and magnetic field [9]. The genesis of this study is to understand the interaction of a high power pulsed laser beam with a solid target in the presence of an ambient gas and to develop a comprehensive numerical model for the process. The laser ablation at moderate intensity is particularly important because of its application in thin film deposition [3] and laser drilling [10–12]. Further, the interaction between laser produced plasma and ambient gas is of interest because it provides information on collisional, collective and electromagnetic processes in astrophysical and laboratory plasmas [13] and can help in the solution of various practical problems [14].

Since late seventies there have been several attempts to develop a theoretical model for understanding laser-matter interaction in ambient atmosphere but every model has some limitations. Knight [15] developed a theoretical model which was generalized by Bellantone *et al* [10, 11] but its usage was restricted to relatively low intensity regime. Aden *et al* [12] developed a three dimensional model which matched well with their experimental data. Macfarlane *et al* [16] and Giuliani *et al* [17] had given two separate models for the same experiment which was valid above 1 Torr but failed at higher pressure. Ananin *et al* [18] had given a model for plasma expansion at low works well at higher pressure. However, model is true for an instantaneous point explosion and with negligible radiation losses. Further, the model is insufficient for getting the detailed thermodynamic and hydrodynamic properties of the blast wave.

The present paper deals with the case of intermediate intensity regime, 10^8–10^{12} W/cm^2 and higher pressures. We take help of the modified version of the laser fusion code MEDUSA [20], MED101. This is an one dimensional Lagrangian code which calculates hydrodynamic and thermodynamic behaviour of the laser produced plasma in vacuum. MED101 is a well developed code which can take care of double and triple layered targets and can calculate X-ray laser gain. We have made modifications in this code to implement it for ambient gas. The Rankine–Hugoniot relations for shock waves are used to calculate the changing boundary conditions, that is temperature and pressure. The Navier Stokes equation is changed due to Reynolds stress arising due to turbulent boundary layer mixing and at a later stage due to diffusion and interparticle collisions. The thermodynamics of the system is also changed accordingly. The equations are solved using the finite difference method.

The results simulated using modified MED101 are compared with the experimental results of Puretzky *et al* [6] where the graphite target was irradiated by focussed beam of KrF laser and the plume expanded into a background of He, Ne, Ar and Xe gas.

2. The numerical model

2.1 *In vacuum*

Here, we present a brief outline of the one dimensional Lagrangian code MEDUSA. A detailed description and the mathematics of the code is available elsewhere [20]. The plasma is assumed to consist of a charge neutral mixture of electrons and various species of ions. MEDUSA treats the thermodynamical properties of the electrons as one subsystem with internal energy u_e per unit total mass, temperature T_e, pressure p_e and specific heat ratio γ_e and so on, and the ions as second subsystem with a corresponding set of variables. Electric and magnetic fields are neglected and the two subsystems are coupled together by a common velocity and by energy exchange due to collisions between them. This is the one fluid two temperature model, the whole of the plasma is considered as one fluid in which electrons and ions have different temperature. According to the first law of thermodynamics

$$\frac{\mathrm{d}Q}{\mathrm{d}t} = \frac{\mathrm{d}U}{\mathrm{d}t} + \frac{\mathrm{d}W}{\mathrm{d}t}, \tag{1}$$

$$S = \frac{\mathrm{d}Q}{\mathrm{d}t} = C_v \frac{\mathrm{d}T}{\mathrm{d}t} + \beta_T \frac{\mathrm{d}\rho}{\mathrm{d}t} + p\frac{\mathrm{d}V}{\mathrm{d}t}, \tag{2}$$

$$C_v = \left(\frac{\delta u}{\delta T}\right)_\rho, \quad \beta_T = \left(\frac{\delta u}{\delta \rho}\right)_T.$$

The source terms S_i and S_e for ions and electrons respectively are written as

$$S_{\mathrm{i}} = H_{\mathrm{i}} - K + Y_{\mathrm{i}} + Q_s, \tag{3}$$

$$S_{\mathrm{e}} = H_{\mathrm{e}} + K + Y_{\mathrm{e}} + J + X. \tag{4}$$

Here H represents the flow of heat due to thermal conduction; K is the rate of energy exchange between ions and electrons; Y is the rate of thermonuclear energy release; J is the Bremstrahlung emission; X is the rate of absorption of laser light; Q_s is the rate of viscous shock heating.

Since plasma is considered to be a fluid, the motion of the plasma is governed by the Navier–Stokes equation

$$\rho \frac{\mathrm{d}u}{\mathrm{d}t} = -\nabla p, \tag{5}$$

where u is the velocity of plasma which defines the motion of the lagrangian coordinate, p is the total pressure due to electrons and ions together with artificial viscous pressure [20].

It is necessary to specify both hydrodynamic and thermodynamic boundary conditions at the inner and outer boundaries. For inner boundary $u(r=0)=0$. For the outer boundary which is moving at a point $r = R_0$ there can be various cases like

$$\begin{aligned} &1.\ p(R_0) = 0,\\ &2.\ u(R_0) = 0, \quad T_{\mathrm{i}}(R_0) = T_{\mathrm{i}}(t), T_{\mathrm{e}}(R_0) = T_{\mathrm{e}}(t),\\ &3.\ p(R_0) = p(t),\\ &4.\ u(R_0) = u(t). \end{aligned} \tag{6}$$

Boundary condition 1 is being the case of plasma expanding in vacuum.

The equation of state assumes perfect gas equation of state for ions and Thomas–Fermi equation of state (with modified expression to give correct solid density) for electrons. These equations are solved along with the mass continuity equation by finite difference method to get temporal and spatial profile of plasma parameters *viz.* ρ, u, T_{i}, T_{e}, n_{i}, n_{e} and also the ionization state of the plasma.

The original MEDUSA code is modified to MED101 to calculate X-ray laser gain. The modified version includes atomic physics and radiation packages which can handle high and low Z materials, and a corrected equation of state for the electrons. The atomic physics package with the help of steady state CORONA model incorporates variable ionization in the plasma assuming equilibrium between collisional ionization and radiative recombination and depends only on electron temperature. It also includes time dependent form of the three body recombination which depends on electron density. In the older version of the code thermal electrons and ions were considered to be the only means of energy transport. The radiation package takes care of the enhanced energy transport due to suprathermal (fast) electrons and photons created at the critical density, whose mean free path is much longer than that of the thermal electrons resulting in fast energy transport [21]. The two equation of state available before were (1) perfect gas equation of state and (2) Fermi Dirac equation of state. Neither of them accounts for changes in ionization and hence the number of free particles remained constant. The Thomas–Fermi equation of state is introduced but it cannot deal with solid or liquid phase because it does not include binding forces. 'Corrected Thomas–Fermi' equation is introduced but it fails

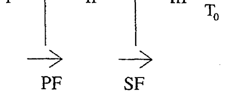

Figure 1. Region I is expanding plasma, region II is compressed gas and region III is the undisturbed gas.

governed by a perfect gas equation of state whereas for electrons one can choose any of the five states stated above.

2.2 *In ambient gas*

As the plasma moves at a velocity of 10^6–10^7 cm/sec into the ambient gas it acts as a supersonic piston giving rise to a shock wave which moves at a faster speed than the piston [22]. If the gas pressure is high (say, > 20 Torr) then there is a constant discontinuity between the piston and the swept up gas and there is hardly any intermixing of the two. A rough sketch of the process is given in figure 1. Region I is the plasma region, region II is the compressed gas ahead of the plasma front and region III is the undisturbed gas where pressure and temperature are P_0 and T_0. Between region I and II is the plasma front which is referred to as supersonic piston. Between region II and III is the shock front which is moving faster than the plasma front.

The velocity of the plasma front V_p and the velocity of shock front V_s are related by the expression [22]

$$V_\mathrm{s} = \frac{(\gamma+1)}{4} V_\mathrm{p} + \sqrt{\frac{(\gamma+1)^2}{16} {V_\mathrm{p}}^2 + {a_1}^2}, \tag{7}$$

where $a_1 = \sqrt{\gamma R T_0}$ is the velocity of sound in the medium and γ the specific heat ratio of the gas.

2.2.1 *Boundary conditions.* The boundary condition on the region I is defined by the pressure and temperature of the region II. Rankine–Hugoniot relations are used to calculate the temperature and pressure of region II. The situation is similar to figure 2(a).

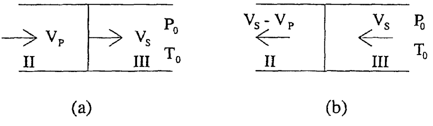

Figure 2. (**a**) The moving shock front as seen from reference frame fixed to earth. (**b**) The stationary shock front as seen from reference frame moving with the shock front.

Here the pressure (P_c) and temperature (T_c) in compressed gas region II across a stationary shock front are given by Rankine Hugoniot relations [22]

$$P_c = P_0\left[\frac{2\gamma}{(\gamma+1)}M_s^2 - \frac{(\gamma-1)}{(\gamma+1)}\right], \tag{8}$$

$$T_c = T_0\left[\frac{2\gamma M_s^2 - (\gamma-1)}{(\gamma+1)^2 M_s^2}\right][(\gamma-1)M_s^2+2], \tag{9}$$

where γ is the specific heat ratio of the gas and $M_s = V_s/a$ is the Mach number i.e the boundary condition is changing with time, the changed boundary conditions are

$$\begin{aligned} P(R_0) &= P_0 \quad \text{if } M_s \le 1 \\ &= P_c \quad \text{if } M_s > 1, \\ T_e(R_0) &= T_0 \quad \text{if } M_s \le 1 \\ &= T_c \quad \text{if } M_s > 1 \end{aligned} \tag{10}$$

If the Mach number is ≤ 1 then shock waves are not formed and the boundary conditions are defined by P_0 and T_0 but if Mach number is > 1 then shock waves are formed and pressure and temperature are given by P_c and T_c respectively.

Here the boundary condition for the temperature is applicable to the electron temperature only. It is because of the higher concentration of electrons at the plasma front due to their higher mobility than that of ions. Here the velocity is being calculated at every step. That is, after every small time step the code calculates the plasma front velocity and simultaneously it calculates the shock front velocity and then the corresponding pressure at the boundary and with that pressure it calculates the next plasma front velocity and this process continues till the end.

2.2.2 *Viscous drag.* When plasma moves into an ambient gas it is almost similar to the case of hot jet coming out into ambient atmosphere. The moving plasma undergoes turbulent boundary layer mixing due to which it experiences viscous force on its boundary.

According to Prandtl's mixing length theory the total Reynolds stress due to turbulent mixing in the boundary layer is given by the expression [24]

$$\tau = \rho\epsilon\frac{\delta u}{\delta y} = \rho x_1 b[u_{\max} - u_{\min}]\frac{\delta u}{\delta y}, \tag{11}$$

where ϵ is kinematic viscosity, ρ is the density of the external gas, $u_{\max}$ is the velocity of the center of flow and $u_{\min}$ is at the boundary. x_1 is an empirical constant to be determined from experiment, b is the width of the mixing zone.

At the outermost boundary, velocity is zero. So $u_{\min} = 0$ and writing $u_{\max} = u$, eq. (11) simplifies to

$$\tau = \rho x_1 u^2. \tag{12}$$

$$F_{\text{drag}} = \tau(\delta l). \tag{13}$$

δl is the length of a particular mesh varying with time. The Navier–Stokes equation (eq. (5)) changes to

$$\rho \frac{\mathrm{d}u}{\mathrm{d}t} = -\nabla p - \tau(\Delta l). \tag{14}$$

2.2.3 *Diffusive force.* As the plasma front expands into the ambient gas the pressure just inside the boundary decreases and the pressure outside increases. At a later time the pressure inside the plasma front is comparable to the pressure outside. At that time the piston becomes leaky and outside gas diffuses into the plasma which gives rise to collisions due to which the expanding plasma experiences a large resistive force

$$F_{\text{diff}} \, \alpha \left(\frac{p_{\text{ext}}}{p_{\text{int}}}\right)^n \rho$$

or

$$F_{\text{diff}} = K\left(\frac{p_{\text{ext}}}{p_{\text{int}}}\right)^n \rho. \tag{15}$$

p_{ext} is the pressure just outside the plasma front and p_{int} is the pressure just inside the plasma front. ρ is the density of the external gas. On addition of a diffusive term the modified Navier–Stokes equation reads

$$\rho \frac{\mathrm{d}u}{\mathrm{d}t} = -\nabla p - \tau(\Delta l) - F_{\text{diff}} = -\nabla p - \rho x_1 u^2 - K\left(\frac{p_{\text{ext}}}{p_{\text{int}}}\right)^n \rho. \tag{16}$$

This equation contains three constants viz. x_1, K and n to be determined from the experiments.

3. Results

With the modifications as above the simulation is carried out with an initial step of $t = 10^{-18}$ sec having mesh size of 60. One of the simulated curves is compared with one of the experimental curves (say Xe) and constants x_1, K and n in eq. (16) are determined. These constants once determined are then used to get other simulated curves (in case of He, Ne and Ar) which are compared with respective experimental curves. The simulated curves are matched with the experimental data of Puretzky *et al.* Here graphite target is ablated by KrF laser ($\lambda = 248$ nm, 30-ns FWHM, $2 \times 2\,\text{mm}^2$ spot size on the target, fluence $= 20\,\text{J/cm}^2$). The ablation is carried out in four different buffer gases at a pressure of 300 Torr. The temporal evolution of the plasma front as it propagates in He, Ne, Ar and Xe gas is shown in figures 3(a)–(d). The simulated results shown in solid line match well with the experimental results, shown in dashed line till 300 nsec. The front propagates faster in lighter gas (like He) than denser gas (like Xe). It is interesting to note that after 300 nsec the simulated value is more than that of the

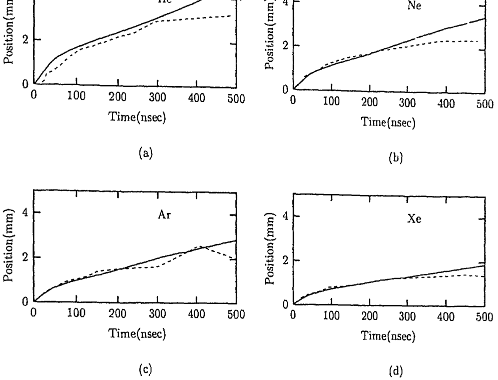

Figure 3. The position of the plasma front versus time in four different ambient gases (**a**) He (**b**) Ne (**c**) Ar and (**d**) Xe. Experiment (- - - -), simulation (——).

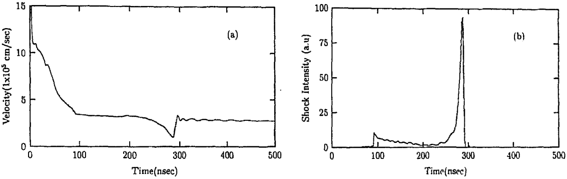

Figure 4. The temporal profile of (**a**) velocity (**b**) shock intensity of the plasma front in Xe gas as obtained from simulation.

experimental one. This is because after 300 ns the diffusion increases to such an extent that a reflected shock is generated within the plasma plume which moves in the opposite direction, towards the target surface, damping the motion of the plasma as observed in the experiment. If there is mixture of fluids whose composition is different at different points then the equations of fluid dynamics have to be considerably modified [25]. So a different set of equations are needed to model this part which is beyond the scope of the paper.

In figure 4(a) the temporal profile of plasma front velocity with Xe as buffer gas as predicted by this numerical model is shown. The velocity decreases with time but at

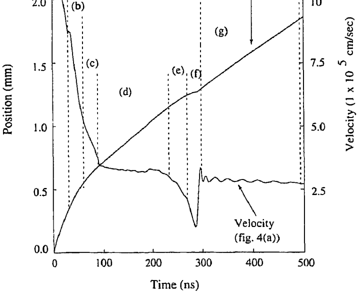

Figure 5. Figure 3(d) and figure 4(a) is replotted with a common time axis.

shock wave going into the plasma as a function of time as observed in simulation. The shock intensity is maximum at around 290 ns, that is at the same time when velocity suddenly drops and increases again. Experimentally it was observed that a shock wave had gone into the plasma front at around 300 ns causing instability in the velocity of the plasma front. The simulated result match very well with the experiment. It has also been observed in simulation that the intensity of shock wave going into the plasma in case of He is orders of magnitude lower than that of Xe. It is because Xe being a denser gas gives a greater thrust to the moving plasma compared to that of He. Figure 3(d), that is position of the plasma front expanding in Xe and figure 4(a) that is the velocity of the plasma front in the same ambient condition is replotted in figure 5, with a common time axis, position and velocity axis are shown along the Y axis in left and right respectively. The whole graph is divided into seven different regions to show that slope of the position graph obtained by simulation gives the simulated velocity graph. For e.g. in region (f) the slope of the position curve suddenly tends to 0, the velocity also tends to 0 at that point as seen in the velocity curve where as in region (d) and (g), the velocity is constant.

The simulated temporal profile of temperature, pressure, density and electron density of the plasma front in case of Xe (dashed line) and He (solid line) as buffer gas is shown in figures 6(a)–(d). Xe being denser than He gives higher resistance to the moving plasma resulting in higher temperature, pressure, density and electron density of the plasma front. The temperature of the plasma front is highest at around 30 nsec (figure 6(a)) which is the pulse duration time, after which it decreases due to the cooling effect of the inert gases. The density profile in case of Xe (figure 6(c)) show a sudden rise at around 290 nsec due to shock wave coming into the plasma . Theoretically, according to perfect gas equation of state, rise in density at around 290 nsec (figure 6(c)) and fall in its temperature at the same time (figure 6(a)) gives no significant change in pressure. This is what is observed

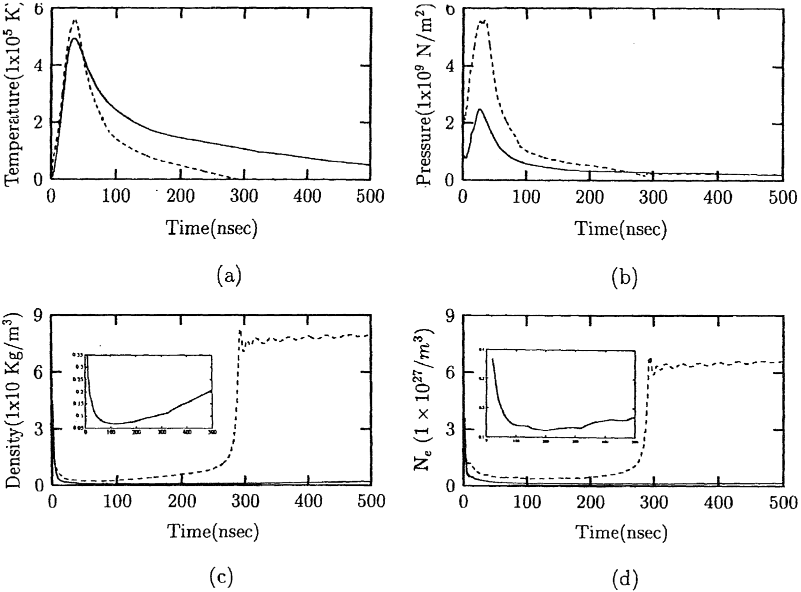

Figure 6. (**a**) Temperature, (**b**) pressure, (**c**) density, (**d**) electron density of the plasma front expanding in Xe and He as obtained fr simulation. Dotted line is for the case of Xe and solid line for He as ambient gas. The inset in (c) and (d) shows density and electron dens of the plasma front expanding in He in enlarged scale neglecting the initial points.

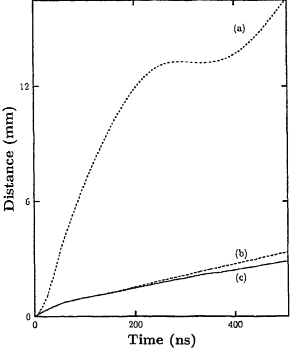

Figure 7. The simulated position of the plasma front as obtained from (**a**) eq. (5) i.e. no change in Navier–Stokes equation, (**b**) eq. (14) i.e. on adding viscous drag term only, (**c**) eq. (16) i.e. on adding viscous drag term and diffusive force term.

in the simulated pressure profile at 290 ns in figure 6(b). The inset in figure 6(c) and figure 6(d) show the density profiles and electron density profiles for He in a magnified scale. It shows that density as well as electron density increases similar to that of Xe but increase is gradual and low in case of He compared to Xe where change is abrupt and high because of its higher density.

Figure 7 shows the effect of different terms which are added in the Navier Stokes equation other than the boundary conditions. The viscous drag term plays the major role in decelerating the plasma front. The diffusive term comes into play at around 300 ns and is much less compared to viscous drag.

The model successfully predicted the results of another experiment by Gu *et al* [5] also.

4. Conclusion

The laser matter interaction in the presence of an ambient gas has been modeled numerically by making appropriate modifications in the one dimensional laser fusion Lagrangian code MEDUSA. The model is applicable for the high pressure of ambient gas where diffusion and interparticle collisions are not dominant in the beginning of the plasma expansion. The simulated result such as position of the plasma front, instability in velocity and the time of evolution of shock wave going into the plasma front are in reasonable agreement with the experimental observations [6]. Using the modified code the model developed can be used to calculate spatial and temporal profile of the plasma

References

[1] Anan'in, ByKovski, Yu V Eremin, A A Zhuravlev, O S Lyubchenko, I K Navikov and S P Frolov, *Sov. J. Quantum Electronics* **21**, 787 (1991)

[2] M A Liberman and A L Velikovich, *Phys. Fluids* **B1**, 1271 (1989)

[3] H S Kim and A S Kwok, *Appl. Phys. Lett.* **61**, 2234 (1992)

[4] David Geohegan, *Appl. Phys. Lett.* **60**, 2732 (1992)

[5] H P Gu, Q H Lou, N H Cheung, S C Chen, Z Y Wang and P K Lin, *Appl. Phys.* **B58**, 143 (1994)

[6] A A Puretzsky, D B Geohegan, R E Hauflerm, R L Hettich, X Y Zheng and R N Compton, in *AIP Conference Proceedings 288, Laser Ablation: Mechanisms and Applications-II* edited by J C Miller and D B Geohegan (AIP Press, New York, 1994) pp. 365

[7] E Hontzopoulos, D Charalambidis, C Fortakis, Gy Farkas, Gy Horvath and Cs Toth, *Opt. Commun.* **67**, 124 (1988)

[8] Daniel Fried and Gene P Reck, *J. Phys.* **24**, 1065 (1991)

[9] T Pisarczyk, A Farynski, H Fiedorowicz, P Gogolewski, M Kusnierz, J Makowski, R Miklaszewski, M Mroczkowski, P Parys and M Szczurek, *Laser and Part. Beams* **10**, 767 (1992)

[10] R Bellantone and Y Hahn, *J. Appl. Phys.* **76**, 1436 (1994)

[11] R Bellantone and Y Hahn, *J. Appl. Phys.* **76**, 1447 (1994)

[12] M Aden, E Beyer, G Herziger and H Kunze, *J. Phys.* **D25**, 57 (1992)

[13] B H Ripin, C K Manka, T A Peyser, E A Mclean, J A Stamper, A N Mostovych, J A Stamper, J Grun, K Kearney, J R Crawford and J D Huba, *Laser and Part. Beams* **8**, 183 (1990)

[14] D L Pappas, K L Saenger, J Bruley, W Krakow, T Gu, R W Collins and J J Cuomo, *J. Appl. Phys.* **71**, 5675 (1992)

[15] C J Knight, *AIAA J.* **17**, 519 (1979)

[16] J J Macfarlane, G A Moses and R R Peterson, *Phys. Fluids* **B17**, 635 (1989)

[17] John L Giuliani, Jr. and Margaret Mulbrandon, *Phys. Fluids* **B17**, 1463 (1989)

[18] O B Anan'in, Yu A Bykovskii, Yu V Eremin, A A Zhuravlev, O S Lyubchenko, I K Novikov and S P Frolov, *Laser Phys.* **2**, 711 (1992)

[19] L I Sedov, *Similarity and dimensional methods in mechanics* (Academic, New York, 1959) G I Taylor, *Proc. R. Soc. London.* **A201**, 175 (1950)

[20] J P Christiansen, DETF Ashby and K V Roberts, *Comp. Phys. Commun.* **7**, 271 (1974)

[21] T D Beynon and E H Smith, *Proc. 2nd International Conference on radiative properties of hot dense plasma* (Sarasota, Florida, 1983)

[22] James E A John, *Gas dynamics*, second edition, (Allwyn and Bacon, INC, Boston, 1984)

[23] Zhaoyuan Han and Xiezhen, *Shock dynamics* (Science Press, Beijing Kluwer Academic Publishers, 1993)

[24] H Slitching, *Boundary layer theory* (Pergamon Press, London, 1955)

[25] Landau and Lifshitz, *Fluid mechanics* (Pergamon Press, New York,1984)

Absence of neutron emission during interaction of deuterium with metal at low energies

A SHYAM and T C KAUSHIK
Neutron Physics Division, Bhabha Atomic Research Centre, Mumbai 400085, India
Email: npd@magnum.barct1.ernet.in

MS received 13 June 1997; revised 18 October 1997

Abstract. Technique and instrumentation to detect reliably, multiplicity of neutrons emitted in sharp bursts ($\leq 100\,\mu$s) has been developed where a burst of as low as 15 neutrons and continuous emission of $\simeq 10^{-1}$ neutron/s may be detected. Using this technique, attempts were made to detect neutron emission from various experiments in which anomalous nuclear effects (or what is commonly referred to as cold fusion) may be expected to occur. No neutrons, above our detection threshold, were detected in the recent series of experiments.

Keywords. Anomalous nuclear effects; cold fusion; deuterated solids; burst neutrons; pulsed neutrons; neutron detection.

PACS Nos 25.70; 28.20; 52.70

1. Introduction

Several investigators, including the present authors [1, 2], have reported on the emission of neutrons when deuterium is loaded into palladium or titanium by electrolysis or by other techniques [3–16]. These experiments are usually referred to as anomalous nuclear effects in deuterium-solid systems or cold fusion. The neutrons were reported to be emitted continuously, as well as in sharp bursts presumably by the D–D fusion reaction

$$^2D_1 + {}^2D_1 \rightarrow {}^3He_2 + {}^0n_1(2.45\,\mathrm{MeV}), \tag{1}$$

where $^2D_1$, $^3He_2$ and $^0n_1$ are deuteron, helium-3 and neutron respectively.

2. Neutron detection systems

In order to confirm and understand the nature of observed neutron emissions, simple, relatively inexpensive and high sensitivity systems had been developed [17] in two configurations, to characterize the burst and continuous neutron emissions. These detection systems were designed and optimized based on neutronics numerical simulations [18] and then through experiments. Hydrogenous materials (epoxy and polyethylene) were used to thermalize, back scatter and stretch ($\simeq 100\,\mu$s) the neutron burst. The thickness of hydrogenous material (to thermalize the neutrons), between

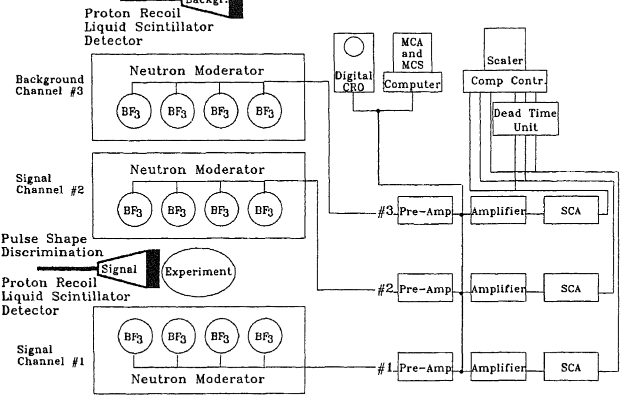

Figure 1. Schematic of the first neutron detecting system.

material was at the back-side of the detectors. This material helped in back-scattering the escaped (signal) neutrons into the detectors. It also, partially, shielded the detectors from background neutrons.

In the first system developed here, 12 boron-tri-fluoride (BF_3) proportional detectors were arranged into three independent channels (see figure 1). Two detector arrays were used to record signal and the third to monitor background. The neutrons were continuously detected in 100 μs and 5 s interval in order to detect burst as well as continuous emissions. The second system had 16 BF_3 detectors in two concentric rings (see figure 2). In this configuration, the second ring acted both as background and signal detector. In both the systems weather-proof connectors were used. The preamplifiers were electromagnetically shielded and kept close to detectors. The system was reliable enough to work satisfactorily even in 100% condensing humidity (of Mumbai monsoon).

Each channel had separate counting electronics (though powered from single source and grounded at same point). The counts from each channel were recorded in a personal computer controlled scalar, communicating to an IBM PC/486 compatible computer through RS-232 serial interface.

The efficiencies were measured using a standard californium-252 source (average neutron energy $\simeq$2.2 MeV, close to D–D fusion neutron energy). The efficiencies of the channels, in the first system were $\simeq 3.9 \pm 0.4\%$, $4.6 \pm 0.4\%$ and $3.9 \pm 0.4\%$, when source was kept close to the detector channels. When the source was kept in the experimental space the efficiencies were $\simeq 3.5 \pm 0.4\%$, $4.2 \pm 0.4\%$ and $0.5 \pm 0.4\%$ for the two signals and the background detector banks, respectively. The average background/s in the three

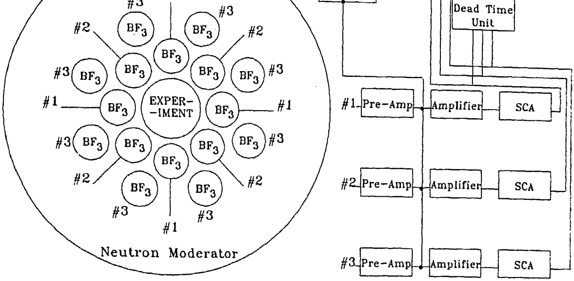

Figure 2. Schematic of the second neutron detecting system.

detector systems were 0.062 ± 0.005, 0.076 ± 0.006 and 0.063 ± 0.005 counts per second (cps). For the second system, the efficiencies and the backgrounds of the three channels (with calibration source kept in the central experimental area) were $5.1 \pm 0.4\%$, $4.9 \pm 0.4\%$, $3.0 \pm 0.4\%$ (outer ring), 0.060 ± 0.005, 0.063 ± 0.005, 0.067 ± 0.006 cps respectively. However, when the calibration source was kept at periphery of the detecting system, at six different locations, all around the circumference, the average efficiencies were $1.1 \pm 0.3\%$, $1.0 \pm 0.3\%$ and $2.5 \pm 0.4\%$ (outer ring). Therefore in this setup, the outer ring of detectors, served the dual purpose of signal as well as background channel.

3. Statistics of detection

3.1 *Continuous emission*

If the counting is done for a very long duration (as in cold fusion experiments), in other words if there is a large number of counting intervals, there is always a probability of getting counts in an interval which are several σ above the background. Therefore the data was analysed by comparing the experimentally observed frequency distribution with Poisson distribution

$$P_p(c) = \mathrm{e}^{-a} \cdot a^c / c!, \tag{2}$$

where P_p is the frequency, predicted by the Poisson distribution, of getting counts c in a counting time-interval, a being mean of counts. The goodness of fit between observed and Poisson frequency distribution was determined by χ^2 (chi-square) test.

As we have used more than one detecting channels, the binomial probability (for isotropic emission) of getting M counts in detecting channel 1 and N counts in the

$$P_b = \left[\frac{[\{(N+M)/2\}!]^2}{\{N!M!\}}\right]^2. \tag{3}$$

This probability is normalized to give $P_b = 1$ for both the counters giving equal counts ($M = N$). This indicates that probability of getting more than twice (or half) the counts in one channel (N) as compared to the counts in another channel (M) is insignificant, unless the counts recorded are very small ($M \leq 2$). By this method the spurious counts, if generated in one channel, due to some defect, could be ignored. The thumb rule criteria used to look for genuine neutron emission was

(i) the counts in one of the signal channel should not be greater than twice (or less than half) the other channel (after normalizing for channel efficiencies),
(ii) the counts in the background channels (a) should be close to background counts, in the first system and (b) should be much less than counts in the signal channels, in the second system,
(iii) the frequency of the event(s) should be higher than predicted by Poisson distribution.

3.2 *Burst emission*

For burst neutron emission, if the average background per second is b, and τ is the counting interval, then the Poisson probability P_s of getting j counts in the interval is

$$P_s(j) = \mathrm{e}^{-b\cdot\tau}\cdot(b\cdot\tau)^j/j!. \tag{4}$$

To get multiplicity of at least 1 ($j = 2$), from continuous emission (in the counting interval of 100 μs and background of $\simeq 0.07/\mathrm{s}$ – as encountered in our experiments) the probability is $2.2.10^{-11}$ or 1 multiplicity count should be observed every 2 months. Therefore observing even a single multiplicity count indicates a burst emission. However as the cosmic ray background also generates bursts, the criteria to identify neutron bursts from the experiments, should be similar to conditions stated for continuous emissions (described later).

4. Experiments and results

Experimental configurations similar to those which were previously performed, and had reported neutron emissions [5, 8, 10, 13, 19–24] were repeated further. The neutron emissions reported in these experiments, were high enough to be detected easily, by the present detecting systems.

One of the most extensively investigated devices is being described in detail here. The device studied was commercially available palladium(Pd)–nickel(Ni) electrolysis cell (or the Milton Roy cell—as it was procured from M/s Milton Roy, Ireland). Other reasons for choosing this configuration of electrolytic cell as an illustrative example are (a) it was reported [25] to have produced large neutron emissions in continuous as well as in burst mode, during the first run of the experiments, (b) during the second run, proton recoil-third run, there appeared to be a low, but definite increase in burst and continuous counts during electrolysis but in a subsequent run counts were observed to be lower during the electrolysis.

4.1 *Commercial palladium–nickel electrolyser*

The commercially available Milton Roy cell had 16 Pd tubes (-3×10^{-3} m outer diameter, 0.2 m long), coated with Pd black and arranged in a circular array, as cathode. The total surface area of the tubes was $\simeq 3 \times 10^{-2}$ m^2. The Pd cathode was surrounded on both sides by two concentric, cylindrical Ni anodes. Three cells of this type were operated for a total five times. These experimental runs (or series) have been labelled as MR1, MR2, MR3, MR4 and MR5.

4.2 *MR1 series of experiments*

The cell was operated with electrolyte consisting of 5 molar (M) sodium deuteroxide (NaOD) dissolved in heavy water (D_2O). The current was maintained at 60 A (2000 A/m^2). The results obtained for MR1 series have already been reported [9, 10]. However it may be noted that during this series all the counters were configured into one segment, connectors were not weather-proof and the preamplifiers did not have electromagnetic shielding.

4.3 *MR2 series of experiments*

This series of experiments were replication of the MR1 series. The cell was again operated at 60 A current, using 5 M NaOD solution in D_2O as electrolyte . However in this series, the BF_3 detectors were segmented to form three independent channels as shown in figure 1. Along with this system, proton recoil liquid scintillator detectors, with pulse shape discrimination capability were also used. The latter could detect fast neutrons (energy threshold $\simeq$1 MeV) with a detection efficiency of $\simeq$40% till 14 MeV neutron energy. With these detectors it was possible to detect fast, continuously emitted, neutrons with a detection threshold of 0.7 n/minute [26].

During this series of experiments, no neutron emission could be observed, either in continuous [26] or in burst mode. It may be noted that this (Milton Roy) cell was equivalent to at least 16 simple cells [3]. Therefore the neutron yield expected from MR cell was at least one order of magnitude higher than reported from a simple cell [3] and thus well above the detection threshold of our detecting system.

4.4 *MR3 series of experiments*

During the third series of experiments (and subsequent runs), the second type of BF_3 neutron detecting system (see figure 2) was employed. As other investigators had reported to observe neutron only after several weeks of loading and using lithium

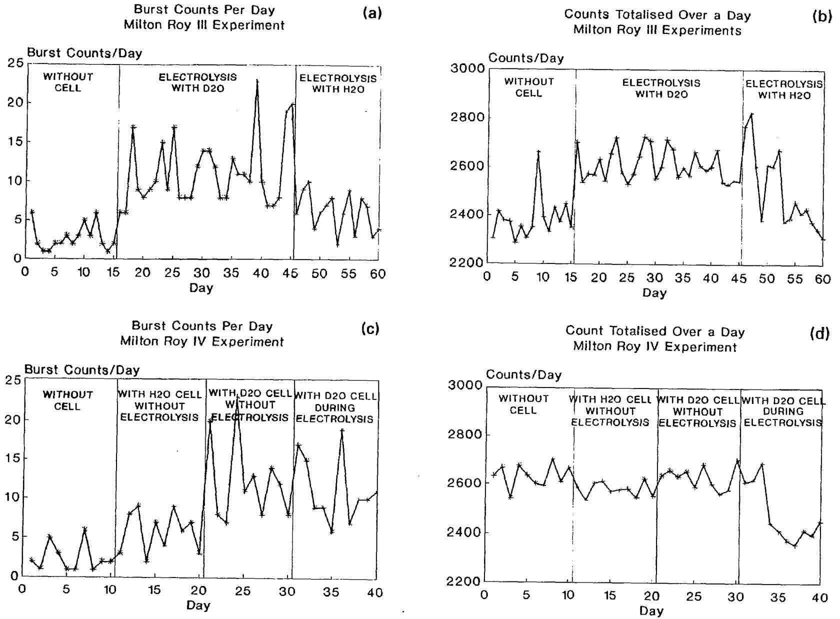

Figure 3. The continuous and burst neutron emission per day for MR3 and MR4 series of experiments.

for 2 months in three different phases. In the first phase, for 15 days, only the detector system's (without cell) background was observed. In the second phase of experiments, the cell was operated at 10 A for the next 30 days, using saturated solution of LiOD in D_2O as electrolyte. In the third phase, the cell was run for (next) 15 days using saturated solution lithium hydroxide (LiOH) in natural water (H_2O) as electrolyte.

The burst and continuous counts per day are plotted in figures 3a, b respectively. It appears from these plots that neutrons were getting produced (burst as well as continuous), not only during D_2O electrolysis (as compared to blank run) but also, to a lesser extent, during H_2O electrolysis [2].

4.5 *MR4 series of experiments*

The fourth set of experiments (MR4 series) were performed in an attempt to reproduce the results of MR3 series with more controls. In this series, for the first ten days data was recorded without cell, for the next ten days data was obtained with cell filled with saturated solution of LiOH in H_2O, but without electrolysis. For next 10 days data was recorded with cell filled with saturated solution of LiOD in D_2O, but without electrolysis. For the last ten days, the cell was operated at 10 A using saturated LiOD in D_2O as electrolyte. As can be seen from figure 3d, the continuous counts observed were lowest, during electrolysis (carried out at 10 A) using LiOD–D_2O electrolyte. This was contrary to the behaviour observed during MR3 series.

4.6 *MR5 series of experiments*

Due to the contradictory results obtained in MR3 and MR4, long duration experiments, MR5 series of experiments were done for shorter durations. Following experiments were performed for 24 h each: (a) blank, (b) cell only, (c) cell filled with H_2O, (d) cell filled with saturated solution of LiOH in H_2O, (e) electrolysis of this cell at 10 A, (f) cell filled with D_2O, (g) cell filled with saturated solution of LiOD in D_2O, (h) electrolysis of this cell at 2 A, (i) electrolysis of the same cell at 4 A, (j) electrolysis of the same cell at 8 A, (k) electrolysis of the same cell at 16 A and (l) electrolysis of the same cell at 32 A.

In this set of runs, no neutrons, in bursts or in continuous mode, could be observed above the detection threshold of the counting system. All the counts were within the statistical variations of the background (the statistical variations in this series of experiments were higher because of shorter duration of the data collection).

5. Discussion

The results obtained in MR4 series were contradictory to those obtained in MR3 series. Such observations may however be explained if the neutrons are assumed to have been produced by cosmic rays (secondary) impinging on the cell and producing neutrons by (nuclear) reactions with Pd, Ni and lithium in H_2O–LiOH cell. Moreover in D_2O–LiOD cells, additional number of neutrons may be produced by disintegration of deuterons by cosmic rays. As the cosmic ray intensity varies periodically [27], it may be conjectured counts were lowest during D_2O–LiOD electrolysis. Since the neutrons were produced by cosmic rays impinging on the cell, the signal channels recorded more neutrons than the background channel.

The number of neutron burst counts were higher, in the case of D_2O–LiOD cell both in MR3 and MR4 runs. However in the MR4 run, such counts were high even before electrolysis and remained approximately the same afterwards (see figure 3c). Hence these bursts could not be attributed to electrolytically induced nuclear reactions. Such bursts were perhaps again produced by large (high multiplicity) cosmic ray showers. More number of bursts observed with the D_2O–LiOD cell may be accounted through possible extra neutrons produced by deuteron disintegration. Muons are also known to be generated in cosmic showers which may further catalyse fusion reactions and contribute [28] to the registered low level neutron yield in the LiOD–D_2O cells.

6. Conclusion

Reliable and high sensitivity detecting systems were used to search for burst as well as continuous neutron emission from electrolysis of D_2O–LiOD. No conclusive evidence of neutron emission (pulsed or continuous) could be obtained from a number of such runs.

A neutron detection system needs to be properly designed to avoid malfunctions which may give rise to misleading signal of neutron emissions from an experimental source. In the long duration experiments, the change in cosmic ray background, also appears to be an important effect which could reasonably explain many contradictory observations from such experiments.

References

[1] A Shyam, M Srinivasan, S B Degwekar and L V Kulkarni, *Multiplicity distribution of neutron emission in cold fusion experiments*, BARC Studies in Cold Fusion, BARC Report 1500 A4 (1989)

[2] A Shyam, T C Kaushik, L V Kulkarni and M Srinivasan, *5th Int. Conf. on Cold Fusion* 181 (1995)

[3] S E Jones, E P Palmer, J B Czirr, D L Decker, G L Jensen, J M Thorne, S F Taylor and J Rafelski, *Nature (London)* **388**, 737 (1989) (later withdrawn)

[4] M Fleischmann, S Pons and M Hawkins, *J. Electroanal. Chem.* **261**, 301 (1989)

[5] A De Ninno, A Frattolillo, G Lollobattista, L Martinis, M Martone, L Mori, S Podda and F Scaramuzzi, *Il. Nuovo Cimento* **A101**, 841 (1989)

[6] K L Wolf, N J C Packham, D Lawson, J Shoemaker, F Cheng and J C Wass, *J. Fusion Energy* **9**, 105 (1990)

[7] J O' M Bockris, G H Lin and N J C Packham, *Fusion Technol.* **18**, 11 (1990)

[8] N Wada and K Nishizawa, *Jap. J. Appl. Phys.* **28**, 2017 (1989)

[9] P K Iyengar, BARC Cold Fusion Experiments, *Proc. 5th Int. Conf. on Emerging Nuclear Energy Systems* (Karlsruhe, F R Germany, World Scientific, Singapore, 1989)

[10] P K Iyengar and M Srinivasan (editors), Bhabha Atomic Research Centre Studies in Cold Fusion, Bhabha Atomic Research Centre Report BARC-1500 (1989). See also *Fusion Technol.* **18**, 32 (1990)

[11] A Takahashi, T Takeuchi, T Iida and M Watanabe *J. Nucl. Sci. Tech.* **27**, 663 (1990)

[12] X Z Li, Chinese Efforts in Understanding the Cold Fusion Phenomena, *Proc. 2nd Annual Conf. on Cold Fusion* (Como, Italy, 1991)

[13] H O Menlove, M M Fowler, E Garcia, M C Miller, M A Paciotti, R R Ryan and S E Jones, *J. Fusion Energy* **9**, 495 (1990)

[14] F Fernandez, J Sevilla, B Escarpizo and C Sanchez, Nuclear Effects in Electrolytically Deuterated Ti and Pd, *Proc. Anomalous Nuclear Effects in Deuterium Solid Systems* (Provo, Utah, USA, 1990)

[15] E Storms, *Fusion Technol.* **20**, 680 (1991)

[16] M Srinivasan, *Curr. Sci.* **60**, 417 (1991)

[17] A Shyam, T C Kaushik, L V Kulkarni and M Srinivasan, *Indian J. Pure Appl. Phys.* **32**, 837 (1995)

[18] A Sinha, Neutron Physics Division, Bhabha Atomic Research Centre, Mumbai, 1989 (private communication)

[19] M G Nayar, S K Mitra, P Raghunathan, M S Krishnan, S K Malhotra, D G Gaonkar, A Shyam and V Chitra, *Fusion Technol.* **18**, 39 (1990)

[20] M S Krishnan, S K Malhotra, D G Gaonkar, M G Nayar and A Shyam, *Fusion Technol.* **18**, 42 (1990)

[21] P Raj, P Suryanarayana, A Sathyamoorthy and T Datta, *Fusion Technol.* **18**, 80 (1990)

[22] A R Arzhannikov and G A Yezerashvili, Preprint INP 90–36 (Institute of Nuclear Physics, Novosibirsk, USSR, 1990)

[23] B Y Liaw, P L Tao, P Turner and B E Liebert, Elevation Temperature Excess Heat Production Using Molten Salt Electrochemical Techniques, *Proc. Cold Fusion Symp.* (World Hydrogen Energy Conference #8, Hawai 49, 1990)

[24] G Mengoli, M Fabirizio, C Manduchi, E Milli and G Zannoni, *J. Electroanal. Chem.* **395**, 249 (1995)

[25] M S Krishnan, S K Malhotra, D G Gaonkar, M Srinivasan, S K Sikka, A Shyam, V Chitra, T S Iyengar and P K Iyengar, *Fusion Technol.* **18**, 35 (1990)

[26] D M Nadkarni, Nuclear Physics Division, Bhabha Atomic Research Centre, Mumbai, 1991 (private communication)

[27] Yavorsky *et al*, *Handbook of Physics* (Mir Publishers, Moscow, 1980)

[28] L Chatterji, Saha Institute of Nuclear Physics, Calcutta, 1990 (private communication)

Use of spherical gratings in a toroidal grating mount for vuv-soft x-ray synchrotron radiation

K J S SAWHNEY, A I MUNSHI and R V NANDEDKAR
Centre for Advanced Technology, Indore 452 013, India
E-mail: sawhney@cat.ernet.in.

MS received 9 September 1997; revised 27 November 1997

Abstract. A toroidal grating monochromator (TGM) based beamline was designed earlier and it is being setup on the 450 MeV Indus-1 synchrotron radiation source. This beamline operates in 40–1000 Å wavelength range and gives a moderate resolution (~500) at high throughput. Now-a-days, spherical gratings are giving very high resolution in some complex monochromators. We have evaluated the use of spherical gratings in the simple rotation mount of a TGM. The motivation has been to evaluate if the existing TGM beamline, without any hardware changes, can be used with the much cheaper spherical gratings. The two monochromators, employing toroidal and spherical gratings respectively, have been compared by performing detailed ray tracing calculations. Our study shows that, with the same mechanical hardware, a real spherical grating monochromator gives better performance compared to the conventional TGM with respect to the spectral resolution and the flux. Furthermore, for moderate resolution this improvement is realized even when the exit slit is not moved to keep the spherical grating in-focus.

Keywords. Synchrotron radiation; beamline; monochromator; soft x-ray.

PACS No. 42.10

1. Introduction

A number of synchrotron radiation facilities exist world wide, many of which emit radiation in the soft x-ray and vacuum ultra violet (XUV) wavelength range (10–1200 Å). In this wavelength range, grazing incidence optics in ultra high vacuum (UHV) environment has to be used. Many designs of the monochromators to be put up on beam lines for this wavelength range exist [1, 2] and are based on plane, toroidal or spherical gratings. Many of these designs require stringent closed coupled movements of the optical elements in the UHV environment and are therefore difficult to realize in practice and are quite expensive. In most cases, these complicated designs are essential to derive the best resolution from the monochromators. However, there are many application areas like photoelectron spectroscopy, reflectometry and radiometry where the requirement is not for very high resolution but of good throughput at moderate resolution ($\lambda/\Delta\lambda \sim 500$–1000). Relatively simple monochromator designs can deliver these requirements leading to a great deal of simplicity in the instrumentation. One such design [3] that has been quite popular during the eighties is the use of toroidal gratings in the constant deviation geometry (TGM) wherein a simple sine bar drive rotates the grating about its axis for toroidal shapes are difficult to fabricate and polish. Even the best toroidal gratings have figure errors of $\sim$5 arcsec. These tangent slope errors severely limit the resolution achievable with these monochromators. However, since there is only one optical element between the entrance and exit slits, these monochromators yield high throughput.

On the other hand, spherical and plane surfaces are easier to fabricate with better figures. Spherical surfaces with 1 arcsec slope error are quite common. However, earlier not many monochromators were designed using spherical gratings in the XUV wavelength range because spherical surfaces suffer from strong astigmatism and coma aberrations at grazing incidence. In the last decade, a few good designs [4–7] for spherical grating based monochromators have come up which give very high spectral resolution. These designs generally require complicated mechanical movements and very small slit widths. In some designs [6, 7], the exit slit, and also at times the entrance slit, is required to be moved to satisfy the Rowland circle condition. This requirement of moving the slits with wavelength scan is, at times, not desirable for certain experiments.

A beamline based on a TGM has been designed [8] and is being set up on the Indian synchrotron facility Indus-1 [9] that is coming up in our centre. This beamline operates in 40–1000 Å wavelength range and gives moderate resolution ($\sim$500) at high throughput. Since now-a-days, spherical gratings are giving very high resolution in Dragon [5] and focusing-spherical grating type of monochromators [7], we have evaluated the performance of spherical gratings in the simple rotation mount of a TGM. The motivation has been to evaluate if the existing TGM beamline, without any hardware changes, can be used with the much cheaper spherical gratings in a later upgrade of the beamline. To evaluate the feasibility of such a scheme, we have evaluated the configuration for the monochromator in which toroidal gratings in the TGM mount are replaced by spherical gratings, and suitable preoptics [10] is used which decouples the meridional and sagittal focus positions to eliminate the astigmatism of the spherical grating. Using ray tracing calculations, the performance of this spherical grating based monochromator is evaluated and compared with the conventional TGM monochromator designed earlier. The details of this intercomparison is given in this paper which shows that the monochromator with spherical gratings give better performance both in terms of resolution and throughput. Moreover, though this intercomparison has been done for the Indus-1 synchrotron source, the conclusions drawn are fairly general and will hold for any other XUV synchrotron source also.

2. Optical configuration

The requirement put on the beamline is that it (i) produces monochromatic ($\lambda/\Delta\lambda \sim$500–2000) radiation in 40–1000 Å wavelength range, (2) provide a relatively high intensity beam of small size at the sample position, and (3) yield a spatially fixed beam after the monochromator.

The detailed optical design of the beamline using TGM was derived earlier [8]. Parameters for the SGM, to fit in the same mechanical hardware, have been determined by a semi-empirical optimization procedure. It involves the optimization algorithm of Mckinney and Howells [11] as well as trial and error. In the first step of optimization, the

Source to toroidal premirror	4500 mm	4500 mm
Premirror to entrance slit	2250 mm	2250 mm
Entrance slit to toroidal grating	1000 mm	1000 mm
Grating to exit slit	1414 mm	1414 mm
Toroidal premirror		
Major radius	38236 mm	38236 mm
Minor radius	235 mm	363 mm
Included angle	171°	171°
Grating	Toroidal	Spherical
Major radius	7977 mm	7662 mm
Minor radius	182.3 mm	7662 mm
Included angle	162°	162°
Grating density		
for 40–120 Å	1800 grooves/mm	1800 grooves/mm
for 120–360 Å	600 grooves/mm	600 grooves/mm
for 360–1000 Å	200 grooves/mm	200 grooves/mm
Grating size	75 mm× 20 mm	75 mm× 20 mm

resolution ($\Delta\lambda$), integrated over the desired wavelength range, was minimized. However, on comparing this resolution with that of TGM it turned out that, though the overall integrated resolution over the whole wavelength range was better than TGM, the resolution at higher energies (i.e., lower photon wavelengths) was worse than the TGM. Hence the SGM was reoptimized semi-emperically so as to get similar or better resolution at each wavelength in the wavelength range of interest. During the optimization, we were constrained to keep the entrance arm length, the exit arm length and the deviation angle fixed, in order to fit the SGM into the hardware of TGM, and only the radii of the grating was varied. A total of three gratings are used to cover the full wavelength range. Various parameters of the monochromator are given in table 1.

The optical layout of the two configurations is given in figure 1. Configuration 1 comprises of a premirror M_1, an entrance slit S_1, a toroidal grating TG, an exit slit S_2 and a post mirror M_2. The prefocussing toroidal mirror is kept at a distance of 4500 mm from the source, which deflects the SR vertically by 9°. The mirror demagnifies the SR source by a factor of 2 and focuses both in sagittal and meridional direction at the entrance slit. The grating in the TGM is vertically dispersing at a constant deviation of 162°. A second toroidal mirror is used to refocus the exit slit image onto the sample.

Configuration 2 also comprises of a premirror M_1, an entrance slit S_1, a spherical grating SG, an exit slit S_2 and a post mirror M_2. The premirror M_1 reflects the beam vertically by 9°, but unlike the premirror of configuration 1, it focuses the beam horizontally and vertically on different positions. The two radii of this toroidal mirror are so chosen that it focuses the beam horizontally on the exit slit and vertically on the entrance slit of the optimized monochromator. The ideal monochromator for this type of preoptics is a cylindrical grating [5] which does not modify the sagittal focus position of the premirror. Use of a spherical grating having a non-zero curvature in the sagittal direction brings in the horizontal focus point from the desired exit slit position. Since the

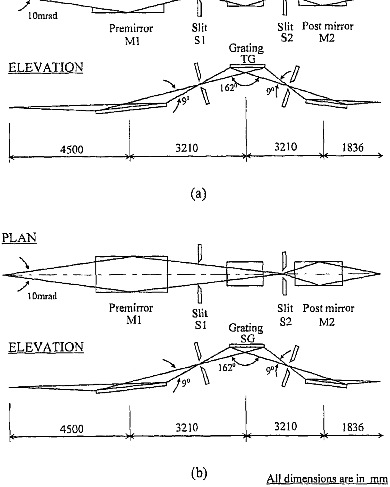

Figure 1. Optical layout of the two configurations (**a**) based on toroidal grating; (**b**) based on spherical grating.

grating rotates about its axis for wavelength scan, this influence of the grating on the horizontal focus position is wavelength dependent. We have increased the horizontal radius of the toroidal premirror empirically so as to get the sagittal focus position at the exit slit at a wavelength in the middle of the wavelength range of interest. A toroidal post mirror is again used to refocus the exit slit image onto the sample.

3. Ray tracing studies

The two configurations for the beamline were ray traced using the ray tracing code RAY [11]. The radiation source is taken to be the dipole of the 450 MeV Indus-1 storage ring and its various parameters are given in table 2. The vertical divergence of the SR beam from a bending magnet source varies as the wavelength is scanned and is in the range of 2–9 mrad for Indus-1. In the horizontal direction, the beamline accepts a fan of 10 mrad. Various parameters of the gratings and mirrors given in table 1 are used for ray tracing. The tangent slope errors of 5 arcsec on toroidal grating and 1 arcsec on spherical grating have been considered which correspond to the typically achievable manufacturing tolerances for these grating shapes.

Electron energy	450 MeV
Source type	Bending magnet
Bending magnet radius	1000 mm
Critical wavelength, λ_c	61 Å
Source size (r.m.s)	0.8 mm ×0.1 mm
Horizontal divergence	10 mrad
Vertical divergence	2–9 mrad

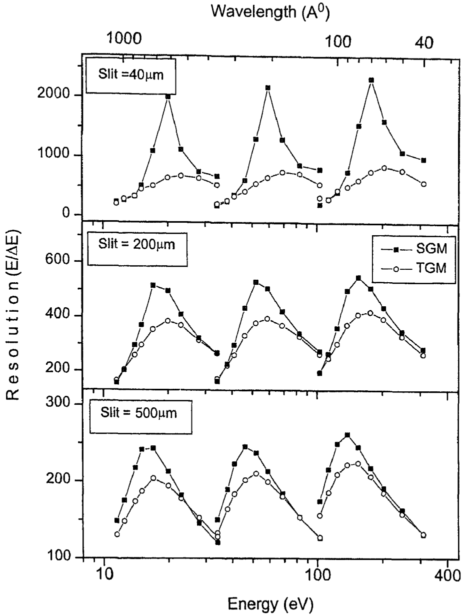

Figure 2. Spectral resolution ($E/\Delta E$) as a function of energy for slit settings of 40, 200 and 500 μm.

The resolving power of the two monochromator configurations for slit settings of 40, 200 and 500 μm, respectively is shown in figure 2. The figure shows that in the low-energy range of each grating, the two configurations give similar resolution while for the rest of the spectral range the SGM configuration gives much higher spectral resolution

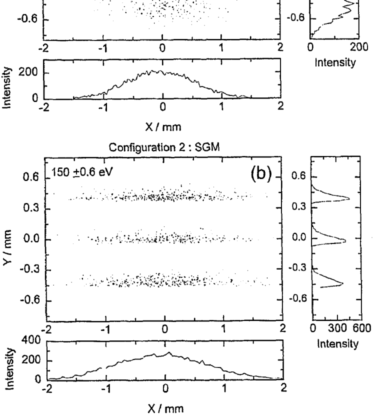

Figure 3. Spot diagrams at 149.4, 150.0 and 150.6 eV for (**a**) TGM configuration, and (**b**) SGM configuration. Also shown is the intensity distribution in the horizontal and vertical directions.

than the TGM configuration. For instance, with slit size of 40 μm, the SGM configuration gives a peak resolving power of 2300 as against 900 available from the TGM configuration. The peak in the resolution curve, with narrow slit widths, is sharper in the case of spherical gratings. This is a manifestation of the fact that the spherical gratings give very high resolution when the Rowland circle condition is satisfied (at the peak). This feature is exploited many times by the beamline designers by choosing the peaks, by appropriate choice of line densities and grating curvature, to lie in the near edge region of specific elements. Figures 3a and 3b show the spot diagrams at the exit slit planes of TGM and SGM respectively for photon energies 149.4, 150.0, 150.6 eV. While the TGM configuration is not able to resolve the three energies, with the SGM configuration these energies are seen to be well separated.

RAY program also calculates the flux throughput of the beamline by considering the wavelength dependent radiation emission from the Indus-1 bending magnet, the absolute reflectivities of the optical elements, figure errors on all optical elements including the gratings, and the geometrical loss in the beamline. The grating efficiency could not be

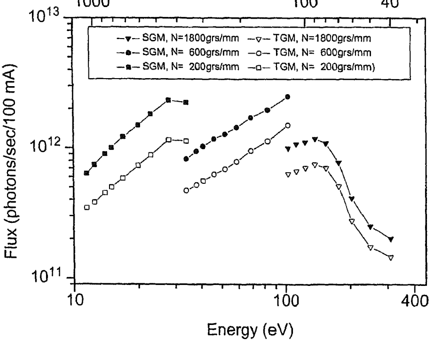

Figure 4. Photon flux at the sample position for the two configurations of the beamline. Slit settings have been kept at 200 μm.

calculated, as the parameters of the commercial gratings employed were not available. In the soft x-ray regime, the grating efficiency is typically in 10 to 30% range and therefore for flux calculations we have assumed it to be 20% over the whole wavelength range. The flux available at the sample position from the two configurations is shown in figure 4 from which it is clear that the flux throughput of the SGM configuration is higher than that from the TGM configuration. These ray tracing results therefore show that if the two configurations of the beam line are operated in exactly identical conditions then the SGM configuration gives better performance both in terms of resolution and flux.

4. Discussion

The principal aberration of a spherical grating in grazing incidence is the astigmatism, which gets compensated in configuration 2 by the use of a proper toroidal premirror which focuses sagitally and meridionally at separate points. The other major components of the aberration in grazing incidence geometry are the defocus, astigmatic coma and coma [13]. Through the optimization process, the monochromator is brought to focus at two wavelengths. Then at the in-between wavelengths, the monochromator remains approximately focused. The defocus component of the aberration can be eliminated by moving the exit slit, as the wavelength is scanned, to keep the monochromator in-focus [13]. We have also determined analytically the various components contributing to the wavelength resolution and figure 5 shows the full width at zero height (fwzh) resulting from different terms for a SGM. This figure shows that, over most of the wavelength range, the astigmatic coma dominates the aberration limited resolution and, therefore, moving the exit slit to keep the monochromator in-focus will not improve the resolution

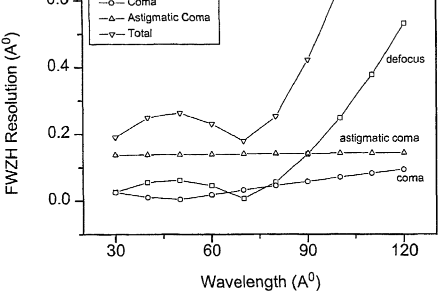

Figure 5. Various components of the aberration limited resolution (full width at zero height) derived analytically for the SGM configuration.

significantly. Thus movement of the exit slit can be avoided which leads to a great deal of simplicity in the experimental station. Keeping the monochromator in-focus at all wavelength will help if the relative proportion of astigmatic coma is reduced compared to the defocus contribution. This can be done by masking the non-dispersive aperture of the grating since astigmatic coma depends on the square of the non-dispersive aperture. However, this will drastically reduce the throughput of the monochromator.

5. Summary

It is shown that the use of spherical gratings in a constant deviation TGM mount gives better performance if proper preoptics is used to reduce the astigmatism. Detailed comparison of this monochromator with a conventional TGM is performed using ray tracing and is presented in this paper. If one is interested in a moderate resolution of ~1000 then one can get the improved performance even without moving the exit slit position. Use of spherical gratings have the obvious advantages – they are easier to fabricate to high accuracy and because of symmetrical shape they are easier to align in the beamline.

Acknowledgement

We thank BESSY, Berlin for kindly providing the source code of RAY program.

References

[1] R L Johnson, *Nucl. Instrum. Methods* **A246**, 303 (1986)
[2] R L Johnson, in *Handbook of synchrotron radiation* edited by E E Koch (North-Holland, Amsterdam, 1983) vol. 1, p. 173
[3] B P Tonner and E W Plummer, *Nucl. Instrum. Methods* **177**, 153 (1980)

[4] F C Brown, R Z Bachrach and Neil Lien, *Nucl. Instrum. Methods* **152**, 73 (1978)

[5] C T Chen, *Nucl. Instrum. Methods*, **A256**, 595 (1987)

[6] H A Padmore, *SPIE Proceedings* **733**, 253 (1986)

[7] W B Peatman, J Bahrdt, F Eggenstein, G Reichardt and F Senf, *Rev. Sci. Instrum.* **66**, 28 (1995)

[8] K J S Sawhney and R V Nandedkar, *Pramana – J. Phys.* **42**, 49 (1994)

[9] S S Ramamurthi and G Singh, *Nucl. Instrum. Methods* **A359**, 15 (1995)

[10] W A Rense and T Violett, *J. Opt. Soc. Am.* **49**, 139 (1959)

[11] W R Mckinney and M R Howells, *Nucl. Instrum. Methods* **172**, 149 (1980)

[12] F Shaefers, RAY program, BESSY, Berlin (unpublished)

[13] J B West and H A Pdmore, in *Handbook of synchrotron radiation* edited by G V Marr (Nor Holland, Amsterdam, 1987), vol. 2, p. 21

Pramana journal of physics Vol. 50 (No. 1), January 1998

Contents

Universality in the effective pair interaction of d-shell metals – Compressibility and vacancy formation energy of $3d$-liquid metals . . . . *A K Karmakar and R N Joarder* 1

Evidence of polaronic charge carriers in oxide superconductors . . . . *C M Srivastava* 11

Electrical properties of a-antimony selenide . . . . *Sanjeev Gautam, D K Shukla, Shelly Jain and N Goyal* 25

Monte-Carlo optimization of correlated helium wave function . . . . *Sabyasachi Kar and Puspajit Mandal* 35

Total electron scattering cross sections for nitrous oxide at low electron energies . . . . *P Rawat, K P Subramanian and Vijay Kumar* 45

Hyperspherical calculation for electron hydrogen atom ionization collisions in a symmetric form . . . . *J N Das* 53

Numerical modeling of laser matter interaction in the presence of an ambient gas . . . . *A Neogi and R K Thareja* 63

Absence of neutron emission during interaction of deuterium with metal at low energies . . . . *A Shyam and T C Kaushik* 75

Use of spherical gratings in a toroidal grating mount for vuv-soft x-ray synchrotron radiation . . . . *K J S Sawhney, A I Munshi and R V Nandedkar* 85

Indexed in CURRENT CONTENTS ISSN 0304–4289